NUCLEAR MAGNETIC RESONANCE STUDY OF COLEMANITE

NUCLEAR MAGNETIC RESONANCE STUDY OF COLEMANITE

By

FRANK HOLUJ, B.Sc., M.Sc.

A Thesis

Submitted to the Faculty of Graduate Studies

in Partial Fulfilment of the Requirements

for the Degree

Doctor of Philosophy

McMaster University

October 1958

DOCTOR OF PHILOSOPHY (1958)
(Physics)

McMASTER UNIVERSITY
Hamilton, Ontario

TITLE: Nuclear Magnetic Resonance Study of Colemanite

AUTHOR: Frank Holuj, B.Sc. (University of London)
M.Sc. (McMaster University)

SUPERVISOR: Professor H. E. Petch

NUMBER OF PAGES: x, 72.

SCOPE AND CONTENTS:

A single crystal of colemanite, which is ferroelectric at temperatures below about -2.0° C., has been investigated by means of nuclear magnetic resonance (n.m.r.) techniques, over a temperature range 52° C. to -136° C.

The splitting of the B^{11} n.m.r. signal in colemanite, caused by the perturbation of the nuclear Zeeman levels by the interactions between the nuclear electric quadrupole moment and the electric field gradients existing at the boron sites at room temperature and at -40° C., has been fully analysed, using the procedure developed by Volkoff and coworkers. The quadrupole coupling constants, the asymmetry parameters and the orientations of the principal axes of the electric field gradient tensors at room temperature and -40° C. are given in Tables XXV - XXVII. A selected set of B^{11} n.m.r. lines has been examined over the temperature range 52° C. to -136° C. This investigation suggests that the ferroelectric transition is second-order and not the order-disorder or martensitic type. The transition temperature itself has

been found to depend upon the history of the crystal, but is apparently about 2° C. higher than previously reported temperatures of about -2.0° C. In addition, a previously unknown phase in colemanite is reported. A large temperature hysteresis loop is associated with the transition to the new phase; on cooling, the transition takes place at about -80° C. whereas on heating, the transition takes place at about -35° C. The point groups for the three phases have been determined as 2/m., 2 and 1 going from room temperature to -80° C., respectively.

The results of the n.m.r. investigation have been interpreted, as far as possible at present, in terms of the crystal structure.

ACKNOWLEDGEMENTS

I would like to express my sincere thanks to Professor Petch for his constant interest and kind help throughout my experimental work, culminating in this thesis, and expecially for his excellent suggestion as to the topic for this thesis. I would also like to thank Dr. H. D. Megaw for many interesting discussions while she stayed at McMaster University as a Visiting Professor. Acknowledgement is also due to Mr. R. D. Datars who carried out a preliminary work on some single crystals of colemanite.

Thanks are due to the employees of the Machine Shop for constructing the crystal holders, the cold-cell and the copper coils at the heat exchanger.

This research was made possible by Defense Research Board of Canada grants-in-aid to Professor Petch. The author is grateful for financial support in the form of a Cominco Fellowship awarded for three consecutive years by the Consolidated Mining and Smelting Co. Ltd. of Canada.

TABLE OF CONTENTS

LIST OF ILLUSTRATIONS

LIST OF TABLES

CHAPTER I

INTRODUCTION

I. 1. The first successful nuclear magnetic resonance (n.m.r.) experiments, using bulk material, were carried out independently near the end of 1945 by Purcell, Torey and Pound ('46) and by Bloch, Hansen and Packard ('46). The first group of physicists found the n.m.r. signal of protons in paraffin whereas the second group found it in water. The two groups used methods which appeared different at that time but are now regarded as equivalent. The theoretical basis of both methods is the resonance condition:

$$\nu_o = \frac{\mu H_o}{Ih}$$

Here ν_o is the frequency at which the n.m.r. absorption takes place, H_o is the externally applied magnetic field, μ is the nuclear magnetic moment, I is the nuclear spin quantum number and h is Planck's constant. The importance of the discovery lies in the facts that with values of H_o easily obtained in the laboratory (of the orders of several kilogauss) n.m.r. frequencies occur in the radio-frequency range and that the resonance frequencies can be measured with great precision.

The most direct application of n.m.r. methods is to the measurement of gyromagnetic ratios (g-factors) of stable isotopes. Only relative measurements can be made so that the absolute value of at least one nuclear g-factor must be known in order to put all the measurements on an absolute basis. The nuclear magnetic moment of a nuclide can be calculated if its spin, I, is known as well as its g-factor. Conversely,

the method can be used to measure Ho in absolute units once a nuclear g-factor is known. Apart from the extraordinary precision which it made possible in the measurements of some nuclear quantities, the n.m.r. technique was found useful in other branches of physics. The fine structures of n.m.r. spectra, arising from the interactions of nuclei with their surroundings, supplied a means of studying some aspects of nuclear environment. For example, the shift of the resonant frequencies due to the local variations of the magnetic field at nuclear sites, occupied by the same isotope, gave the chemist a means of studying chemical reaction rates and of solving some problems in stereochemistry. Also, the interaction of a nuclear electric quadrupole moment with an inhomogeneous electric field set up by its environment, supplied the solid state physicist with a tool to study electrical properties, phase transitions, and crystal symmetry in solids. It is this latter interaction with which we shall concern ourselves in this thesis. In other words, nuclei, already present in their normal sites in a crystal, will be used as probes to explore the properties of the crystal.

I. 2. What follows is a brief review of the origin and of some previous studies of n.m.r. spectra in crystals. The Hamiltonian of a single nucleus, whose spin quantum number is I and magnetic moment is $\vec{\mu}$, placed in a uniform magnetic field, $\vec{Ho}$, is:

$$\mathcal{H} = -\vec{\mu}.\vec{Ho}$$

The nucleus in these circumstances possesses 2I+1 equidistant Zeeman energy levels. A radiation field of frequency,

$$\nu_o = \left|\frac{\mu Ho}{Ih}\right|$$

and with the correct polarisation properties, will induce transitions

between the adjacent energy levels. In a sample containing many identical nuclei which interact only with the uniform magnetic field Ho, the energy levels will be the same for all the nuclei. If the nuclear spins are in thermal equilibrium with their surroundings, the lower energy states will have a larger population, so that the induced transitions between adjacent energy levels will give a net absorption of energy. If in addition, the nucleus has a non-zero electric quadrupole moment, referred to from now on as $\tilde{Q}$, it will interact with a non-vanishing electric field gradient, referred to from now on as $\nabla\tilde{E}$. At the site of any nucleus, $\nabla\tilde{E}$ is characteristic of the crystal structure. The Hamiltonian of a nucleus in these circumstances is:

$$\mathcal{H} = -\vec{\mu}.\vec{Ho} + Q.\nabla\tilde{E}$$

The last term in this expression represents the interaction of $\tilde{Q}$ with $\nabla\tilde{E}$. The result of this additional interaction is that the $2I + 1$ nuclear Zeeman levels are shifted in energy so that they no longer are equidistant. This means that the $2I$ transitions between adjacent levels no longer involve the same energy, but give rise to a spectrum of $2I$ distinct n.m.r. lines. If the quadrupole effect, $\tilde{Q}.\nabla\tilde{E}$, is small when compared with the magnetic term, $\vec{\mu}.\vec{Ho}$, this Hamiltonian can be solved by the perturbation method. The expression for the energy eigenvalues are then given by Eq. (8) of Chapter II. For most practical purposes only the first three terms are retained because the series converges rapidly. The second and the third terms of Eq. (8) are called in this thesis the first and the second order nuclear quadrupole terms, respectively. If the quadrupole effect is sufficiently small it is accurately described by the first order nuclear quadrupole term alone.

The first theoretical and experimental investigation of the quadrupole effect in crystalline matter was carried out by Pound ('50). He investigated the n.m.r. spectrum of Na^{23} in $NaNO_3$ and of Al^{27} in Al_2O_3 (corundum). The Na^{23} n.m.r. spectrum was completely described by the first order nuclear quadrupole term, whereas in the case of the Al^{27} n.m.r. spectrum it was necessary to include the second order nuclear quadrupole term. Pound's work is actually a special case of the general theory. The lack of generality arises from the fact that all Na and Al nuclei occupy crystallographically identical sites in the unit cell of their respective, axially symmetric crystals. Volkoff and coworkers extended both theory and experimental procedure to the completely general case of several non-equivalent nuclear sites per unit cell in non-axially symmetric crystals. They studied the n.m.r. spectra of Li^7 (Volkoff, '51) and Al^{27} (Petch, '53, and Volkoff, '53) in spodumene and of B^{11} in kernite (Waterman, '55). The first paper in the series describes the study of the n.m.r. spectrum of Li^7 in spodumene. The case of Li^7 in spodumene is similar to the case of Na^{23} in $NaNO_3$ since all lithium nuclei occupy crystallographically identical sites and the Li^7 n.m.r. spectrum displays small nuclear quadrupole effect, but the case of Li^7 in spodumene is more general because spodumene is non-axially symmetric. The next two papers of the series describe the n.m.r. spectrum of Al^{27} in spodumene. The analysis of the spectrum is carried out using only the second order nuclear quadrupole term. In other respects the Al^{27} n.m.r. spectrum is similar to that of Li^7 because it originates from crystallographically identical Al^{27} sites in the unit cell of spodumene. A perfectly general n.m.r. spectrum is described in the last paper of this series, i.e., the n.m.r.

spectrum of B^{11} in kernite. This generality lies in the fact that boron nuclei occupy several non-equivalent sites in the unit cell of kernite.

I. 3. It was mentioned before that the nuclear quadrupole effect can be used to study electrical properties, phase transitions, crystal symmetry, etc. in solids. The interpretation of certain features of n.m.r. spectra in terms of crystal symmetry is a straightforward matter. The eigenvalues of the product $\hat{Q}.\tilde{\nabla E}$ and the orientations of its principal axes with respect to a system of coordinate axes fixed in a crystal come out of the mathematical analysis of the spectra. However, the complete interpretation of n.m.r. results in terms of microscopic crystalline electric fields is difficult because of the following: the evaluation of the tensor $\tilde{\nabla E}$ from the experimentally measured product $\tilde{Q}.\tilde{\nabla E}$ is difficult because of the uncertainty of the values of Q quoted in the literature.* Another difficulty arises from the lack of a complete theory for the wave functions involved in chemical bonding in crystals. And yet another serious difficulty arises from the following: only a part of the total nuclear quadrupole effect, $\tilde{Q}.\hat{\nabla E}$, arises from the gradient of the electrostatic field denoted by $\tilde{\nabla \mathcal{E}}$ produced by all other atoms in the crystal structure. The balance is produced by the electric field gradient set up by the distortion of the atom in which the nucleus is situated. This distortion originates from the nuclear quadrupolar electric field and from the electric field, $\mathcal{E}$, mentioned above, and adds, in effect, a contribution $\gamma\hat{\nabla \mathcal{E}}$ to the total field gradient, $\tilde{\nabla E}$. The coefficient

---

*$\hat{Q}$ denotes the nuclear electric quadrupole tensor. Q stands for the customarily defined nuclear electric quadrupole moment, i.e., the largest component of $\tilde{Q}$ measured in the direction of the spin axis of the nucleus.

γ, called the "antishielding factor," plays a very important part in the theory of electric field gradients in crystals because of its large magnitude in some atoms (for example, for B^{+3} ion γ is -0.145 (Das,'56) but for Cs^{+} ion it is + 143.5 (Sternheimer,'56). The accuracy with which γ is calculated is low because it is based on a series of approximations.

The n.m.r. method lends itself well to the study of relative changes occurring within the crystal framework at phase transitions. This is because the product $\tilde{Q}.\tilde{\nabla E}$ depends critically upon the crystal structure. The validity of this was amply demonstrated by Cotts and Knight ('54). They studied the n.m.r. spectra of Nb^{93} in $KNbO_3$ as a function of temperature. $KNbO_3$ had been known to exist in four different phases in the temperature range 410° C. to -196° C. Three of these phases had been known to be ferroelectric, and the transition temperatures had been accurately established. The changes in the configurations of the n.m.r. spectra obtained when the crystal temperature was varied from 400° C. to -196° C. confirmed the existence of the four phases. The temperatures at which these changes occurred corresponded to the transition temperatures. The abruptness with which each change occurred supplied information about the order of the respective transition. The three phase transitions in this temperature range were of first order because the change in the configuration of the spectrum occurred abruptly at the three transition temperatures. Cotts and Knight encountered great experimental difficulties. The single crystals of $KNbO_3$, which they used, frequently twinned and shattered while their temperatures were varied. Considering that the crystals were difficult to replace and that the proper orientation

of the single crystal with respect to the magnetic field calls for a time consuming procedure, the experiment was unduly protracted. However, these experimental difficulties are by no means typical, as this thesis demonstrates.

Before formulating the problem for this thesis we shall first discuss the phenomenon of ferroelectricity.

I. 4. Megaw ('57) defines a ferroelectric crystal as "a crystal possessing reversible spontaneous polarisation as shown by a dielectric hysteresis loop." Other properties of ferroelectric crystals are as follows:

1. They possess a dielectric hysteresis loop, indicating reversible spontaneous polarisation.
2. They show disappearance of hysteresis at a certain temperature, the Curie point.
3. They have a domain structure, which may be visible in polarised light.
4. They have a high dielectric constant, rising to a peak at the Curie point.
5. The falling-off of their dielectric constant above the Curie point follow a Curie-Weiss law.
6. They possess a pseudosymmetric structure.
7. Their symmetry places them in a polar class.
8. They have a transition at the Curie point to a form of higher symmetry.
9. The Curie point is raised (or a lower Curie point lowered) by the application of a biassing field.

10. There is a sudden appearance of surface charges at the transition.

The changes in atomic arrangement at the transition into the ferroelectric phase, since they are completely reversible, must be very small. In crystallographic language they are referred to as "displacive" transitions which only involve very small distortions of the atomic network in contrast to the "reconstructive" transitions in which the network is broken up into small parts and reassembled. This description of the transition emphasises only the crumpling of the framework and not the small movements of atoms relative to the framework which are important in ferroelectrics. Accordingly, a more descriptive term for a ferroelectric phase is "pseudosymmetric," which means that the phase is derived from a structure of higher symmetry by small displacements of some, or all, atoms in the network. The small, relative displacements of atoms in the ferroelectric phase give rise to electric dipoles, which are, in turn, responsible for the spontaneous polarisation. These atomic movements can occur in opposite directions equally well and the directions of the electric dipoles are thereby reversed. The reversal of the direction of spontaneous polarisation can be effected by the application of an electric field greater than the coercive field (the biassing field) to the ferroelectric crystal or a small electric field above the Curie point.

From the thermodynamic standpoint the question arises: is it a first-order or a second-order transition? It will be recalled that a first-order transition involves a discontinuous change of volume and energy which appears as a rel ase of latent heat in an infinitely narrow temperature range. A second-order transition shows no discontinuity in the

volume or energy but the temperature derivative of volume (thermal expansion coefficient) and of energy (specific heat), show anomalies extending over a finite temperature range. It is not easy to detect changes in these thermodynamic quantities because their discontinuities are very small.

I. 5. Although colemanite has long been known as a common boron-containing mineral found in California, it was only recently that interest had been aroused regarding its physical properties. The study of colemanite in this laboratory was started because of several hints which suggested that the crystal might have very interesting structural properties.

Certain faces of colemanite have sometimes been observed to collect dust particles in mineralogical museums. This is a common feature of crystals exhibiting a spontaneous polarisation. This may be taken to mean that colemanite is sometimes pyroelectric in which case its crystal symmetry would allow it to be ferroelectric. This conjecture would be of great interest because no boron-containing material has been known to exhibit ferroelectricity. It seemed also plausible that colemanite undergoes a phase transition because these certain faces of colemanite tended to attract dust only under special circumstances. These observations, together with the facts that B^{11} is relatively easy to study by n.m.r. technique and the ready availability of large single crystals of colemanite, encouraged the present work.

Before the actual experimental work was begun in this laboratory, Christ et al. (54) had published the preliminary results of an X-ray analysis of colemanite. They found that their results were consistent

with the space-group $P2_1/a$ and the unit cell dimensions were:

$a = 8.743 - 0.004$ Å

$b = 11.264 - 0.002$ Å

$c = 6.102 - 0.003$ Å

$\beta = 110^{\circ}7'$

They found that the structure of colemanite consists of infinite boron-oxygen chains running parallel to the a-axis, the chain element being made up of a BO_3 triangle and two BO_4 tetrahedra forming a ring. Each Ca ion is roughly octahedrally coordinated by 5 oxygens and 1 water molecule. The formula for colemanite may thus be written $CaB_3O_4(OH)_3.H_2O$ and each unit cell contains 4-formula units. Refined colemanite parameters and boron-oxygen bond lengths became available to us by private communication (Clark,'57).

During the preliminary stage of our work Davisson ('56) published the results of his dielectric breakdown studies of colemanite. On the one hand he obtained the centrosymmetric breakdown paths covering a wide temperature range and on the other hand, the pyroelectric and the piezzoelectric tests indicated that colemanite cannot be centrosymmetric.

These two papers leave the symmetry properties of colemanite unsolved.

A little later Goldsmith ('56) discovered that colemanite was indeed ferroelectric. He observed the following ferroelectric behaviour in colemanite: it undergoes a transition at -2.5° C. with the ferroelectric direction along the monoclinic b-axis; it has a very sharp dielectric anomaly with a peak value of 7000 and a half-width of 0.5° C. along the

b-axis and finally its spontaneous polarisation is 5×10^{-17} coul./cm.^{2} . Colemanite displays square hysteresis loops on a plot of the applied electric field versus the dielectric displacement with a coercive field of 10^4 volts/cm. at 60 c./sec. and at -6° C.

Goldsmith's work posed more questions regarding the structure of colemanite. These questions refer to the following:

1. What are the symmetry properties of colemanite below the transition temperature?
2. Which atoms in colemanite structure undergo displacement relative to their room temperature positions?
3 What is the thermodynamic order of the observed transition?
4. Are there other transitions?

In August 1957 Chynoweth ('57), using a refined technique, re-examined the pyroelectric and ferroelectric behaviour of colemanite. He found that the curve of pyroelectric coefficient versus temperature showed a high and narrow peak at -2.5° C., possessed an appreciable tail extending to low temperatures and a rapidly decreasing tail on the high temperature side. He concluded that an ideal single crystal of colemanite would show no pyroelectric effect above the transition temperatures and therefore was consistent with the centrosymmetric point group $^2/m$. Prior to the date of publication of Chynoweth's work, however, we had publicly communicated (Petch,'57) our room temperature results in colemanite, including the fact that we had found its structure consistent with the point group $^2/m$.

Summarising, the problem for this thesis was to use the n.m.r. method to answer at least some of the questions raised in the above discussion and to supply completely new information regarding the physical properties of colemanite.

CHAPTER II

THEORY

II. 1. This chapter outlines the theory of the dependence of the nuclear magnetic resonance frequencies in a single crystal on the orientation of the crystal with respect to the uniform magnetic field, Ho, in which the crystal is immersed. For a particular nucleus in a particular situation, the energy due to the interaction of its quadrupole moment tensor, $\tilde{Q}$, with the electric field gradient tensor, $\tilde{\nabla E}$, existing at its site, is not necessarily small as compared to the interaction of its magnetic moment, $\vec{\mu}$, with the external magnetic field, $\vec{Ho}$. However, this discussion, following Pound ('50), Bersohn ('52), and Volkoff ('53), is restricted to cases where the nuclear electric quadrupole interaction, $\tilde{Q}.\tilde{\nabla E}$, is weak as compared to the nuclear magnetic interaction, $\vec{\mu}.\vec{Ho}$, but large as compared with magnetic dipole-dipole interactions which are neglected. Furthermore, this discussion is limited to cases where the nuclear spin quantum number I is 3/2, since for B^{11}, the case in which we are interested, I equals 3/2.

II. 2. An elementary description of the electric field gradient tensor, $\tilde{\nabla E}$, will be useful in the following pages. $\tilde{\nabla E}$ is a tensor of rank two. In Cartesian coordinates (X, Y, Z), fixed with respect to crystal axes, it has nine components

$$\begin{pmatrix} \phi_{XX} & \phi_{XY} & \phi_{XZ} \\ \phi_{YX} & \phi_{YY} & \phi_{YZ} \\ \phi_{ZX} & \phi_{ZY} & \phi_{ZZ} \end{pmatrix} \qquad \ldots\ldots\ldots\ldots\ldots\ldots\ldots\ldots\ldots\ldots\ldots\ldots\ldots\ldots (1)$$

where $\phi_{XX} = -\partial V/\partial X^2$ etc. with V being the electrostatic potential. Not all components of this tensor are independent. Firstly, it will be recalled that the scalar product, $\vec{\nabla}.\vec{E}$, is equal to zero and is invariant under a coordinate transformation, hence the sum of the diagonal components is always zero. Secondly, the vector product, $\vec{\nabla} \times \vec{E}$, is also zero and is invariant under a coordinate transformation. Hence $\tilde{\nabla E}$ is symmetric, ie., $\phi_{XY} = \phi_{YX}$, etc. Thus only five components are independent.

A symmetric tensor can always be diagonalised; that is, there exists a coordinate system (x, y, z), fixed with respect to the crystal in which the off-diagonal components vanish. When diagonalised the tensor assumes the following form:

$$\begin{pmatrix} \phi_{xx} & 0 & 0 \\ 0 & \phi_{yy} & 0 \\ 0 & 0 & \phi_{zz} \end{pmatrix} = \begin{pmatrix} -[\phi_{zz}(\eta-1)]/2 & 0 & 0 \\ 0 & -[\phi_{zz}(1+\eta)]/2 & 0 \\ 0 & 0 & \phi_{zz} \end{pmatrix} \quad \ldots(2)$$

where $\eta = (\phi_{xx} - \phi_{yy})/\phi_{zz}$ is called the "asymmetry parameter." Since $\phi_{xx} + \phi_{yy} + \phi_{zz} = 0$, the magnitude* of $\tilde{\nabla E}$ is specified by two parameters, in this case ϕ_{zz}, which is chosen to have the largest absolute value of the three eigenvalues , and the asymmetry parameter, η . ϕ_{xx} and ϕ_{yy} are chosen negative with $|\phi_{xx}| < |\phi_{yy}|$. With this definition, the asymmetry parameter is specified within the limits $0 \leq \eta \leq 1$ (At first sight, it might appear that by referring $\tilde{\nabla E}$ to its principal axes the number of independent components has been reduced to two. However, this is not the case because three additional quantities are necessary to specify the orientation of the principal axes (x, y, z) with respect to the (X, Y, Z) system).

---

*The term "magnitude" refers to the eigenvalues of $\tilde{\nabla E}$.

The tensor scalar product, $\tilde{Q}.\ \tilde{\nabla}\tilde{E}$, must be calculated in coordinates that diagonalise the magnetic part of the Hamiltonian Eq.(4), that is, in Cartesian coordinates (x'y'z') whose z' direction coincides with that of Ho and the x and y axes are chosen arbitrarily. Both tensors appearing in this scalar product are expressed in their irreducible forms. The five irreducible tensor components of $\tilde{\nabla}\tilde{E}$ are $\nabla' Eq$ where $q = 0, \pm 1, \pm 2$. Expressed in terms of the components in (x'y'z') system, $\nabla' Eq$ are

$$\nabla' E_0 = -1/2\ \phi x'x'$$

$$\nabla' E_{\pm 1} = \pm \sqrt{6}/6\ (\phi x'z' \pm i\ \phi z'y')$$

$$\nabla' E_{\pm 2} = -\sqrt{6}/12\ (\phi x'x' - \phi y'y' \pm 2i\ \phi x'y')$$

$\tilde{\nabla}\tilde{E}$ reflects strongly the symmetry of a nuclear site.

From the point of view of symmetry, nuclear sites can be identical or non-identical in a unit cell. The non-identical character of nuclear sites arises from two sources:

(a) The formula unit contains more than one atom.

(b) More than one formula unit is allowed to occur in the unit cell by the crystal symmetry.

It is obvious that in case (a) the nuclear sites are unrelated by symmetry. This implies that the magnitudes and orientations of the $\tilde{\nabla}\tilde{E}$'s at these sites are unrelated. We speak of these sites as non-equivalent. In the case (b), starting with any one nuclear site in general position in the crystal structure, other sites can be generated by the operation of the crystal space group. $\tilde{\nabla}\tilde{E}$'s at these

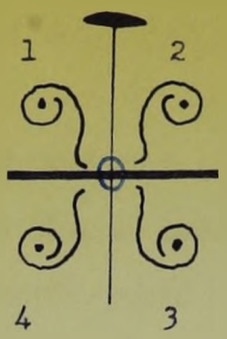

(a)

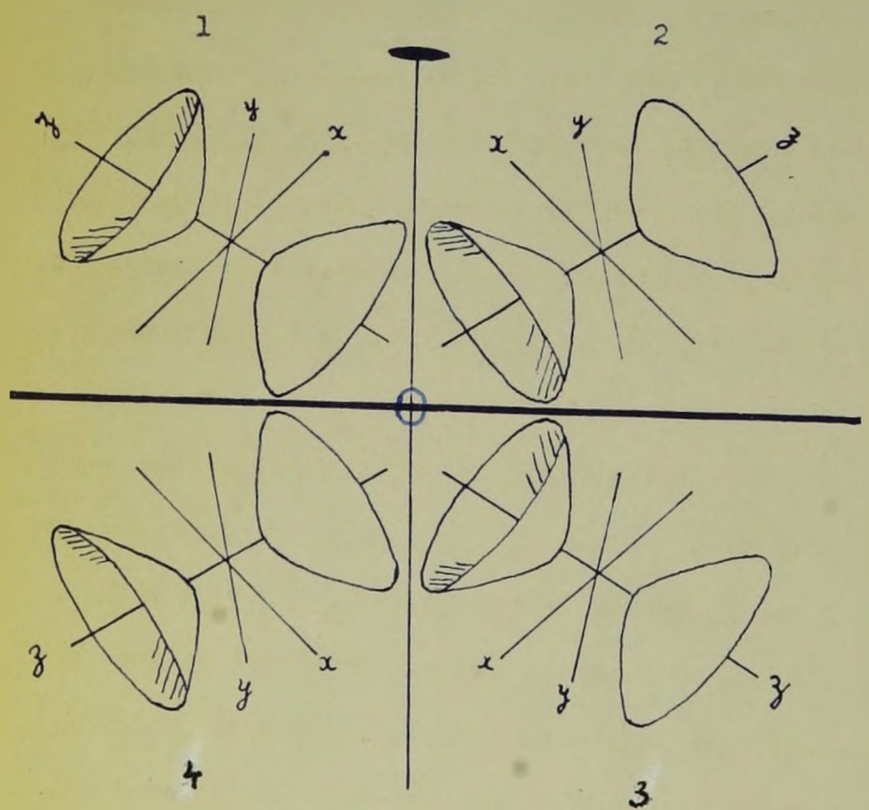

(b)

Fig. 1. (a) Nuclear Sites Related by the Point Group 2/m.
(b) $\nabla\bar{E}$'s Related by the Point Group 2/m.

nuclear sites are then identical in magnitude, but differ in the orientations of their principal axes. We refer to these sites as the symmetry-equivalent sites.

Consider, for example, a nuclear site in a crystal whose point group is 2/m. This point group demands that, in addition to a two-fold symmetry axis, there exists a mirror plane whose perpendicular coincides with the two-fold axis. An equivalent interpretation of this point group is that in addition to the two-fold symmetry axis there exists a centre of symmetry. Fig.1(a) illustrates the inter-relation between the nuclear sites under these circumstances. The sites are represented by dots and brackets each numbered by 1, 2, 3, and 4. 1 and 2, 3 and 4 are related by the two-fold symmetry axis; 1 and 3, 2 and 4 are related by the centre of symmetry. The inter-relation between the $\tilde{\nabla}$E's existing at these sites is illustrated in Fig.1(b) where each $\tilde{\nabla}$E is described by its representative quadric, the hyperboloid of two sheets. The four $\tilde{\nabla}$E's, numbered 1, 2, 3, and 4 in Fig.1(b), are related in the following way. 1 and 2, 3 and 4, by the two-fold symmetry axis, 1 and 3, 2 and 4, by the centre of symmetry. It follows from Fig.1(b) that $\tilde{\nabla}$E denoted by 1 can be derived from that denoted by 3 by translation through the centre of symmetry. The case of 2 and 4 is similar. From the point of view of n.m.r. theory 1 and 3 (or 2 and 4) are identical in all respects. These ideas can be expressed in the tensor notation as follows. The operation of two-fold rotation axis assumed along the Y-axis sends X into -X, Z into -Z but leaves Y unchanged. It follows that the tensor components, ϕ_{XX}, ϕ_{YY}, ϕ_{ZZ}, and ϕ_{ZX} remain

unchanged, but the tensor components ϕ_{ZY} and ϕ_{XY} are sent into $-\phi_{ZY}$ and $-\phi_{XY}$, respectively. Hence $\tilde{\nabla}E$ retains its magnitude but differs only in the orientation of its principal axes. Next, consider the operation of the centre of symmetry on $\tilde{\nabla}E$. This operation sends X into -X, Y into -Y, and Z into -Z. It follows that the tensor components remain unchanged, hence the operation of the centre of symmetry on $\tilde{\nabla}E$ leaves it unchanged in both the magnitude and the orientation of its principal axes.

II. 3. This section is devoted to the calculation of the shift of the nuclear Zeeman levels by the quadrupole effect. We have seen that the Hamiltonian of the nucleus in these circumstances is

$$\mathcal{H} = -\vec{\mu}.\vec{H_o} + F \qquad (4)$$

where $F = \tilde{Q}.\tilde{\nabla}E.$

$$= Q_o \nabla' E_o + Q_{\pm 1} \nabla' E_{\pm 1} + Q_{\pm 2} \nabla' E_{\pm 2}.$$

In the case when $\tilde{Q}.\tilde{\nabla}E$ is much smaller than $\vec{\mu}.\vec{Ho}$, the energy eigenvalues are calculated using the perturbation method. For this purpose we calculate the matrix elements of F in the representation diagonalising the Zeeman energy operator, $-\vec{\mu}.\vec{Ho}$. In their general form, these matrix elements are

$$F_{mm'} = \sum_{q=2}^{-2} \langle \alpha I m | Q_q \nabla' E_q | \alpha I m' \rangle$$

$$= \sum_{q=2}^{-2} \langle \alpha I m | Q_q | \alpha I m' \rangle \nabla' E_q \qquad (5)$$

since $\nabla' E_q$ is assumed to be independent of the nucleus.* Here, m denotes

---

*The contribution of the quadrupolar part to $\tilde{\nabla}E$ is ignored.

the magnetic quantum number, I the angular momentum quantum number, and α the additional quantum number characterising the nucleus. The energy of the perturbed level which in the limit of zero perturbation is characterised by the magnetic quantum number m is given as a sum:

$$U_m = U_m^{(0)} + U_m^{(1)} + U_m^{(2)} + \ldots \qquad (6)$$

where $U_m^{(0)} = - m\mu H_0 / I$

$$U_m^{(1)} = F_{mm}$$

$$U_m^{(2)} = \sum_{m' \neq m} (F_{mm'} F_{m'm}) / (U_m^{(0)} - U_{m'}^{(0)}) \qquad (7)$$

All terms higher than the second have been ignored because they are not generally useful. Substituting Eq.(5) into (7) we get

$$U_m^{(1)} = eQ / [2I(2I-1)][3m^2 - I(I+1)] \nabla' E_0$$

$$U_m^{(2)} = \frac{3e^2Q^2}{[2I(2I-1)]^2} \frac{Im}{\mu H_0} \left\{ |\nabla' E_{\pm 1}|^2 [4I(I+1) - 1 - 8m^2] - |\nabla' E_{\pm 2}|^2 [2I(I+1) - 1 - 2m^2] \right\} \qquad (8)$$

To clearly demonstrate the perturbation of nuclear Zeeman energy levels by the quadrupole effect, Eq.(8) will now be used to calculate the energy levels for B^{11} nuclei at one of the sites in colemanite. Assume a particular orientation of the crystal such that the coordinate axes (X, Y, Z)* arbitrarily fixed in the crystal bear the following relation to (x', y', z') axes fixed in the laboratory:

$$X = y', \quad Y = z', \quad Z = x' \text{ (i.e., } \theta_x = 0)$$

---

*See section III. 2 for definition of (X, Y, Z) system.

Using Eqs.(3), $\nabla' E_q$'s are

$$\nabla' E_0 = -\tfrac{1}{2}\,\phi_{yy}$$

$$\nabla' E_{\pm 1} = \pm \sqrt{6}/6\,(\phi_{zy} \pm i\,\phi_{xy})$$

$$\nabla' E_{\pm 2} = -\sqrt{6}/12\,(\phi_{zz} - \phi_{xx} \pm 2i\,\phi_{zx}) \qquad (9)$$

Inserting the numerical values for I and m into Eq.(8) and substituting Eqs.(9) into Eq.(8), and denoting μ Ho/I by U^o, we get the following energy levels

$$U_{3/2} = -\tfrac{3}{2}\,U^o - h/4\,\Psi_{yy} + Ih/(8\mu Ho)\{-\tfrac{2}{3}(\Psi^2_{zy} + \Psi^2_{xy}) - 1/12\,[(\Psi_{zz} - \Psi_{xx})^2 + 4\,\Psi^2_{xz}]\}$$

$$U_{1/2} = -\tfrac{1}{2}\,U^o - h/4\,\Psi_{yy} + Ih/(24\mu Ho)\{2(\Psi^2_{zy} + \Psi^2_{xy}) - -\tfrac{1}{4}\,[(\Psi_{zz} - \Psi_{xx})^2 + 4\,\Psi^2_{xz}]\}$$

$$U_{-1/2} = \tfrac{1}{2}\,U^o + h/4\,\Psi_{yy} - Ih/(24\mu Ho)\{2(\Psi^2_{zy} + \Psi^2_{xy}) - \tfrac{1}{4}\,[(\Psi_{zz} - \Psi_{xx})^2 + 4\,\Psi^2_{xz}]\}$$

$$U_{-3/2} = \tfrac{3}{2}\,U^o - h/4\,\Psi_{yy} - Ih/(8\mu Ho)\{-\tfrac{2}{3}(\Psi^2_{zy} + \Psi^2_{xy}) - 1/12\,[(\Psi_{zz} - \Psi_{xx})^2 + 4\,\Psi^2_{xz}]\}. \qquad (10)$$

where $\Psi_{ij} = (eQ/h)\,\phi_{ij}$ and is in units of frequency. Using the appropriate values of Ψ_{ij} from Table XII and the experimental value of μHo/Ih (11.981 mc./sec.) we get the following set of energy levels in kc./sec. for B^{11} nuclei at the M sites:

$(U_{3/2})/h$	$(U_{1/2})/h$	$(U_{-1/2})/h$	$(U_{-3/2})/h$
-18331	-5633	6308	17656

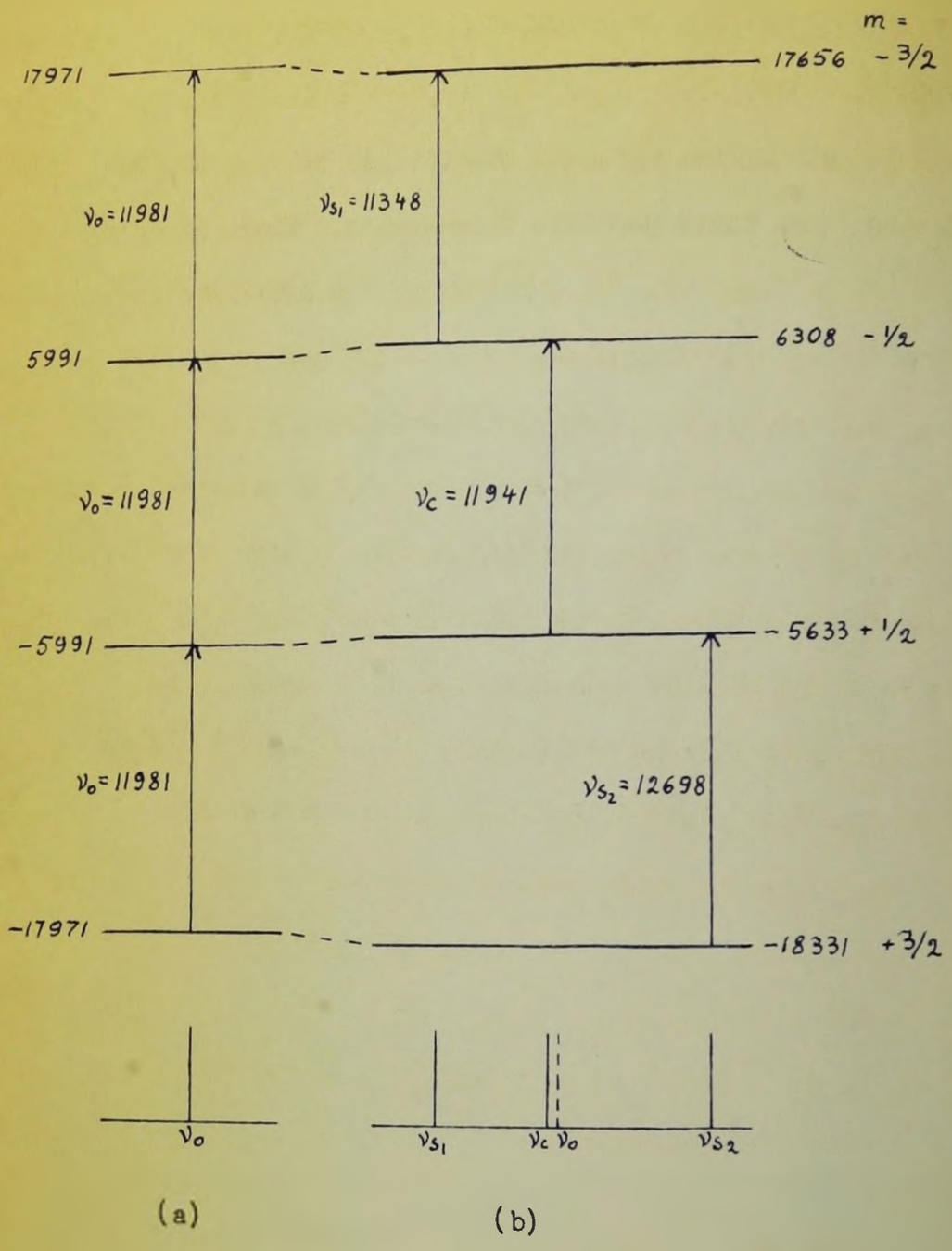

Fig. 2. Nuclear Zeeman Levels, in Mc./Sec., of B^{11} ($I = 3/2$) Nuclei in External Magnetic Field of 8.75 Kilogauss, (a) Not Showing a Quadrupole Interaction, (b) Showing the Quadrupole Interaction at B^{11} Sites M in Colemanite at Room Temperature and at $\Theta x = 0^{\circ}$. The Arrows Show the N.M.R. Transitions. The Spectrum is Drawn at the Bottom.

These energy levels have been drawn to scale in Fig.2(a) and (b). To the left, Fig.2(a), are the unperturbed energy levels given by μ Ho/Ih, i.e., in units of frequency; those to the right, Fig.2(b), are the perturbed levels. The arrows indicate transitions between adjacent levels. For I = 3/2 there are three possible frequencies. They are denoted by ν_{s_1}, ν_c and ν_{s_2} in Fig.2(b). ν_{s_1} and ν_{s_2} are the satellite frequencies corresponding to the transitions $m = \pm 3/2 \leftrightarrow \pm 1/2$ and ν_c denotes the central frequency corresponding to the transition $m = \pm 1/2 \leftrightarrow \mp 1/2$. Except at very low temperatures, there is no way of determining experimentally which of the two satellite frequencies ν_{s_1} and ν_{s_2} corresponds to the transition $m = +3/2 \leftrightarrow +1/2$ and which to $m = -3/2 \leftrightarrow -1/2$. All the transitions in Fig.2(a) have been indicated by a single symbol ν_o.

Additional relationships between ν_{s_1}, ν_o and ν_{s_2} can be obtained from Eq.(8). Inserting values for I and m we get

$$\Delta\nu = \nu_{s_2} - \nu_{s_1} = 2(eQ/h)\,\nabla'E_o + 3^{rd}\ order\ term + \dots \qquad (11)$$

$$\bar{\nu} - \nu_o = (\nu_{s_1} + \nu_{s_2})/2 - \nu_o = (eQ/h)^2\, 1/\nu_o\, |\nabla'E_{\pm 1}|^2 + 4^{th}\ order\ term + \dots \qquad (12)$$

$$\nu_c - \nu_o = (eQ/h)^2\, 1/\nu_o\, (1/2\, |\nabla'E_{\pm 1}|^2 - |\nabla'E_{\pm 2}|^2) + 4^{th}\ order\ term + \dots \qquad (13)$$

in units of frequency. $\bar{\nu} = (\nu_{s_1} + \nu_{s_2})/2$ is called the centre of gravity of the satellite frequencies and ν_o is the unperturbed frequency, $|\mu H_o/Ih|$. Eqs.(11)-(13) show that, if the second-order terms are negligible, the two satellite frequencies are symmetrically situated below and above the central frequency, ν_c, which in this case coincides

with ν_o . If the second-order terms are not negligible they show that the centre of gravity of the satellite frequencies and the central component no longer coincide with ν_o . This is demonstrated at the bottom of Fig.2(b) where the n.m.r. spectrum of B^{11} has been drawn to scale. The frequency ν_o is represented there by the broken line.

II. 4. Eqs.(3) and (11)-(13) show that by measuring the spectra at five different crystal orientations with respect to Ho one can determine the five independent components of ∇ E. This, however, would hardly constitute a satisfactory experiment for the following reasons. The satellite lines, belonging to the same nuclear site, depend strongly on the crystal orientation with the result that they may cross and overlap. This makes the identification of the lines difficult. These difficulties increase when the complete n.m.r. spectrum consists of 2nI-lines, where n is the number of both the non-equivalent and the symmetry-equivalent nuclear sites in the unit cell. Another important reason is that the accuracy of the experimental results would then be very low. For these reasons a systematic investigation of the spectra is necessary. It permits not only a reliable classification of the lines but also increases experimental accuracy. A scheme for such investigation was first developed by Volkoff et al ('52).

In Volkoff's scheme we select a set of axes (X, Y, Z) fixed with respect to the crystal (for example, this set may involve some of the crystallographic axes), and study the relation between the components of ∇E in this system of axes, and in the laboratory system of axes

(x', y', z') as the crystal is rotated about, say, its X axis which is kept in coincidence with the y' axis perpendicular to Ho. The initial position of the crystal, in which the angle of rotation is zero, is chosen so that Y, Z coincide with z', x'. The transformation between (X, Y, Z) and (x', y', z') is given by

$$X = y'$$

$$Y = \cos\theta_x \, z' + \sin\theta_x \, x'$$

$$Z = -\sin\theta_x \, z' + \cos\theta_x \, x' \qquad (14)$$

The tensor components in the (x', y', z') system are related to those in the (X, Y, Z) by the transformation law:

$$\phi_{q_i' q_j'} = \sum_{\alpha,\beta} \phi_{Q_\alpha Q_\beta} \frac{\partial Q^\alpha}{\partial q_i'} \frac{\partial Q^\beta}{\partial q_j'} \qquad (15)$$

where Q refers to the (X, Y, Z) system, while q' to (x', y', z') system, α , β , i and j each take the values 1, 2, 3, and $\phi_{q_i' q_j'}$, $\phi_{Q_\alpha Q_\beta}$ are the tensor components in (x', y', z') and (X, Y, Z) system, respectively. Using Eq.(14) and (15) we get

$$\phi_{z'z'} = \sum_{\alpha,\beta} \phi_{Q_\alpha Q_\beta} \frac{\partial Q^\alpha}{\partial z'} \frac{\partial Q^\beta}{\partial z'}$$

$$= 1/2(\phi_{YY} + \phi_{ZZ}) + 1/2(\phi_{YY} - \phi_{ZZ}) \cos 2\theta_x - \phi_{YZ} \sin 2\theta_x \qquad (16)$$

Similar relationships hold for $\phi_{x'x'}$, $\phi_{y'y'}$, etc. Substituting these relationships into (3) we get

$$\nabla' E_0 = 1/4\,(\phi_{yy} + \phi_{zz}) + 1/4\,(\phi_{yy} - \phi_{zz})\cos 2\theta_x - 1/2\,\phi_{zy}\sin 2\theta_x$$

$$\nabla' E_{\pm 1} = 1/\sqrt{6}\,\{\mp[\phi_{yz}\cos 2\theta_x + 1/2\,(\phi_{yy} - \phi_{zz})\sin 2\theta_x] - i\,(\phi_{xy}\cos\theta_x - \phi_{zx}\sin\theta_x)\}$$

$$\nabla' E_{\pm 2} = 1/\sqrt{24}\,[3/2\,(\phi_{yy} + \phi_{zz}) - 1/2\,(\phi_{yy} - \phi_{zz})\cos 2\theta_x + \phi_{yz}\sin 2\theta_x \pm 2i\,(\phi_{zx}\cos\theta_x + \phi_{xy}\sin\theta_x)] \qquad (17)$$

Substituting (17) into Eqs.(11)-(13) and introducing* $\psi_{ij} = eQ/h\ \phi_{ij}$ we get the following equations:

$$\Delta\nu_x = a_x + b_x\cos 2\theta_x + c_x\sin 2\theta_x \qquad (18)$$

where

$$a_x = 1/2\,(\psi_{yy} + \psi_{zz})$$
$$b_x = 1/2\,(\psi_{yy} - \psi_{zz})$$
$$c_x = -\psi_{zy} \qquad (19)$$

---

*For reasons discussed earlier the experimental results appear in terms of ψ_{ij}. The symbol ψ_{ij} is reserved for the ∇E components ϕ_{ij} times the constant eQ/h. Thus $\psi_{xx} = eQ/h\ \phi_{xx}$, $\psi_{x'x'} = eQ/h\ \phi_{x'x'}$ etc.

$$(\bar{\nu} - \nu_0)_x = \bar{n}_x + \bar{p}_x \cos 2\theta_x + \bar{r}_x \sin 2\theta_x + \bar{u}_x \cos 4\theta_x + \bar{v}_x \sin 4\theta_x \qquad (20)$$

where,

$$\bar{n}_x = 1/(12\nu_0)\,(6_x^2 + c_x^2 + c_y^2 + c_z^2)$$

$$\bar{p}_x = -1/(12\nu_0)\,(c_y^2 - c_z^2)$$

$$\bar{r}_x = -1/(6\nu_0)\,c_y c_z$$

$$\bar{u}_x = -1/(12\nu_0)\,(6_x^2 - c_x^2)$$

$$\bar{v}_x = -1/(6\nu_0)\,6_x c_x \,. \qquad (21)$$

$$(\nu_c - \nu_0)_x = n_x + p_x \cos 2\theta_x + r_x \sin 2\theta_x + u_x \cos 4\theta_x + v_x \sin 4\theta_x, \qquad (22)$$

where,

$$n_x = 1/(96\nu_0)\,[18\,a_x^2 - 7(6_x^2 + c_x^2) - 4(c_y^2 + c_z^2)]$$

$$p_x = 1/(8\nu_0)\,(-a_x 6_x - c_y^2 - c_z^2)$$

$$r_x = 1/(8\nu_0)\,(a_x c_x + 2\,c_y c_z)$$

$$u_x = 3/(32\nu_0)\,(6_x^2 - c_x^2)$$

$$v_x = 3/(16\nu_0)\,6_x c_x \,. \qquad (23)$$

Similar relations hold for the Y and Z rotations by cyclic permutation

of the subscripts. Eqs.(19) show that the coefficients a_i, b_i, and c_i in the three rotations are related by the following identities:

$$a_x = 1/2\,(b_y - a_y) = -1/2\,(b_z + a_z)$$

$$b_x = -1/2\,(3a_y - b_y) = 1/2\,(3a_z - b_z) \qquad (24)$$

Eqs.(24) are useful in checking the consistency of the experimental data.

As can be seen from Eqs.(11)-(13) and from Eqs.(18)-(24), the separation of the satellites $\Delta\nu = \nu_{s_2} - \nu_{s_1}$ is independent of ν_o and so independent of Ho, if the third-order term is neglected. For this reason the coefficients a_i, b_i, and c_i are sometimes referred to as the first-order coefficients. The separation of the centre of gravity of the satellite frequencies from the unperturbed frequency, ν_o , $\bar{\nu} - \nu_o$, and the separation of the central component from ν_o, $\nu_c - \nu_o$ are entirely dependent upon the second-order term (again, if we neglect the fourth-order term, etc.) and so are inversely proportional to Ho. For this reason the coefficients $\bar{n}_i$ etc. and n_i etc. are referred to as the second-order coefficients. If the second-order term is large one single rotation determines the five independent tensor components ψ_{ij} as follows: an analysis of $\Delta\nu_i$ gives the three diagonal components plus the component ψ_{jk}. The remaining components ψ_{ik} and ψ_{ij} can be got from the second-order coefficients. However, this procedure would result in a low experimental accuracy. The three rotations are therefore necessary from the point of view of improving the experimental accuracy.

Having determined the tensor ψ_{ij} in X, Y, Z coordinates we may now refer it to its principal axes (x, y, z) by determining its eigenvalues and the direction cosines of (x, y, z) with respect to (X, Y, Z). The characteristic equation for the eigenvalues, γ , is the equation

$$\gamma^3 - a\gamma - b = 0 \tag{25}$$

where

$$a = \psi_{xy}^2 + \psi_{yz}^2 + \psi_{zx}^2 - \psi_{xx}\psi_{yy} - \psi_{yy}\psi_{zz} - \psi_{zz}\psi_{xx} \tag{26}$$

$$b = \psi_{xx}\psi_{yy}\psi_{zz} + 2\psi_{xy}\psi_{yz}\psi_{zx} - \psi_{xx}\psi_{yz}^2 - \psi_{yy}\psi_{zx}^2 - \psi_{zz}\psi_{xy}^2 \tag{27}$$

The reversal of signs of ψ_{ij} leaves the sign of a of Eq.(26) unchanged but it reverses the sign of b of Eq.(27). The undetermined common sign of ψ_{ij} is always chosen so that $b = |b|$.

The trigonometric solution of the cubic equation with three real roots is

$$\gamma_n = 2\,(a/3)^{1/2} \cos(\alpha - 2\pi n/3) \tag{28}$$

where

$$n = 1, 2, 3$$

and

$$\cos 3\alpha = |b|/2\,(3/a)^{3/2}.$$

γ_3 is always positive while γ_2 and γ_1 are always negative and $|\gamma_3| > |\gamma_2| > |\gamma_1|$.

If we denote the principal axes of the tensor ψ_{ij} by (unprimed) (x, y, z) then γ_n are defined as:

$$\gamma_3 = \psi_{zz} = eQ/h\ \phi_{zz}$$
$$\gamma_2 = \psi_{yy} = eQ/h\ \phi_{yy}$$
$$\gamma_1 = \psi_{xx} = eQ/h\ \phi_{xx} \qquad (30)$$

As it was shown earlier we define the asymmetry parameter as

$$\eta = (\gamma_1 - \gamma_2)/\gamma_3 = (\phi_{xx} - \phi_{yy})/\phi_{zz} \qquad (31)$$

γ_3 is also frequently called the "quadrupole coupling constant."

The process of diagonalisation also gives the direction cosines of the principal axes (x, y, z) with respect to the axes (X, Y, Z),

$$\lambda_n/D_{1n} = \mu_n/D_{2n} = \nu_n/D_{3n} = \pm 1/(D_{1n}^2 + D_{2n}^2 + D_{3n}^2)^{1/2} \qquad (32)$$

where

$$D_{1n} = \psi_{xy}\psi_{y2} - \psi_{zx}(\psi_{yy} - \gamma_n)$$
$$D_{2n} = \psi_{yx}\psi_{x2} - \psi_{zy}(\psi_{xx} - \gamma_n)$$
$$D_{3n} = (\psi_{xx} - \gamma_n)(\psi_{yy} - \gamma_n) - \psi_{xy}^2 \qquad (33)$$

The relative signs of λ_n, μ_n and ν_n for each value of γ are fixed by the relative signs of D_{1n}, but not their absolute sign, because for the second rank tensor, ψ_{ij}, it does not matter which direction along a principal axis is chosen to be the positive one.

II. 5. The theory developed above is adequate for a full analysis of the n.m.r. spectra, simple or complex.* If the complex spectrum is investigated in a crystal possessing a two-fold symmetry axis, mirror plane, etc., and if one of the axes about which the crystal is rotated coincides with the direction of these symmetry elements, then the second-order term is very helpful in the analysis of the spectra, because of the following. Consider a crystal with the point group 2/m, the case in which we are especially interested. It was shown previously that an operation of two-fold symmetry axis, coinciding with Y-axis, on $\tilde{\nabla}E$ leaves its magnitude unchanged but changes the orientation of its principal axes, and that the two tensors have the form (correct to a relative sign),

$$\begin{pmatrix} \phi_{xx} & \phi_{xy} & \phi_{xz} \\ \phi_{yx} & \phi_{yy} & \phi_{yz} \\ \phi_{zx} & \phi_{zy} & \phi_{zz} \end{pmatrix} \text{ and } \begin{pmatrix} \phi_{xx} & -\phi_{xy} & \phi_{xz} \\ -\phi_{yz} & \phi_{yy} & -\phi_{yz} \\ \phi_{zx} & -\phi_{zy} & \phi_{zz} \end{pmatrix} \qquad (34)$$

Experimentally, however, the two tensors are determined in the form

$$\begin{pmatrix} \phi_{xx} & |\phi_{xy}| & \phi_{xz} \\ |\phi_{yx}| & \phi_{yy} & |\phi_{yz}| \\ \phi_{zx} & |\phi_{zy}| & \phi_{zz} \end{pmatrix} \qquad (35)$$

---

*The term, "simple spectrum," refers to the n.m.r. spectrum consisting of 2I lines, the term, "complex spectrum," refers to the one consisting of 2nI lines, where n is the number of non-equivalent or symmetry-equivalent nuclear sites.

The problem is, what combination of signs in front of ϕ_{xy} and ϕ_{zy} is the correct one? An inspection of the sign of $\bar{r}_i$ in Eq.(21) and the value of r_i in Eq.(22) furnishes an answer to this problem only if the second-order term is measurable. If, however, the second-order term in not measurable one has to modify the experimental procedure in one of the three ways. Firstly, one can reduce Ho until the second-order term is measurable. However, the measurements of n.m.r. spectra at low fields are inherently more difficult than at high fields. Secondly, one can make a different choice of axes (X, Y, Z) so that none of them coincides with the axis of symmetry. This, however, may be objectionable from both the experimental point of view and from the point of view of analysis of the spectra. Thirdly, one conducts the experiment as if the second-order term were present except that a few additional measurements of the n.m.r. spectra are made with the crystal oriented in such a way that none of the (X, Y, Z) axes are either parallel or perpendicular to Ho. Since this procedure is not mentioned in the literature it is fully developed below.

Consider an orientation of the crystal such that the laboratory axes (x', y', z') have (l_i, m_i, n_i) for their direction cosines in (X, Y, Z) system. Using the transformation law, Eq.(15), we arrive at the following relations between $\phi_{\xi_i' \xi_j'}$ and $\phi_{Q_\alpha Q_\beta}$,

$$\phi_{x'x'} = \phi_{xx} l_3^2 + \phi_{yy} m_3^2 + \phi_{zz} n_3^2 + 2(\phi_{xy} l_3 m_3 + \phi_{yz} m_3 n_3 + \phi_{zx} n_3 l_3)$$

$$\phi_{y'y'} = \phi_{xx} l_2^2 + \phi_{yy} m_2^2 + \phi_{zz} n_2^2 + 2(\phi_{xy} l_2 m_2 + \phi_{yz} m_2 n_2 + \phi_{zx} n_2 l_2)$$

$$\phi x'x' = \phi_{XX}\, l_1^2 + \phi_{YY}\, m_1^2 + \phi_{ZZ}\, n_1^2 + 2(\phi_{XY}\, l_1 m_1 + \phi_{YZ}\, m_1 n_1 + \phi_{ZX}\, l_1 n_1)$$

$$\phi x'y' = \phi_{XX}\, l_1 l_2 + \phi_{YY}\, m_1 m_2 + \phi_{ZZ}\, n_1 n_2 + \phi_{XY}(l_1 m_2 + l_2 m_1) + \phi_{YZ}(m_1 n_2 + m_2 n_1) + \phi_{ZX}(n_1 l_2 + l_1 n_2)$$

$$\phi y'z' = \phi_{XX}\, l_2 l_3 + \phi_{YY}\, m_2 m_3 + \phi_{ZZ}\, n_2 n_3 + \phi_{XY}(l_2 m_3 + l_3 m_2) + \phi_{ZX}(l_2 n_3 + l_3 n_2) + \phi_{YZ}(m_2 n_3 + m_3 n_2)$$

$$\phi z'x' = \phi_{XX}\, l_1 l_3 + \phi_{YY}\, m_1 m_3 + \phi_{ZZ}\, n_1 n_3 + \phi_{XY}(l_1 m_3 + l_3 m_1) + \phi_{YZ}(m_1 n_3 + m_3 n_1) + \phi_{ZX}(n_3 l_1 + n_1 l_3) \qquad (36)$$

Inserting these values into Eqs.(11)-(13), using also Eq.(3), we can predict $\Delta\nu$, $\bar{\nu} - \nu_0$ and $\nu_c - \nu_0$ for this particular crystal orientation. Actually, only the value of $\phi x'x'$ needs to be calculated for our purpose; the additional calculation of $\bar{\nu} - \nu_0$ and of $\nu_c - \nu_0$ is desirable for checking purposes.* The two combinations of signs in front of ϕ_{XY} and ϕ_{ZY}, for example, $(+\phi_{XY}, +\phi_{ZY})$ and $(-\phi_{XY}, +\phi_{ZY})$ are tried in calculating $\Delta\nu$ from Eq.(36). The correct combination predicts the experimentally measured $\Delta\nu$.

A summary of the methods of analysis of the experimental results will be appropriate in concluding this chapter. The coefficients of Eq.(18) are determined by the Fourier analysis of the experimental values

---

*The calculation of the second-order term for sites which do not display it is, of course, pointless. However, such calculation in the case of other sites, whose second-order term is measurable, serve as a reliable check on whether the axes (X, Y, Z) have been followed consistently both during the three rotations of the crystal and during these additional measurements.

of $\Delta\nu$. These Fourier coefficients are next used to determine the tensor components Ψ ij with the aid of Eq.(19). The experimental values of $(\bar{\nu}-\nu_o)$ and $(\nu_c-\nu_o)$, if measurable, are treated similarly. In this way we obtain the second-order Fourier coefficients. If present, $\bar{r}_i$ and r_i are used to identify the symmetry equivalent ∇E in the manner indicated above. If they are absent, additional measurements are made as described above. The tensor Ψij is finally diagonalised using Eqs.(25)-(28) and the direction cosines of its principal axes determined using Eqs.(32) and (33).

CHAPTER III

APPARATUS AND EXPERIMENTAL PROCEDURE

III. 1. This chapter describes briefly the n.m.r. spectrometer and ancillary equipment used in this work. A complete description of the spectrometer is given by Datars ('56).

The magnetic field was produced by a 12" Varian electromagnet. The magnet pole-faces measured 12" in diameter and the gap between them was 5". Two sets of caps were available which, when attached to the pole-faces, produced gaps 1 1/2" in width by 7" in diameter and 3" in width by 7" in diameter. The work with the crystal at room temperature was carried out using the 1 1/2" gap. The 3" gap was used for the work at other crystal temperatures because it afforded more space for the cold-cell.

The magnet, energised by a stabilised power-supply, provided a field with long- and short-term stabilities of 2:100,000 and 1:100,000, respectively, in the current range from 0.02 to 2 amperes, provided the temperature of the room was held constant. Variations in the field due to temperature changes in the laboratory were compensated by manual adjustment of the current; a proton signal displayed on an oscilloscope served as a field-monitor.

A block diagram of the n.m.r. spectrometer is shown in Fig.3. The oscillating-detector, similar to the Volkoff, Petch and Smellie type, consists essentially of a marginal oscillator of the Colpitts type, a

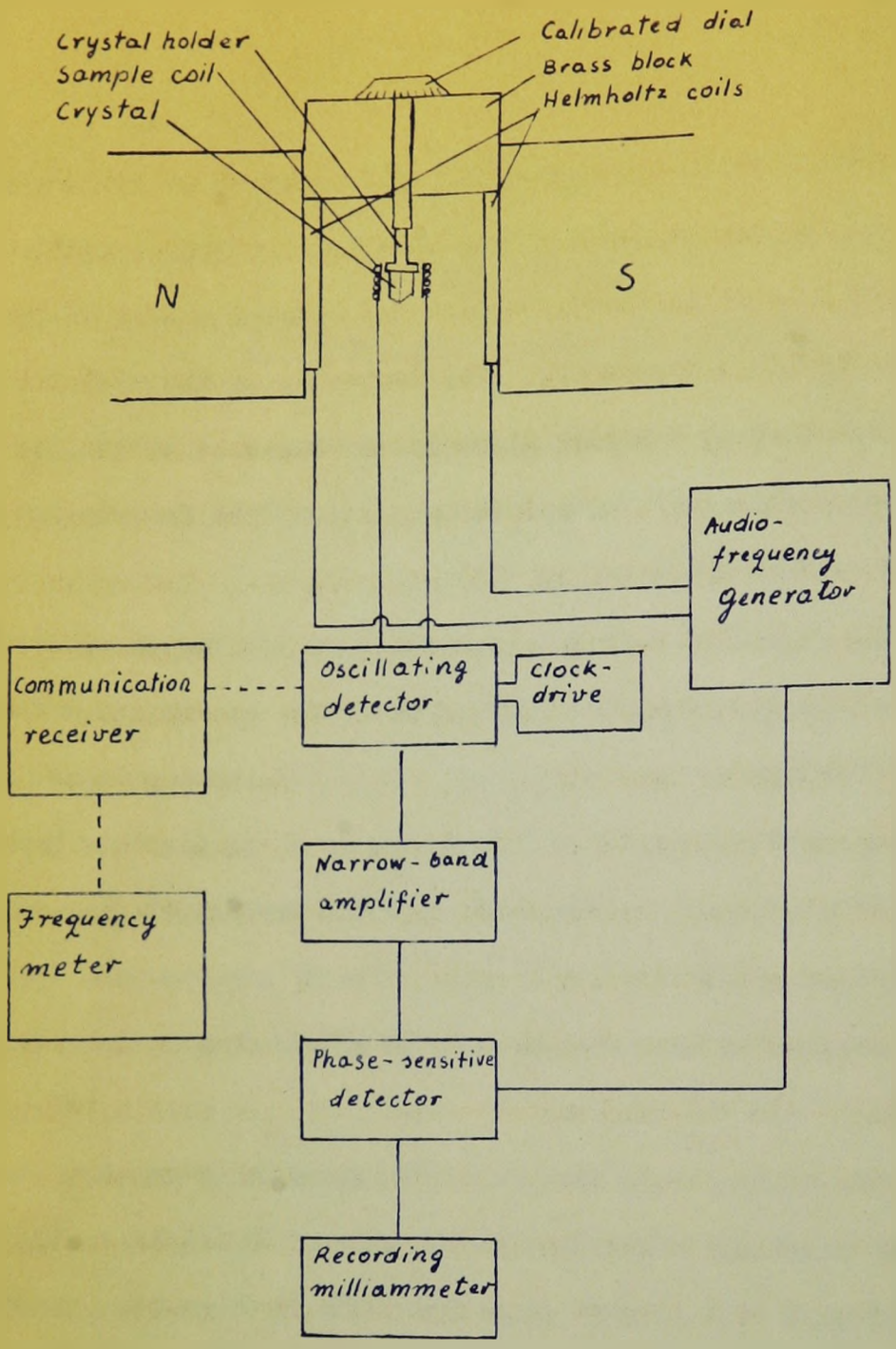

Fig. 3. A Block Diagram of a N.M.R. Spectrometer.

radio-frequency amplifier, a detector, and a wide-band audio-frequency amplifier. The tank circuit of the marginal oscillator consists of a sample coil, located inside the magnet gap between a pair of Helmholtz coils and a variable condenser. The frequency of the oscillating detector is varied by a Haydon clock-drive connected to the variable condenser through a chain of reduction gears. The frequency sweep-rate mostly employed in this work was 250 kc./sec./hr. The Helmholtz coils are energised by a 210 c./sec. alternating current supplied by the audio-frequency power amplifier. Other parts of the spectrometer are: a narrow-band amplifier tuned to 210 c./sec., a phase-sensitive detector, and a recording milliammeter. The frequency is measured with the aid of a Hallicrafter Radio model 5X-62A and a General Radio heterodyne frequency meter and calibrator type No. 620-A.

The spectrometer functions in the following way. The Helmholtz coils modulate the external magnetic field with an amplitude much smaller than the width of a n.m.r. signal (of the order of 3 gauss in crystals). The resonance condition for the nuclei inside the sample coil, which manifests itself as a drop of potential difference across the coil, is thus made repetitive at the modulation frequency. The signal, after radio-frequency amplification, is detected and then fed to the wide-band audio-frequency amplifier, the narrow-band audio-frequency amplifier and finally to the phase-sensitive detector which produces a d.c. signal approximately proportional to the first derivative of the absorption curve. The d.c. signal is plotted on the recording milliammeter. At suitable intervals frequency markers are accurately placed on the recorder chart.

The orientation of a crystal with respect to the external magnetic field, Ho, has to be accurately known at all stages of n.m.r. work. An accurately calibrated angle-measuring device meets this demand. The angle-measuring device employed for the room temperature work is sketched in Fig. 3. It consisted of a brass block which could be adjusted by a set of screws to fit tightly between the magnet pole-faces and a calibrated dial assembly. The calibrated dial assembly could rotate in the brass block with its axis of rotation always held perpendicular to Ho. The dial was calibrated at one degree intervals and, with the aid of a magnifying glass, relative measurements could be repeated to better than half a degree. Lucite crystal mounts were, in turn, held by the dial assembly. Several lucite mounts, with shapes machined to fit the colemanite crystals in their particular orientations, were used. This arrangement allowed accurate alignment of the crystal.

III. 2. A qualitative investigation of the B^{11} n.m.r. spectrum in colemanite preceded the quantitative investigation. The purpose of this investigation was to establish the maximum number of resonance lines and the frequency region in which they occur for a given Ho. A number of crystals and cleavage fragments of colemanite from Inyo and San Bernardino Counties in California were used in this particular study.

Colemanite has a perfect cleavage plane parallel to the (010) plane and consequently the crystallographic b-axis is well defined. In addition, several available crystals had an edge defining the crystallographic c-axis. Several of these crystals were oriented on their mounts with these crystallographic axes in turn parallel to the rotation axis of

the calibrated dial assembly, and their B^{11} n.m.r. signals investigated. From most of these samples, the signals were found to be very broad. Ordinarily this would not be very serious, but, in the case of colemanite, the separation between many lines, which were later identified as belonging to K and L sites, were unusually small, so that their excessive breadth made their resolution impossible over a wide range of crystal orientations. Also some lines, later identified as belonging to the M site, were so broadened at certain crystal orientations that it was not possible to detect them. Finally, a cleavage fragment from San Bernardino County, which, judging from its outer appearance did not differ markedly from other samples already tried unsuccessfully, gave the desired narrow signals which were detectable at all crystal positions. Since this particular crystal was used throughout the present work we may note its physical appearance. It was a transparent cleavage fragment, measuring 1 1/2 cm. x 1 cm. x 2 cm. after it had been ground. In addition to a perfect cleavage which defined the (010) plane, it had a 2 cm. edge which defined the c-crystallographic axis. The crystallographic axes were verified with the aid of X-rays. Because of these external crystal features the set of (X,Y,Z) axes was chosen as follows: the $\vec{b} \times \vec{c}$ crystal direction defined the X-axis, the $\vec{b}$ direction the Y-axis and the $\vec{c}$ direction the Z-axis. Henceforth we shall use X, Y, Z to denote these crystal directions.

For the systematic investigation, the axes X, Y, Z were held in turn accurately parallel to the axis of rotation of the calibrated dial assembly and the B^{11} n.m.r. spectra were recorded at many crystal orientations. The orientation for which the X-axis was along the rotation

axis and the Y-axis along the direction of Ho is marked $\theta_x = 0$. It was checked against the cross-over points of the lines denoted by $\nu_{s_1}^{M_{1,3}}$ and $\nu_{s_4}^{M_{2,4}}$, $\nu_{s_3}^{M_{1,3}}$ and $\nu_{s_2}^{M_{2,4}}$ in Fig.6, Chapter IV. These cross-over points occurred exactly at the dial reading 0°, 90°, 180°, and 270°. A similar procedure was used when the crystal had its Z-axis along the rotation axis. The $\theta_z = 0^\circ$ orientation was marked by the cross-over points of the same lines as shown in Fig.9, Chapter IV. The procedure used in aligning the crystal with its Y-axis parallel to the rotation axis differed somewhat from the above. This difference arose from the fact that in this case a reduced spectrum was obtained. Accordingly, the crystal alignment for the Y-rotation was checked by comparing the spectra obtained at $\theta_y = 0$ and 90° with those obtained at $\theta_x = 90^\circ$ and $\theta_z = 0^\circ$, respectively. The reduced spectrum was obtained in the range $\theta_y = 0$ to $\theta_y = 180^\circ$. In the range $\theta_y = 180^\circ$ to $\theta_y = 360^\circ$, however, small splittings of the lines marked by $\nu_{s_1}^{M}$ and $\nu_{s_2}^{M}$ in Fig.8, Chapter IV, occurred. Normally such small splittings would have been disregarded as arising from a slight misalignment of a crystal. In our case, however, since there was a controversy regarding the symmetry properties of colemanite, it was essential to know whether such splittings were due simply to a misalignment or due to an inherent property of colemanite, or both. When the crystal was re-examined, using a goniometer arc set in the crystal mount, the splitting of these lines no longer appeared and therefore, this proved that the splittings were due to misalignment.

The B^{11} n.m.r. spectra were recorded at 15° intervals in the range 0° - 360° for each of the three crystal rotations. The spectra

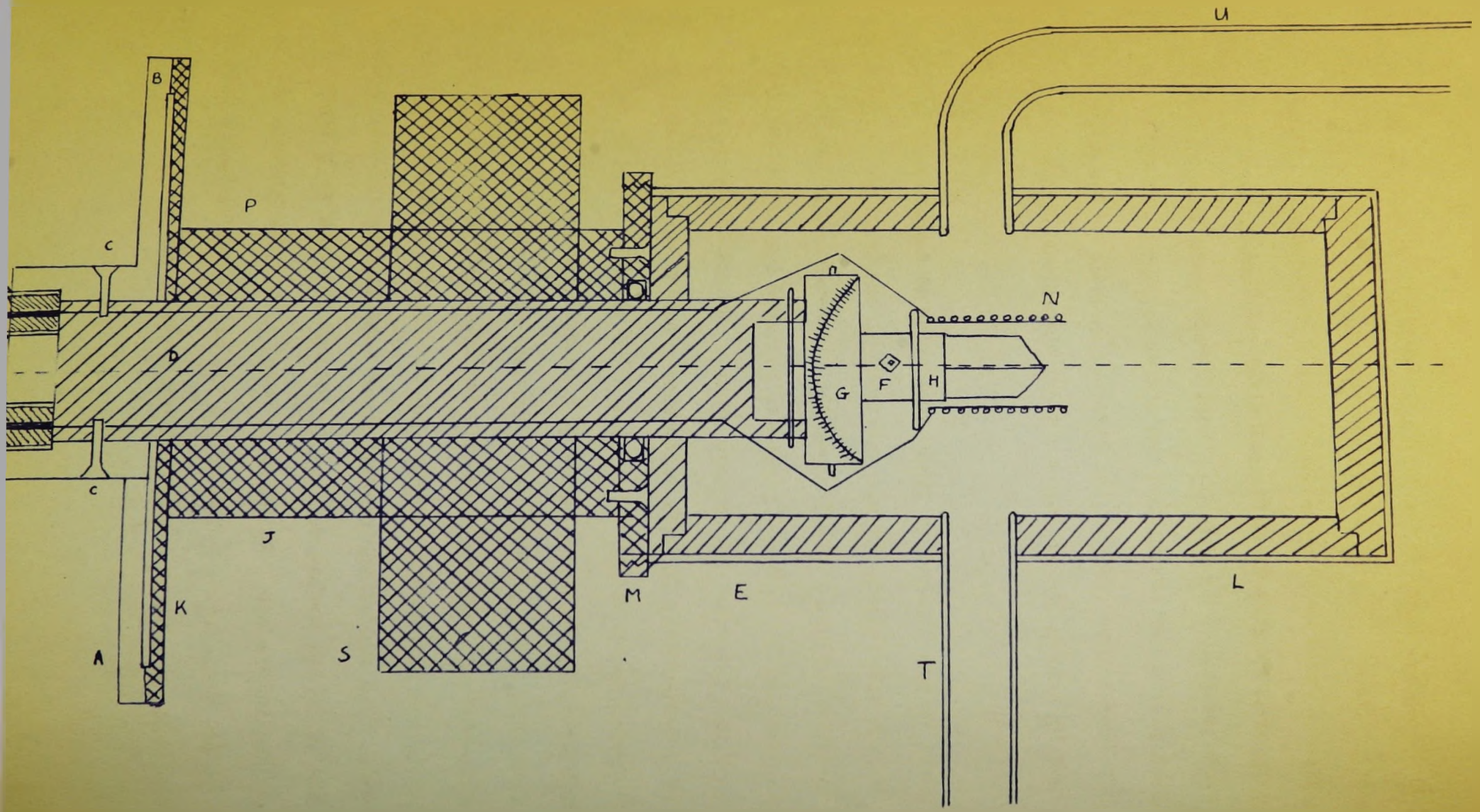

Fig.4. A Cross-Section of the "Cold-Cell."

were very complicated, and it was difficult to sort out the lines. It was therefore necessary to re-examine the spectra over some regions at smaller intervals of from 2^{o} to 5^{o} with higher resolution. If two particular lines belonging to different sites overlapped, their frequencies were determined by interpolation. Some lines belonging to K and L sites overlapped throughout the entire Z-rotation. The experimental frequencies used in the complete analysis of the spectra were obtained by taking the averages between the values measured at θ^{o} and $180^{o}+\theta^{o}$.

III. 3. Since it was planned to study colemanite at temperatures other than that of the laboratory, it was necessary to construct the apparatus which is described below. Fig.4 shows the cross-section of the "cold-cell" which, for all intents and purposes, replaced the calibrated dial assembly used for the room temperature work. The rotator-mount assembly consists of a teflon rod, D, with calibrated circular scale, A, at one end and a crystal mount at the other end. The circular scale is attached to a perspex disc, B, which, by means of a pair of screws, C, is attached to the teflon rod. The crystal mount consists of a Unicam single crystal goniometer arc set incorporating two mutually perpendicular arc sets, G and F, and a platform of brass and lucite, H, to which a crystal can be glued. One end of the crystal mount fits tightly into the socket provided for it in the teflon rod and is secured in position by means of a pin, E. The sample coil, N, which is wound around the crystal, is connected to the oscillating detector via two copper wires, P, embedded in the teflon rod, a pair of amphenol connectors, R, and two coaxial cables.

This rotator-mount assembly is received into the brass block, J, with the teflon rod fitting tightly into a carefully machined and polished cylindrical hole, and with the circular scale fitting into a socket provided for it in the brass disc, K. K also carried a circular vernier. The brass block, which is expanded by means of two screws, fits tightly between the magnet pole-faces so that the axis of rotation of the rotator-mount assembly is accurately perpendicular to the magnetic field. The cylinder, L, is attached to the brass block by means of a screw-on cap, M. The inside of the cylinder is lined with teflon. L also carries an inlet and an outlet pipe which are bent in the manner indicated in Fig.4. The apparatus was assembled as shown and was rendered air-tight by a system of O-rings. The use of the expensive teflon was dictated by the fact that it has nearly the same thermal expansion coefficient as brass at low temperatures and because no lubrication is necessary on well polished metal-teflon contacts.

The cold-cell was cooled by a stream of cold, dry air which was circulated through the cell and a heat exchanger by means of a vacuum pump and compressor. The heat exchanger consisted of three copper coils connected in series. One terminal of the series was connected to the compressor-end of a "Speedivac Combined Compressor and Vacuum Pump," model RB/4, manufactured by Edwards High Vacuum Ltd., while the other terminal was joined to the cold-cell by means of the copper tube, T, of Fig.4. The copper tube, U, on the same diagram, was connected to the vacuum-end of the pump. The three copper coils forming the series were designated as follows: the one nearest to the pump was

designated the first coil; the next one, the drying coil; and the last one, the cooling coil. The first coil was immersed in a cold water bath and served to precool the hot air issuing from the pump. The drying coil served essentially as a trap for oil and moisture which had joined the stream of air during its passage through the pump. The cooling coil served to bring the temperature of the air stream to that of the refrigerant to maintain the crystal temperature at -40° C. The latter two coils were both immersed in an acetone-dry-ice bath. To attain crystal temperatures in the range -40° to -136° C. the drying coil and the cooling coil were immersed in dry-ice and liquid air, respectively. For other temperature ranges the drying coil was omitted.

The 60° C. to 25° C. range was produced by controlled heating of an ethylene glycol bath, whereas the range 25° C. to -40° C. was produced by cooling the bath using a "Blue M Electric Portable Cooling Unit," model PCC4. For fine control of the crystal temperatures the speed of pumping of the air stream was varied or the air stream was allowed to impinge upon a heated metal surface before it entered the cold-cell. The metal tubes connecting the cold-cell to the cooling coil were thermally insulated either with styrofoam sheaths or glass-wool jackets.

The temperatures of the crystal were measured by means of a standardised copper-constantan thermocouple. One junction of the thermocouple was always kept in an ice-water mixture, whereas the other was inserted into the cold-cell until it touched the crystal. The thermal e.m.f. was measured by means of a "Thermocouple Potentiometer,"

type P4, manufactured by the Croydon Precision Instrument Co., Ltd. The potentiometer gave consistent readings to 2 microvolts. The thermocouple was standardised by measuring, with respect to the ice point, the thermal e.m.f. at two temperatures, the solid CO_2 point and the liquid O_2 point. The deviation of the thermal e.m.f., when compared with the Adam's Scale,* was assumed to be of the form $\Delta E = aE + bE^2$, where E is the measured thermal e.m.f., a and b are the constants determined by standardisation.

III. 4. The three rotations with the crystal at -40° C. were carried out using the same crystal and the same technique as that described in Section III.2. The crystal was first aligned at room temperature using the arc set. In this connection it should be mentioned that the arcs were oriented so that the axis of rotation of one, arc (1), was parallel to the 0° - 180° line on the circular scale while that of the other arc, arc (2), was parallel to the 90° - 270° line. Let us consider the procedure for aligning the crystal for the X-rotation. The crystal was glued with its X-axis approximately parallel to the axis of rotation of the rotator-mount assembly and its Y-axis approximately parallel to the axis of arc (1). The Y-axis was then brought accurately perpendicular to Ho by rotating the rotator-mount assembly and noting the exact reading of the circular scale when the $\gamma_{S_1}^{M_{1,3}}$ and $\gamma_{S_1}^{M_{2,4}}$, $\gamma_{S_2}^{M_{1,3}}$ and $\gamma_{S_2}^{M_{2,4}}$ resonance lines crossed. With exactly the same reading on the circular scale, the axis of arc (2) was varied until X- and Z-axes were, respectively, exactly

---

*See "Temperature, Its Measurement and Control in Science and Industry." Edited by the American Institute of Physics, Table 1, p.210.

perpendicular and parallel to Ho. This occurred when the separation of the lines $\nu_{s_1}^{M}$ and $\nu_{s_2}^{M}$ was the same as that obtained with the orientation $\theta_y = 0$ and the mount described in the previous section. The procedure used in aligning the crystal for the Z-rotation was similar. The orientation of the crystal for the Y-rotation consisted simply of manipulating the two arcs until no splitting of either $\nu_{s_1}^{M}$ or $\nu_{s_2}^{M}$ line occurred at any crystal position.

The spectra were recorded at least 90 minutes after the cooling apparatus had been switched on. This procedure was necessary in order to allow the crystal to attain the temperature of the cold-cell. Owing to their very complicated rotation pattern the spectra obtained in the X- and Z-rotations were recorded at 5° intervals in the range 0° - 90° which was sufficient to establish the pattern. In its other respects the procedure used at -40° C. was similar to that used at room temperature.

The investigation of the n.m.r. spectra as a function of temperature was carried out with selected crystal orientations which gave measurable splitting of all the lines at -40° C. One crystal orientation would have been preferable because it would have eliminated the misalignment error. Since no single crystal position was found at which the separation of all the lines was measurable, the experiment had to be carried out with two crystal positions. They are defined in Section IV.6.

The influence of a static electric field upon the splitting of the lines was also investigated. An electric field of 2100 volts/cm. was applied to the crystal in the following manner. The cleavage faces, (010) and ($0\bar{1}0$), were painted with "aquadag," a suspension of

graphite in water, which served as electrodes. They were connected by means of small gauge copper wire to a 2100 volt power supply. After the field had been applied the crystal was cooled to -10° C. It was necessary to switch the field off while the spectrum was actually being recorded since the arrangement otherwise caused an enormous increase in the spectrometer noise. This procedure was repeated with the field direction reversed. No change in the spectrum was observed.

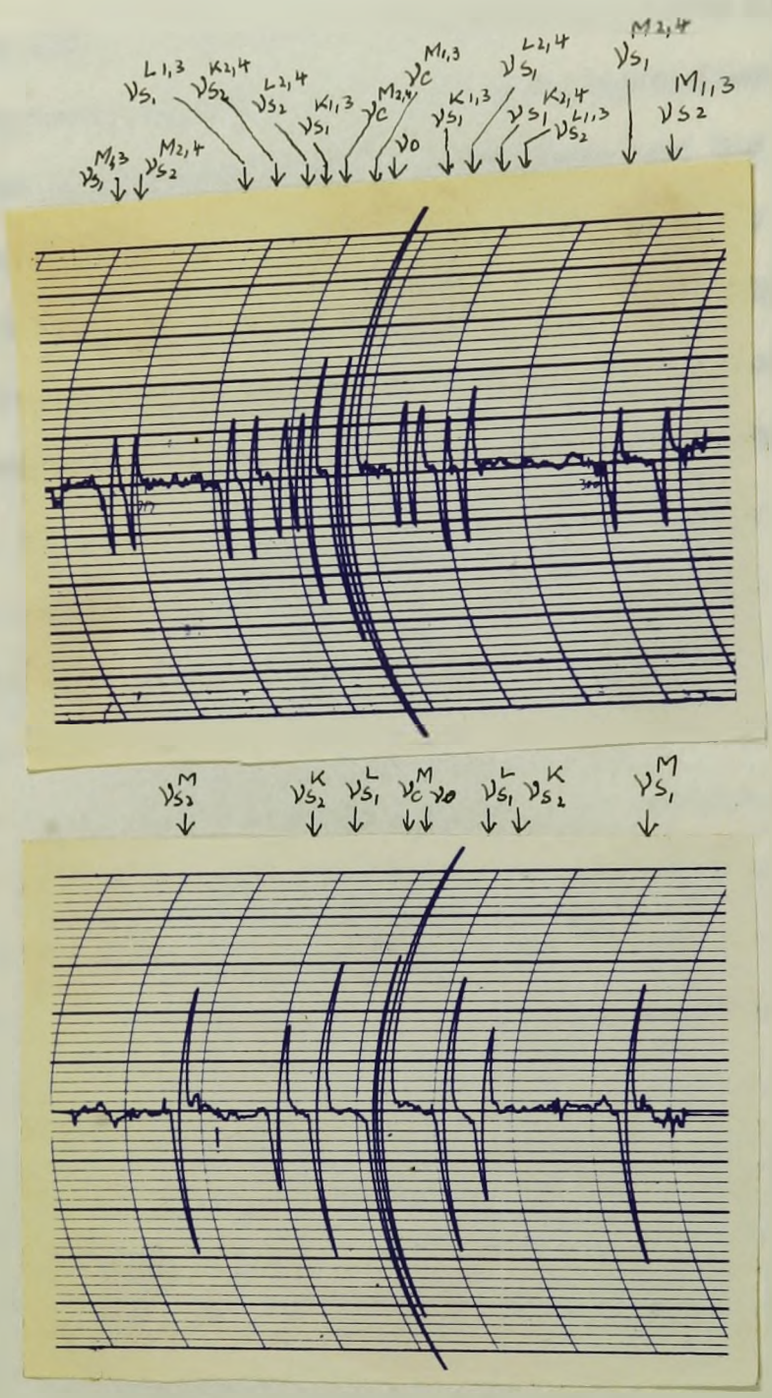

Fig. 5. Chart Recordings of the B^{11} N.M.R. Spectrum in Colemanite at Room Temperature Showing (a) the Observed Maximum Number of Lines, (b) the Observed Maximum Number of Lines in the Reduced Spectrum (for $\theta_y = 150^\circ$). The Orientation of the Crystal in the Case (a) is Explained in Table XI ($\alpha = 80^\circ$, $\beta = 45^\circ$).

CHAPTER IV

RESULTS

IV. 1. This chapter describes the complete analysis of the B^{11} nuclear magnetic resonance spectrum in colemanite at room temperature and at -40° C. It also includes the results of the investigation of a selected set of resonance lines over the temperature range 52° C. to -136° C.

The number of lines observed and the dependence of their frequencies on the orientation of the crystal with respect to the external magnetic field, Ho, at both temperatures, are explained by the discussions of Chapters I and II. It is assumed, in particular, that the boron nuclei occur at several sites per unit cell and that the resulting spectrum is a superposition of the simple 3-line spectra due to B^{11} nuclei at each type of site.

IV. 2. At room temperature, the observations consisted of recording the n.m.r. spectrum of B^{11} in colemanite over a wide frequency range as the crystal was rotated in turn about its X-axis ($\vec{b} \times \vec{c}$-crystallographic axis), Y-axis ($\vec{b}$-crystallographic axis), and Z-axis ($\vec{c}$-crystallographic axis). Two sample chart records are reproduced in Figs.5(a) and (b), where the frequency scale is roughly 107 kc./sec. per chart division. Fig.5(a) shows the maximum number of lines observed at room temperature, which is 15. The crystal orientation in this case is explained in Table XI. Fig.5(b) represents a reduced spectrum at the crystal orientation for which $\theta_y = 150^{\circ}$. The total number of lines in this case is only 8.

TABLE I

Experimentally Measured Values of the B^{11} Resonance Frequencies

in Mc./Sec. for the X-Rotation of Colemanite at Room Temperature

0°	15°	30°	45°	60°	75°	90°	105°	120°	135°	150°	165°
		10.748	10.819	11.138	11.586		11.586	11.134	10.824	10.752	
		11.773	11.459	11.389	11.591		11.592	11.390	11.461	11.776	10.950
	10.947	11.914	11.904	11.910	11.926		11.924	11.910	11.901	11.910	11.827
11.347	11.826	11.831	11.923	11.929	11.934		11.932	11.930	11.923	11.930	11.940
11.941	11.941	11.959	11.942	11.935	11.939	11.931	11.937	11.935	11.940	11.959	11.942
11.969	11.956	11.963	11.969	11.949	11.945	11.953	11.945	11.951	11.971	11.962	11.956
11.974	11.959	11.967	11.976	11.965	11.961	11.968	11.960	11.966	11.976	11.967	11.960
11.979	11.980	11.980	11.980	11.980	11.981	11.980	11.980	11.980	11.981	11.979	11.980
11.989	11.986	12.000	11.985	11.996	12.004	11.983	12.004	11.997	11.985	12.000	11.986
11.994	12.001	12.003	11.997	12.006	12.016	11.995	12.017	12.006	11.998	12.003	12.002
12.697	12.005	12.033	12.020	12.028	12.032	12.032	12.032	12.029	12.022	12.033	12.006
	12.024	12.053	12.040	12.035	12.037	12.056	12.037	12.035	12.039	12.055	12.027
	12.232	12.247	12.062	12.055	12.409		12.412	12.058	12.065	12.248	12.232
	13.056	13.222	12.517	12.577	12.466		12.467	12.576	12.516	13.219	13.052
			13.161	12.890				12.892	13.157		

TABLE II

Experimentally Measured Values of the B^{11} Resonance Frequencies in Kc./Sec. for the Y-Rotation of Colemanite at Room Temperature

0°	15°	30°	45°	60°	75°	90°	105°	120°	135°	150°	165°
		11.854	11.803	11.623						11.717	11.882
11.933	11.916	11.941	11.827	11.839	11.455	11.342	11.318	11.390	11.538	11.848	11.899
11.953	11.951	11.951	11.923	11.910	11.890	11.946	11.925	11.864	11.837	11.898	11.904
11.970	11.974	11.954	11.961	11.974	11.920	11.963	11.977	11.940	11.912	11.971	11.959
11.979	11.981	11.981	11.982	11.986	11.980	11.979	11.979	11.979	11.984	11.982	11.982
11.985	11.992	12.011	12.041	12.053	11.989	12.001	11.982	11.999	12.054	12.063	12.057
11.992	12.011	12.099	12.134	12.120	12.044	12.003	12.006	12.023	12.129	12.116	12.066
12.029	12.037	12.107	12.230	12.390	12.074	12.018	12.042	12.099	12.459	12.301	12.150
12.055	12.047				12.535	12.628	12.644	12.585			

TABLE III

Experimentally Measured Values of the β^{11} Resonance Frequencies in Kc./Sec. for the Z-Rotation of Colemanite at Room Temperature

0°	15°	30°	45°	60°	75°	90°	105°	120°	135°	150°	165°
			11.809								
	11.328	11.511	11.832		11.334		11.336		11.817	11.512	11.325
	11.550	11.843	11.833	11.507	11.544		11.544	11.511	11.833	11.845	11.546
	11.884	11.878	11.869	11.855	11.904	11.350	11.904	11.856	11.871	11.878	11.886
11.339	11.911	11.884	11.882	11.862	11.922	11.941	11.922	11.860	11.882	11.886	11.913
11.945	11.947	11.905	11.937	11.891	11.931	11.969	11.936	11.890	11.937	11.905	11.949
11.961	11.950	11.952	11.954	11.936	11.940	11.974	11.939	11.938	11.955	11.952	11.952
11.979	11.979	11.980	11.980	11.980	11.979	11.980	11.980	11.980	11.980	11.979	11.979
11.997	12.004	12.060	12.080	12.069	12.027	11.989	12.027	12.071	12.083	12.060	12.004
12.002	12.011	12.086	12.081	12.072	12.039	11.994	12.041	12.107	12.092	12.085	12.011
12.017	12.018	12.119	12.091	12.106	12.057	12.698	12.059	12.199	12.128	12.116	12.016
12.626	12.053	12.157	12.127	12.200	12.515		12.514	12.547	12.202	12.156	12.052
	12.078	12.486	12.202	12.552	12.711		12.707		12.246	12.486	12.075
	12.453		12.250								12.455
	12.635										12.637

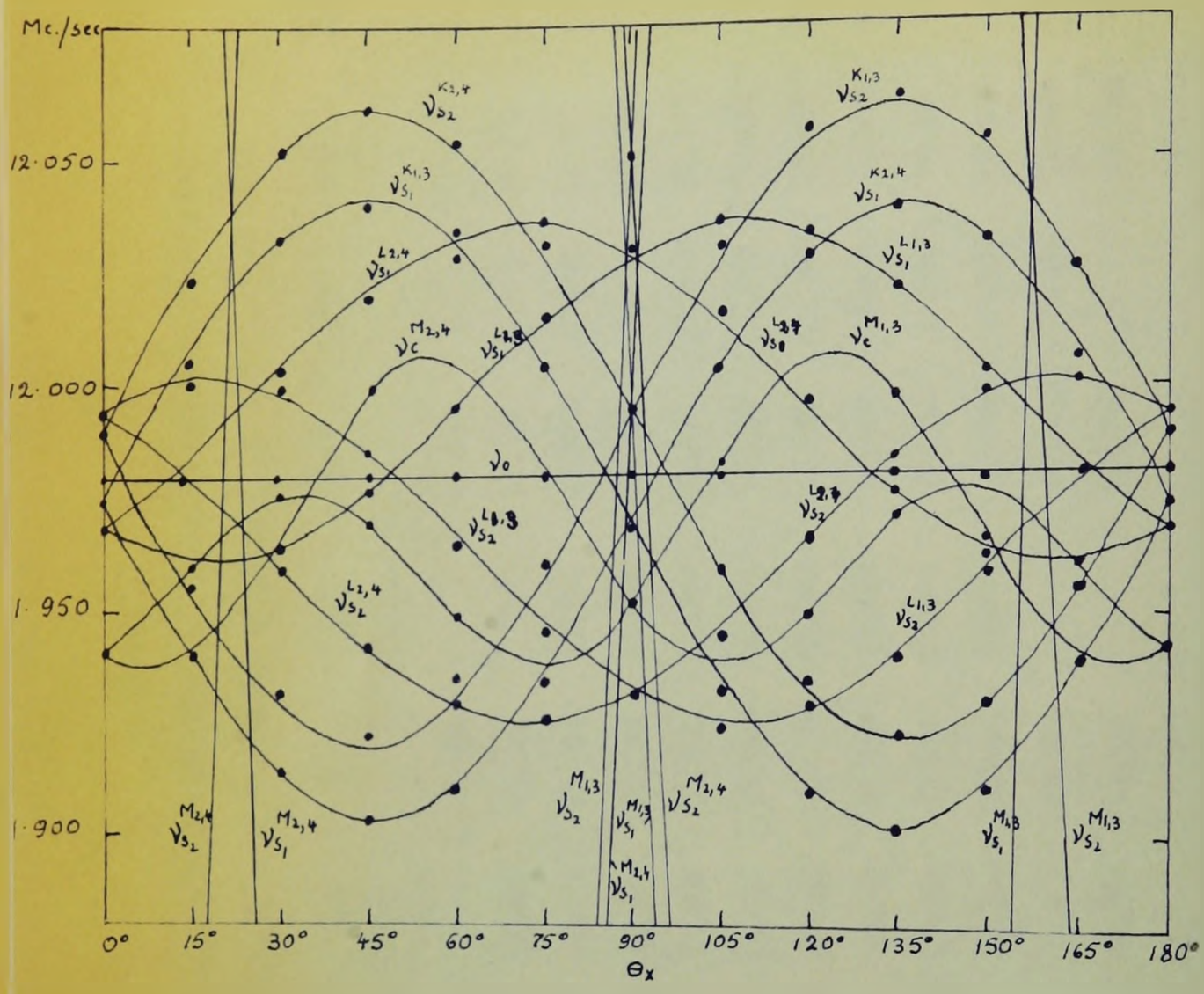

Fig. 6. The Rotation Pattern of all the B^{11} Lines in Colemanite at Room Temperature for the Rotation About the X-Axis.

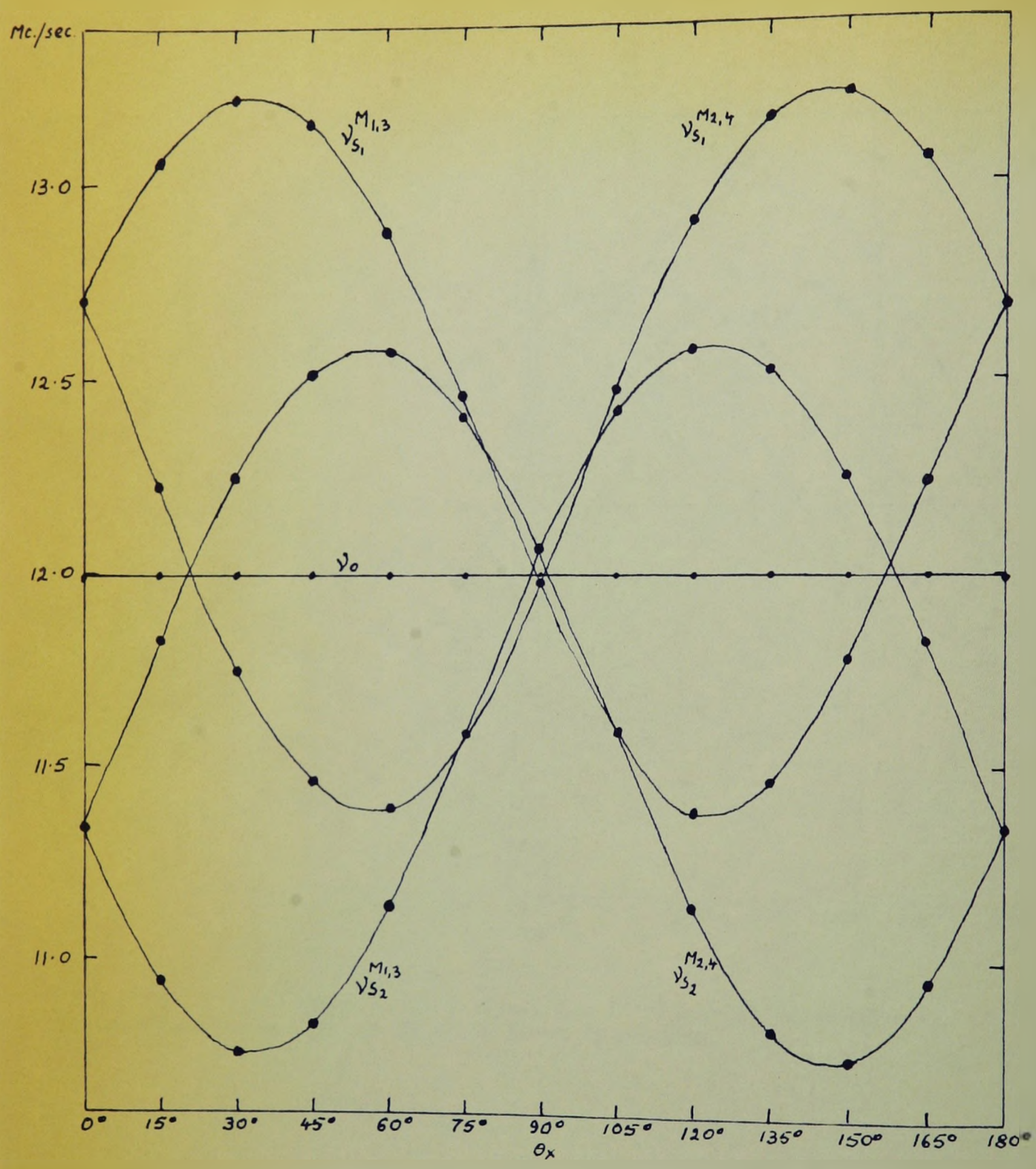

Fig. 7. The Rotation Pattern of the B^{11} Lines Depending Strongly Upon $2\theta x$ in Colemanite at Room Temperature.

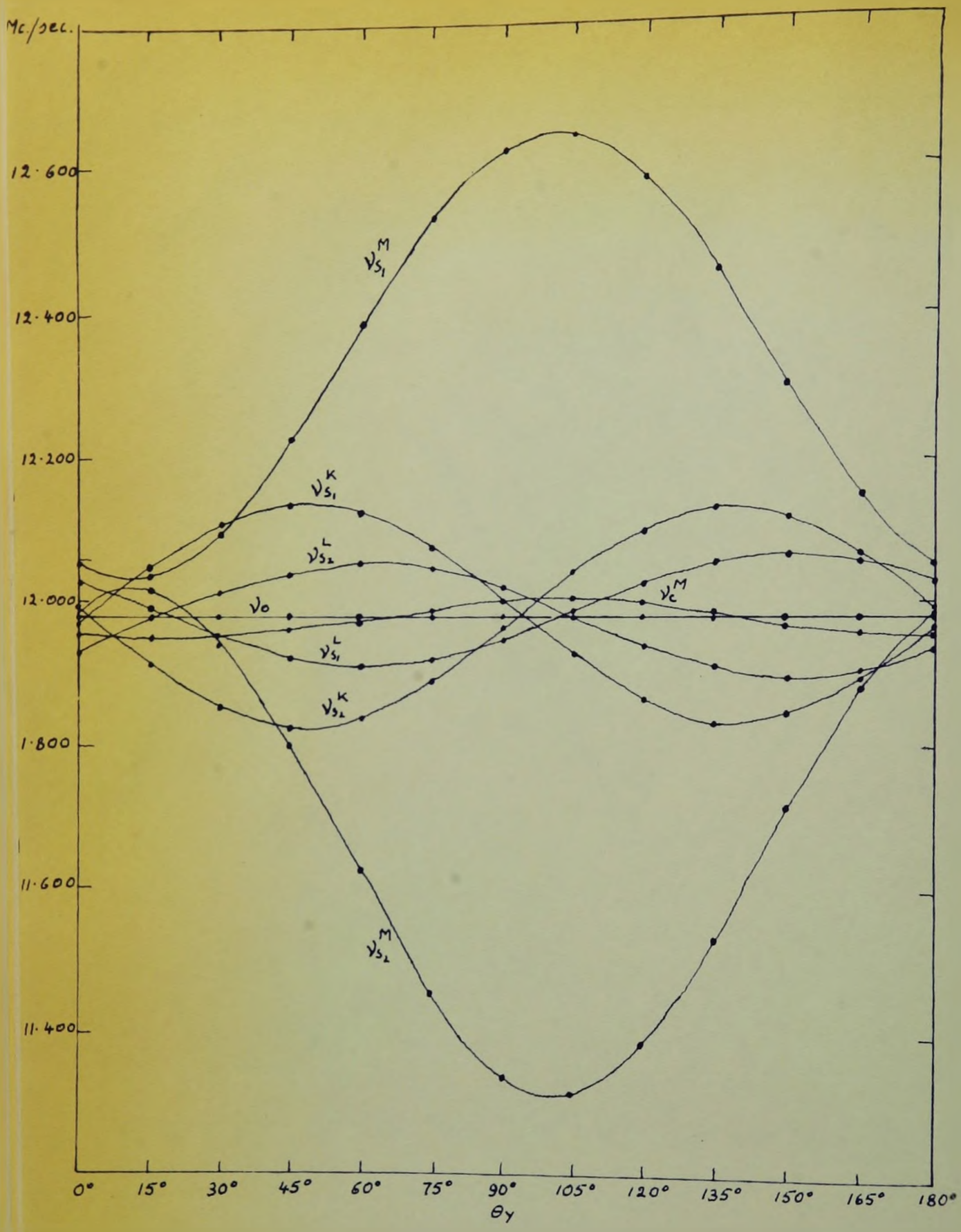

Fig. 8. The Rotation Pattern of all the B^{11} Lines in Colemanite at Room Temperature for the Rotation About the Y-Axis.

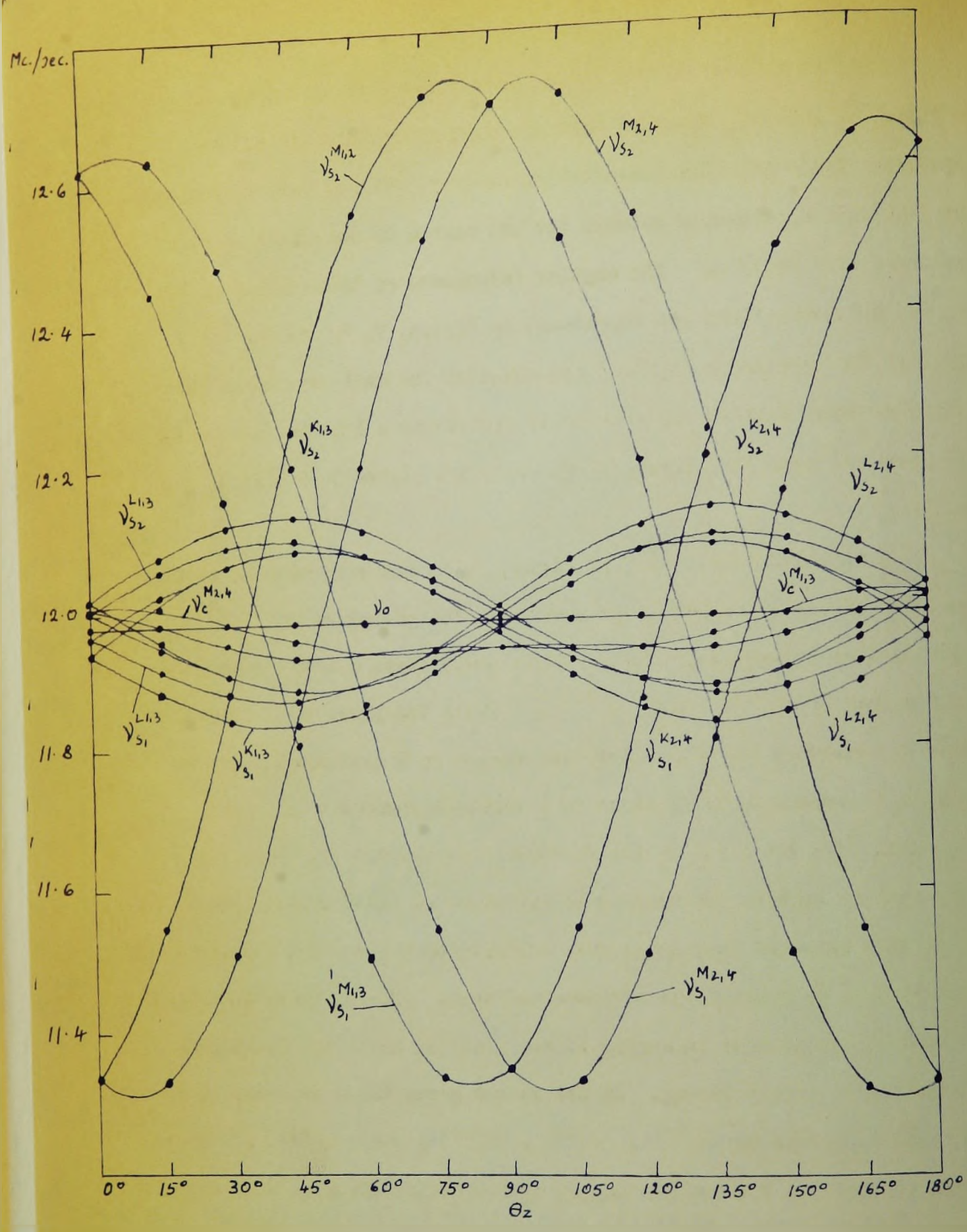

Fig. 9. The Rotation Pattern of all the B^{11} Lines in Colemanite at Room Temperature for the Rotation about the Z-Axis.

The frequencies of the lines, except the ones marked by ν_o in Figs.5(a) and (b), depended upon the angular orientation of the crystal. Their relative intensities, however, did not vary appreciably. The line widths, measured between the two maxima of each line, were of the order of 5 kc./sec. The angular dependence of these lines in the X-, Y-, and Z-rotations are reproduced in Figs.6, 7, 8, and 9. A chart of the type shown in Fig.5 was obtained for each crystal orientation on these figures and each point represents a line on the chart. The numerical data for Figs.6, 7, 8, and 9 are listed in Tables I, II, and III.

A detailed inspection of Figs.6, 7, 9, and 5(a) reveals that the lines can be conveniently grouped into four groups on the basis of their angular dependence. In the first group there are two resonance lines marked by $\nu_c^{M_{4,3}}$ and $\nu_c^{M_{3,4}}$. These two lines always remain close in frequency to ν_o. Their dependence on θ contains an appreciable 4θ component, in addition to a constant component and a 2θ component. On the basis of the discussion in Chapter II, these two lines must be central frequencies belonging to at least two different sites in the unit cell and they arise from transitions between the energy levels which contain an appreciable second-order term. Hence, these two lines are central frequencies belonging to two sites at which the quadrupole interaction is fairly strong. In the second group there are four lines (two pairs), marked by $\nu_{s_1}^{M_{4,3}}$, $\nu_{s_2}^{M_{4,3}}$, $\nu_{s_1}^{M_{3,4}}$, and $\nu_{s_2}^{M_{3,4}}$. They depend strongly on 2θ and are <u>nearly</u> symmetrically situated with respect to ν_o. Hence, they are satellite frequencies belonging to at least

two sites and they arise from transitions between energy levels which are strongly perturbed by the quadrupole interaction. In the third group there are eight lines (four pairs), marked by $\nu_{S_1}^{L_{1,3}}$, $\nu_{S_2}^{L_{1,3}}$, $\nu_{S_1}^{L_{2,4}}$, $\nu_{S_2}^{L_{2,4}}$, $\nu_{S_1}^{K_{1,3}}$, $\nu_{S_2}^{K_{1,3}}$, $\nu_{S_1}^{K_{2,4}}$ and $\nu_{S_2}^{K_{2,4}}$, which depend almost entirely on 2 θ and are symmetrically located about ν_o. We can say that they are satellite frequencies belonging to at least four sites which arise from transitions between the energy levels which are weakly perturbed by the quadrupole interaction. Lastly, there is one line, marked by ν_o, which stands out by its lack of angular dependence and its great intensity. In order to assign this line to a particular transition, or transitions, it should be noted that the central frequencies for the four sites at which the quadrupole interactions are weak have not been accounted for yet. These transitions should all occur at frequencies almost exactly equal to ν_o, the unperturbed frequency, because the expressions for their respective energy levels are expected to contain negligible second-order terms. The line marked ν_o, satisfies these conditions, hence, it is a composite line consisting of four separate, but unresolved, signals. Summarising, the first two groups of six lines in all must belong to the same two sites, while the next two groups of twelve lines in all, the third and fourth, must belong to additional four sites. Hence, the n.m.r. spectrum of B^{11} in colemanite at room temperature contains 18 separate signals, not all of which can be resolved, and it arises from six non-identical B^{11} sites whose $\nabla\tilde{E}$'s differ in some respects.

Our next aim is to establish the point group of colemanite at room temperature. On the basis of chemical data and the unit cell

dimensions, the formula for colemanite is $4CaO \cdot 6B_2O_3 \cdot 10H_2O$. Hence, the unit cell of colemanite contains 12 boron sites. It will be recalled from Section II.2 that the $\tilde{\nabla}E$'s at two sites related by a centre of symmetry are identical from the point of view of the theory dealt with in Chapter II. Hence, colemanite must have a centrosymmetric structure since of the 12 borons present in the unit cell we have found that only 6 have non-identical $\tilde{\nabla}E$'s. Let us now refer to Figs.6, 7, and 9. It can be seen that the rotation pattern is symmetrical with respect to $\theta = 0^\circ$ and $\theta = 90^\circ$ in the X- and Z-rotations, and that the reduced spectra occur at the following positions: $\theta_x = 0^\circ$ and $\theta_z = 90^\circ$ (Y parallel to Ho), $\theta_x = 90^\circ$ and $\theta_z = 0^\circ$ (Y perpendicular to Ho). Furthermore, a reduced spectrum results for the complete Y-rotation. The Y-axis must therefore be parallel to a two-fold rotation axis or to normal to a mirror plane or to both. However, the combinations,

mirror plane plus centre of symmetry

two-fold rotation axis plus centre of symmetry

mirror plane plus two-fold rotation axis

are identical, all three being denoted by the point group symbol 2/m. Actually, anticipating our low-temperature results, the presence of 12 boron sites in the unit cell of colemanite, and hence of the centre of symmetry at room temperature, will be established by the analysis of n.m.r. spectra alone. We shall return to this point later.

The B^{11} sites were classified on the basis that colemanite at room temperature possesses point group 2/m. The three non-equivalent groups of sites were named by capital letters K, L, and M. Each group

TABLE IV

The Separations, in Kc./Sec., of the B^{11} Satellite Lines Belonging to the K Sites in Colemanite at Room Temperature. The Signs Are Relative.

Rotation	θ°	0	15	30	45	60	75	90	105	120	135	150	165
X	$K_{1,3}$	15	-49	-102	-117	-93	-43	27	100	148	164	145	87
	$K_{2,4}$	15	83	139	158	145	98	27	-44	-94	-116	-103	-50
Y	K	22	-131	-253	-307	-281	-184	-38	117	235	292	268	167
Z	$K_{1,3}$	-36	-142	-208	-222	-181	-96	15	119	181	201	155	67
	$K_{2,4}$	-36	71	155	198	181	117	15	-91	-181	-221	-207	-139

TABLE V

The Separations, in Kc./Sec., of the B^{11} Satellite Lines Belonging to the L Sites in Colemanite at Room Temperature. The Signs Are Relative.

Rotation	θ^{o}	0	15	30	45	60	75	90	105	120	135	150	165
X	$L_{1,3}$	25	-6	-44	-78	-106	-111	-101	-72	-31	9	38	42
	$L_{2,4}$	25	42	37	9	-31	-71	-101	-113	-105	-82	-44	-6
Y	L	-96	-18	57	118	143	124	72	-5	-83	-142	-165	-153
Z	$L_{1,3}$	72	-61	-155	-199	-178	-96	25	155	251	295	271	189
	$L_{2,4}$	72	194	276	294	251	153	25	-91	-181	-201	-155	-59

TABLE VI

The Separations, in Kc./Sec., of the B^{11} Satellite Lines Belonging to the M Sites in Colemanite at Room Temperature. The Signs Are Relative.

Rotation	θ^{o}	0	15	30	45	60	75	90	105	120	135	150	165
X	$M_{1,3}$	1350	2109	2474	2342	1752	880	-73	-820	-1186	-1055	-472	405
	$M_{2,4}$	1350	406	-474	-1058	-1188	-818	-73	881	1758	2333	2467	2102
Y	$M_{1,3}$	-70	-26	-158	-427	-767	-1080	-1286	-1326	-1195	-921	-584	-268
Z	$M_{1,3}$	-1287	-1307	-975	-370	338	971	1348	1371	1036	429	-270	-909
	$M_{2,4}$	-1287	-903	-273	441	1045	1377	1348	970	339	-369	-974	-1312

TABLE VII

The Separations, in Kc./Sec., of the B^{11} Central Line from the Unperturbed Frequency, ν_0 = 11.981, Mc./Sec., for the M Sites in Colemanite at Room Temperature

Rotation	θ°	0	15	30	45	60	75	90	105	120	135	150	165
X	$M_{1,3}$	-40	-22	-4	-12	-32	-42	-28	4	25	17	-14	-39
	$M_{2,4}$	-40	-40	-14	16	25	4	-28	-44	-30	-10	-4	-21
Y	M_1	-28	-30	-30	-20	-7	8	22	25	18	4	-10	-22
Z	$M_{1,3}$	21	23	2	-27	-45	-41	-40	-42	-43	-44	-29	-1
	$M_{2,4}$	21	-1	-29	-44	-45	-41	-40	-45	-43	-26	2	23

TABLE VIII

The Separations, Kc./Sec., of the B^{11} Centre of Gravity of the Satellite Lines from the Unperturbed Frequency, ν_0 = 11.981 Mc./Sec., for the M Sites in Colemanite at Room Temperature

Rotation		θ°	0	15	30	45	60	75	90	105	120	135	150	165
X		$M_{1,3}$	42	22	5	10	34	46	40	22	3	9	32	50
		$M_{2,4}$	42	49	30	8	3	20	40	47	33	11	6	21
Y		M	40	44	40	37	27	15	5	1	8	19	29	36
Z		$M_{1,3}$	2	1	18	36	50	49	43	41	48	51	40	20
		$M_{2,4}$	2	21	40	49	49	25	43	48	49	37	18	0

of these sites consists of four symmetry-equivalent sites which were denoted by the subscripts 1, 2, 3, and 4, as shown in Fig.1. Thus K_1 and K_2 are related by the two-fold symmetry axis and so are K_3 and K_4. Since K_1 and K_3 (or K_2 and K_4) are related by the centre of symmetry, $\nabla\widetilde{E}$ at these sites are identical; hence, at room temperature, these two sites are simply denoted by $K_{1,3}$ (or $K_{2,4}$). The L and M sites are similarly denoted. The three lines arising from the transitions $m = \mp 3/2 \leftrightarrow \mp 1/2$ and $m = \mp 1/2 \leftrightarrow \mp 1/2$ were denoted by (ν_{s_1} , ν_{s_2}) and ν_c , respectively; the subscripts s_1 and s_2 were chosen so that $\Delta\nu = \nu_{s_2} - \nu_{s_1}$ was positive. The site of their origin was indicated by a superscript, thus $\nu_{s_1}^{M_{1,3}}$, $\nu_{s_2}^{M_{1,3}}$, $\nu_c^{M_{1,3}}$. Each line occurring in the reduced spectrum should be denoted by the superscript $P_{1,2,3,4}$ (P = K, L, M) but, for brevity, it was denoted simply by the superscript P. The group of lines ν_c^{K} , ν_c^{L} in the Y-rotation and $\nu_c^{K_{1,3}}$, $\nu_c^{K_{2,4}}$, $\nu_c^{L_{1,3}}$, $\nu_c^{L_{2,4}}$ in the X- and Z-rotation and in Fig.5(a) were denoted simply by ν_o , since their frequencies were very close to $\nu_o = (H/\mu)/(Ih)$.

IV. 3. For the quantitative analysis of the angular dependence of the frequencies, the separations of the satellite frequencies ν_{s_1} and ν_{s_2} have been deduced from the Tables I - III for each site, and are listed in Tables IV - VI. The relative signs have been chosen so that b of Eq.(27) is positive. The experimental values of $\nu_c^{M_{i,j}} - \nu_o$ and $(\nu_{s_1}^{M_{i,j}} + \nu_{s_2}^{M_{i,j}})/2 - \nu_o$, also deduced from Tables I - III, are listed in Tables VII - VIII, respectively. The corresponding experimental values for the sites K and L have not been considered since they are negligibly small.

TABLE IX

Experimental Fourier Coefficients, in Kc./Sec., for B^{11} Sites M in Colemanite at Room Temperature

Rotation	Site	a	b	c		
X	$M_{1,3}$	642.17	711.03	1699.08		
	$M_{2,4}$	640.50	708.00	-1697.77		
Y	$M_{1,2,3,4}$	-675.67	609.17	246.27		
Z	$M_{1,3}$	31.25	-1315.30	-402.17		
	$M_{2,4}$	33.50	-1316.87	406.07		
		n	p	u	r	v
X	$M_{1,3}$	-15.583	-6.230	-18.333	-14.033	18.767
	$M_{2,4}$	-15.500	-6.117	-18.833	13.250	-19.033
Y	$M_{1,2,3,4}$	-5.830	-24.870	2.500	12.750	-2.020
Z	$M_{1,3}$	-22.167	30.400	13.167	9.100	8.083
	$M_{2,4}$	-22.333	30.667	12.750	-9.433	-8.217
		$\bar{n}$	$\bar{p}$	$\bar{u}$	$\bar{r}$	$\bar{v}$
X	$M_{1,3}$	26.250	0.917	16.000	0.417	-15.867
	$M_{2,4}$	25.833	0.767	15.917	-1.283	15.733
Y	$M_{1,2,3,4}$	25.083	17.900	-2.500	9.167	-1.883
Z	$M_{1,3}$	33.250	-20.133	-10.750	-6.300	-7.367
	$M_{2,4}$	33.417	-20.567	-10.333	6.683	6.650

TABLE X

Experimental Fourier Coefficients in Kc./Sec., of the B^{11} Satellite Lines for the K and L sites in Colemanite at Room Temperature

Rotation	Site	a	b	c
X	$K_{1,3}$	23.50	-5.75	-140.6
	$K_{2,4}$	21.52	-6.28	138.08
Y	$K_{1,2,3,4}$	-7.75	29.95	-299.33
Z	$K_{1,3}$	-11.80	-26.98	-210.48
	$K_{2,4}$	-11.50	-26.40	209.17
X	$L_{1,3}$	-36.25	63.53	-44.42
	$L_{2,4}$	-36.67	63.50	45.00
Y	$L_{1,2,3,4}$	-12.33	-83.85	130.00
Z	$L_{1,3}$	48.53	22.66	-247.48
	$L_{2,4}$	48.17	22.62	248.48

TABLE XI

A Comparison of the Values of $\Delta\nu$ Predicted for Specified Crystal Orientations Assuming Possible Sign Combinations of C_z and C_x, with the Experimentally Measured Values of $\Delta\nu$.

α°	β°	Site	Sign Combination	$\Delta\nu$ kc./sec.	Sign Combination	$\Delta\nu$ kc/sec	Experimental $\Delta\nu$ Kc/sec
50	165	$K_{1,3}$ $K_{2,4}$	$= \; \pm$	-321	$\mp \; \pm$	-409	326
			$\pm \; \pm$	-249	$\pm \; \pm$	-161	242
		$L_{1,3}$ $L_{2,4}$	$= \; \pm$	42	$\pm \; \mp$	232	31
			$\pm \; \pm$	204	$\mp \; \mp$	14	206
		$M_{1,3}$ $M_{2,4}$	$= \; \pm$	-1116	$\pm \; =$	-808	1130
				286		-22	341
50	195	$K_{1,3}$ $K_{2,4}$	$= \; \pm$	-249	$\mp \; \pm$	-161	254
			$\pm \; \pm$	-321	$\pm \; \mp$	-409	322
		$L_{1,3}$ $L_{2,4}$	$= \; \pm$	204	$\pm \; \mp$	14	195
			$\pm \; \pm$	42	$\mp \; \mp$	232	39
		$M_{1,3}$ $M_{2,4}$	$\mp \; \pm$	286	$\pm \; =$	-22	282
				-1116		-808	1086
80	45	$K_{1,3}$ $K_{2,4}$	$= \; \pm$	121	$\mp \; \pm$	169	125
			$\pm \; \pm$	-245	$\pm \; \mp$	-293	240
		$L_{1,3}$ $L_{2,4}$	$= \; \pm$	305	$\pm \; \mp$	-183	305
			$\pm \; \pm$	-167	$\mp \; \pm$	321	170
		$M_{1,3}$ $M_{2,4}$	$\mp \; \pm$	792	$\pm \; =$	6	749
				-596		190	675

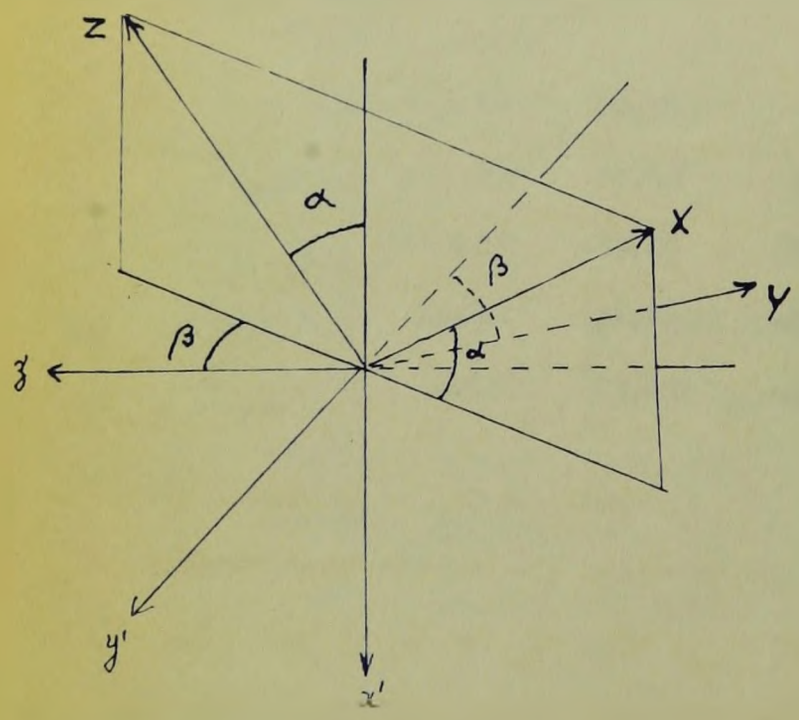

In order to determine the coefficients occurring in Eqs.(18), (20), and (22), a harmonic analysis of the experimental results listed in Tables IV - VIII has been carried out using the method of 12-point analysis by Whittaker and Robinson (43). The values of these coefficients for site M are listed in Table IX; those for sites K and L are listed in Table X.

The problem of determining the relative signs of the off-diagonal components of two $\tilde{\nabla}$E's, related by a two-fold symmetry axis, was discussed at length in Section II.5. The sites $M_{1,3}$ and $M_{2,4}$ can be dealt with in a straightforward way since they possess an appreciable second-order term. Accordingly, the inspection of the sign in front of $\bar{r}_i$ in Table IX, reveals that, for $M_{1,3}$, $\bar{r}_x$ is positive, $\bar{r}_y$ is positive, $\bar{r}_z$ is negative; for $M_{2,4}$, $\bar{r}_x$ is negative, $\bar{r}_y$ is positive, and $\bar{r}_z$ is positive. It follows from Eqs.(21) that the signs of C_i are: $+C_x$, $+C_y$, $-C_z$ for $M_{1,3}$, and $-C_x$, $+C_y$, and $+C_z$ for $M_{2,4}$. The off-diagonal tensor components follow from these values, using Eqs.(19). The remaining two non-equivalent sites, K and L, have to be dealt with by the alternative method described in Chapter II. Table XI lists the values of $\Delta\nu$ calculated by means of Eqs.(36), using the two possible combinations of signs of C_x and C_y. The experimental values of $\Delta\nu$ are listed in the last column. As can be seen, the following combination of signs predicts the experimental results: $-C_x$, $-C_z$ for $K_{1,3}$; $+C_x$, $+C_z$ for $K_{2,4}$; $-C_x$, $-C_z$ for $L_{1,3}$; and $+C_x$, $+C_z$ for $L_{2,4}$. Table XI also lists the $M_{1,2}$ and $M_{2,4}$ sites. The agreement between the theoretically predicted and the experimental values of $\Delta\nu$ is poor for

TABLE XII

Experimental Values of the Tensor Components Ψ_{ii}, in Kc./Sec., for all B^{11} Sites in Colemanite at Room Temperature.

Site	Rotation	Ψ_{xx}	Ψ_{yy}	Ψ_{zz}	Ψ_{xy}	Ψ_{yz}	Ψ_{zx}
$K_{1,3}$	X	-47.00	17.75	29.25		140.60	
	Y	-37.70	15.50	22.20			299.33
	Z	-39.32	14.82	24.50	210.48		
Average		-38.51	15.16	23.35			
$K_{2,4}$	X	-43.04	15.24	27.80		-138.08	
	Y	-37.70	15.50	22.20			299.33
	Z	-37.90	14.90	23.00	-209.17		
Average		-37.80	15.20	22.63			
$L_{1,3}$	X	72.50	27.28	-99.78		44.42	
	Y	71.52	24.66	-96.18			-130.00
	Z	68.80	26.04	-94.84	247.48		
Average		70.16	25.35	-95.51			
$L_{2,4}$	X	73.34	26.83	-100.17		-45.00	
	Y	71.52	24.66	-96.18			-130.00
	Z	70.79	25.55	-96.34	-248.48		
Average		71.16	25.11	-96.26			
$M_{1,3}$	X	-1284.34	1353.20	-68.86		-1699.08	
	Y	-1284.84	1351.34	-66.50			-246.27
	Z	-1284.05	1346.55	-62.50	402.17		
Average		-1284.41	1350.36	-65.95			
$M_{2,4}$	X	-1281.00	1349.15	-68.15		1697.77	
	Y	-1284.84	1351.34	-66.50			-246.27
	Z	-1283.37	1350.37	-67.00	-406.07		
Average		-1283.07	1350.29	-67.22			

M sites because the M sites reflect a misalignment error much more strongly than the K and L sites. However, the agreement for K and L sites is very good.

Using the values of a_i, b_i, and c_i listed in Tables IX and X, and Eqs.(19), the tensor components ψ_{ij} may now be calculated. They are listed in Table XII. The values of ψ_{ii} deduced from a_x and b_x for the K and L sites, though, have not been used in the averaging process because these coefficients carry a large experimental error. This error arises chiefly from very small separations between the satellite lines in the X-rotation, as compared with the other two rotations. The average values listed in Table XII for each nuclear site have been used in diagonalisation calculations, using Eqs.(25)-(29). The resulting values of the coupling constants and the asymmetry parameters are listed in the first and the third columns, respectively, in Table XXV. The estimated experimental error is included. The direction cosines of the principal axes (x, y, z) of ∇E, with respect to (X, Y, Z) axes, have been calculated with the aid of Eqs.(32) and (33), and are listed in Table XXVI for all the sites. The signs are relative.

IV. 4. At -40° C., as at room temperature, the observation of the spectrum consisted of recording the n.m.r. spectrum of B^{11} over a wide frequency range as the crystal of colemanite was rotated in turn about the three axes (X, Y, Z) defined in Section III.2. Two sample chart recordings are reproduced in Figs.10(a) and (b), with the frequency scales roughly 71 kc./sec. per chart division and 138 kc./sec. per chart division, respectively. The spectrum in Fig.10(a) corresponds

TABLE XIII

Experimentally Measured Values of the B^{11} Resonance Frequencies in Mc./Sec. for the X-Rotation of Colemanite at -40° C.

0°	15°	30°	45°	60°	75°	90°	105°	120°	135°	150°	165°
			7.814								
	7.953		7.848						7.815		7.957
	7.967	7.747	8.435	8.139				8.138	7.849	7.744	7.970
8.346	8.813	7.763	8.497	8.174	8.581		8.585	8.173	8.436	7.760	8.817
8.383	8.866	8.764	8.896	8.366	8.597		8.601	8.365	8.494	8.757	8.872
8.931	8.933	8.825	8.914	8.420	8.607	8.929	8.615	8.409	8.898	8.818	8.934
8.933	8.946	8.908	8.937	8.906	8.629	8.934	8.632	8.904	8.915	8.906	8.951
8.966	8.958	8.926	8.942	8.919	8.924	8.935	8.926	8.916	8.936	8.926	8.959
8.974	8.962	8.943	8.961	8.924	8.929	8.943	8.931	8.937	8.969	8.955	8.965
8.975	8.968	8.954	8.972	8.943	8.933	8.951	8.936	8.950	8.978	8.963	8.972
8.978	8.974	8.967	8.979	8.955	8.951	8.964	8.951	8.968	8.981	8.968	8.978
8.982	8.978	8.973	8.981	8.972	8.973	8.979	8.973	8.984	8.983	8.983	8.983
8.984	8.984	8.984	8.984	8.983	8.982	8.983	8.984	9.000	8.985	8.994	8.988
8.987	8.990	8.995	8.988	8.999	8.990	8.984	8.992	9.017	8.988	8.999	8.994
8.990	8.995	8.999	8.990	9.016	9.015	8.995	9.019	9.028	9.007	9.018	9.000
8.991	8.999	9.017	9.008	9.027	9.037	9.007	9.036	9.045	9.013	9.028	9.005
8.994	9.006	9.028	9.014	9.044	9.043	9.010	9.041	9.054	9.033	9.043	9.012
9.001	9.013	9.042	9.030	9.054	9.414	9.033	9.410	9.061	9.056	9.066	9.031
9.002	9.033	9.063	9.036	9.066	9.439	9.039	9.434	9.556	9.074	9.231	9.227
9.703	9.233	9.227	9.056	9.558	9.473	9.079	9.465	9.601	9.495	9.293	9.268
9.733	9.281	9.288	9.078	9.602	9.494	9.084	9.487	9.881	9.552	10.218	9.074
	10.066	10.218	9.484	9.883				9.917	10.152	10.236	
		10.234	9.549	9.920					10.180		
			10.152								
			10.181								

TABLE XIV

Experimentally Measured Values of the B^{11} Resonance Frequencies in Mc./Sec. for the Y-Rotation of Colemanite at -40° C.

0°	15°	30°	45°	60°	75°	90°	105°	120°	135°	150°	165°
										8.711	8.880
8.937	8.917		8.818	8.635		8.335		8.375	8.524	8.738	8.890
8.941	8.931	8.851	8.827	8.640	8.455	8.359	8.305	8.410	8.556	8.843	8.896
8.944	8.942	8.864	8.832	8.839	8.471	8.943	8.340	8.864	8.830	8.850	8.902
8.951	8.948	8.947	8.925	8.843	8.891	8.958	8.926	8.869	8.836	8.894	8.904
8.966	8.972	8.957	8.935	8.921	8.896	8.961	8.932	8.937	8.907	8.909	8.911
8.975	8.977	8.963	8.959	8.978	8.924	8.967	8.974	8.962	8.932	8.971	8.960
8.982	8.981	8.986	8.985	8.981	8.983	8.982	8.983	8.984	8.987	8.984	8.986
8.991	8.986	9.006	9.037	9.054	8.993	9.002	8.997	9.009	9.041	9.057	9.053
9.009	9.000	9.020	9.046	9.126	9.046	9.009	9.014	9.039	9.066	9.074	9.058
9.031	9.022	9.104	9.135	9.130	9.078	9.013	9.044	9.104	9.131	9.120	9.064
9.036	9.032	9.115	9.142	9.400	9.083	9.027	9.050	9.110	9.137	9.128	9.076
9.072	9.041	9.122	9.235	9.409	9.534	9.618	9.633	9.575	9.460	9.310	9.172
9.079	9.054		9.247		9.551	9.644	9.663	9.606	9.485	9.327	9.179
	9.061										

TABLE XV

Experimentally Measured Values of the B^{11} Resonance Frequencies in Mc./Sec. for the Z-Rotation of Colemanite at -40° C.

0°	15°	30°	45°	60°	75°	90°	105°	120°	135°	150°	165°
		8.513									
		8.547	8.813						8.813		
		8.833	8.824						8.828	8.511	
	8.319	8.866	8.849	8.516			8.334	8.512	8.856	8.547	8.321
	8.354	8.882	8.853	8.550	8.334		8.378	8.554	8.857	8.833	8.354
	8.554	8.884	8.860	8.835	8.382		8.547	8.836	8.858	8.862	8.552
8.329	8.559	8.885	8.873	8.873	8.552	8.345	8.568	8.868	8.872	8.881	8.559
8.355	8.885	8.887	8.876	8.874	8.569	8.383	8.893	8.872	8.875	8.882	8.885
8.941	8.894	8.899	8.882	8.882	8.893	8.934	8.923	8.882	8.878	8.896	8.891
8.960	8.916	8.913	8.894	8.892	8.922	8.966	8.929	8.894	8.893	8.897	8.918
8.963	8.941	8.935	8.911	8.897	8.928	8.975	8.932	8.898	8.909	8.909	8.943
8.970	8.952	8.951	8.929	8.912	8.934	8.978	8.939	8.911	8.927	8.934	8.952
8.971	8.973	8.954	8.952	8.927	8.945	8.982	8.942	8.928	8.951	8.948	8.977
8.980	8.983	8.984	8.985	8.985	8.984	8.984	8.984	8.985	8.984	8.985	8.984
9.005	8.995	9.037	9.058	9.056	9.025	8.987	9.026	9.055	9.060	9.038	8.996
9.006	9.013	9.062	9.080	9.073	9.033	8.990	9.032	9.068	9.078	9.061	9.013
9.014	9.016	9.075	9.087	9.079	9.045	8.991	9.035	9.074	9.089	9.074	9.020
9.015	9.032	9.086	9.092	9.085	9.050	8.994	9.046	9.085	9.094	9.086	9.031
9.025	9.052	9.092	9.108	9.097	9.079	8.995	9.050	9.094	9.105	9.093	9.054
9.619	9.074	9.104	9.114	9.134	9.532	9.001	9.079	9.132	9.113	9.104	9.075
9.647	9.084	9.138	9.155	9.233	9.544	9.002	9.543	9.237	9.155	9.139	9.085
	9.462	9.183	9.198	9.544	9.706	9.706	9.550	9.547	9.195	9.181	9.463
	9.475	9.471	9.220	9.579	9.743	9.732	9.707	9.581	9.220	9.188	9.475
	9.621	9.504	9.250				9.745		9.248	9.470	9.621
	9.658		9.279						9.275	9.503	9.656

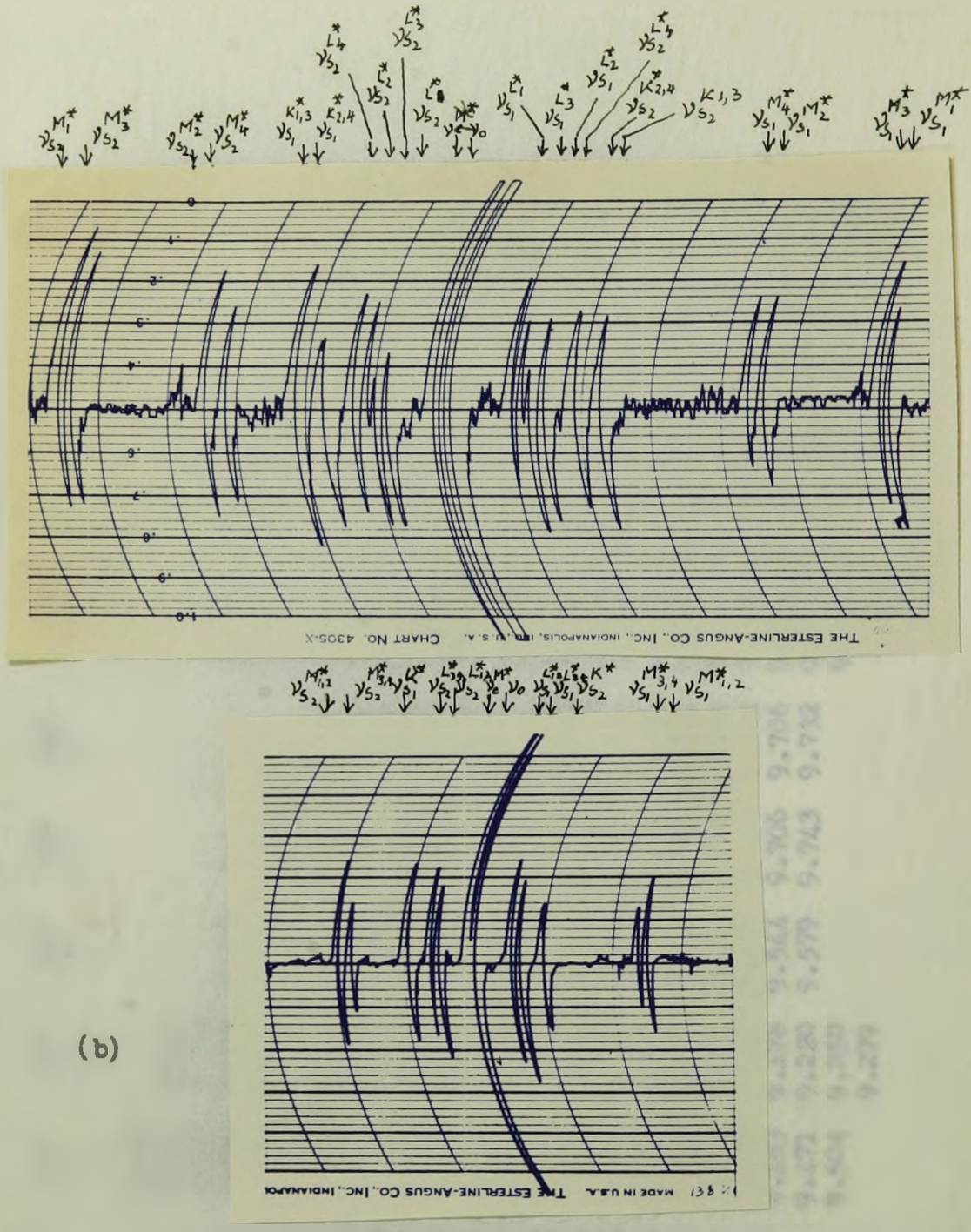

Fig. 10. Chart Recordings of the B^{11} N. M. R. Spectrum in Colemanite at -40° C. Showing (a) the Typical Spectrum, (b) the Typical Reduced Spectrum (for $\theta_y = 150°$). The Orientation of the Crystal in the Case (a) is Explained in Table XX.

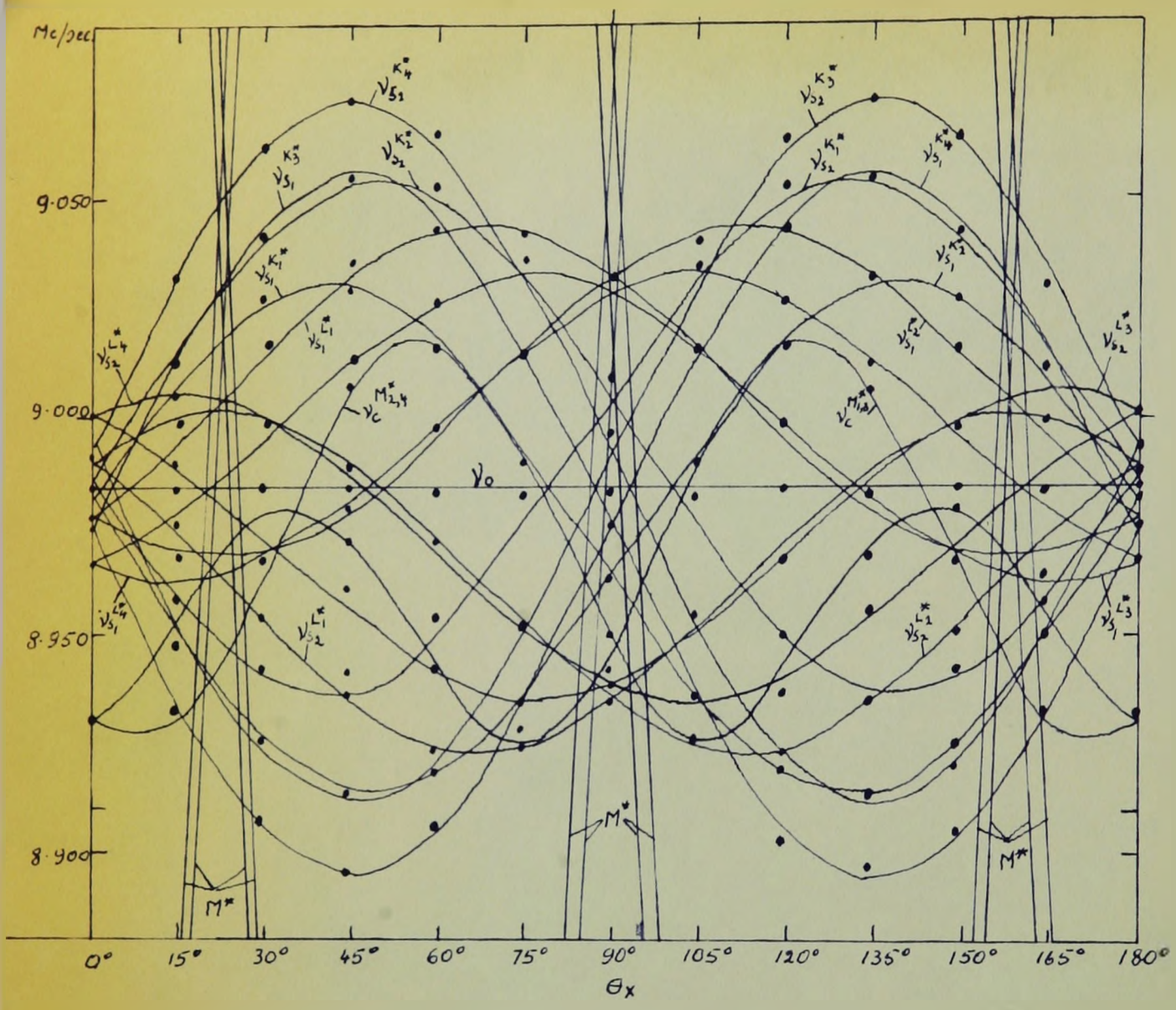

Fig. 11. The Rotation Pattern of all the B^{11} Lines in Colemanite at -40° C. for the Rotation About the X-Axis.

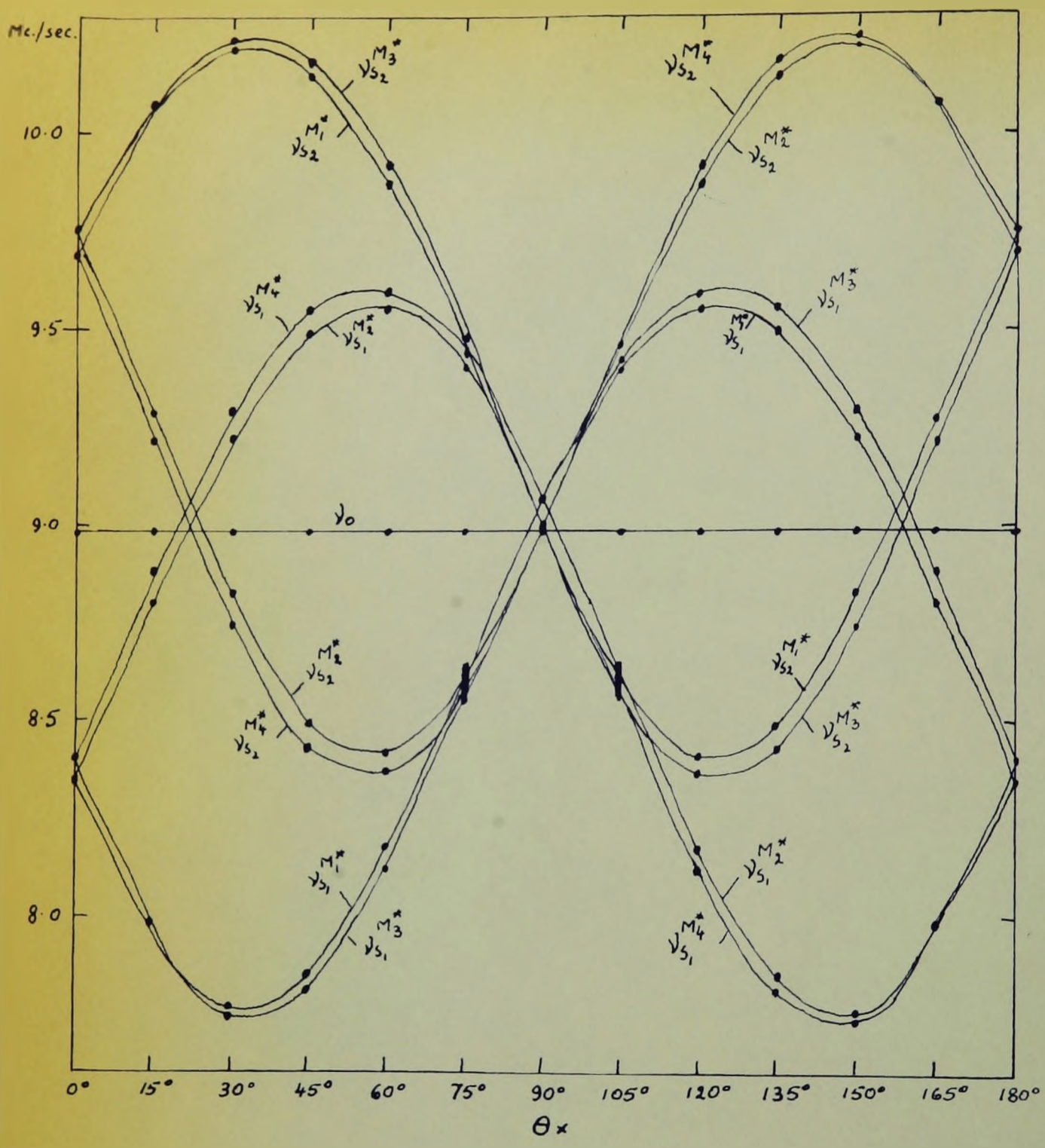

Fig. 12. The Rotation Pattern of the B^{11} Lines Depending Strongly Upon $2\theta x$ in Colemanite at -40° C.

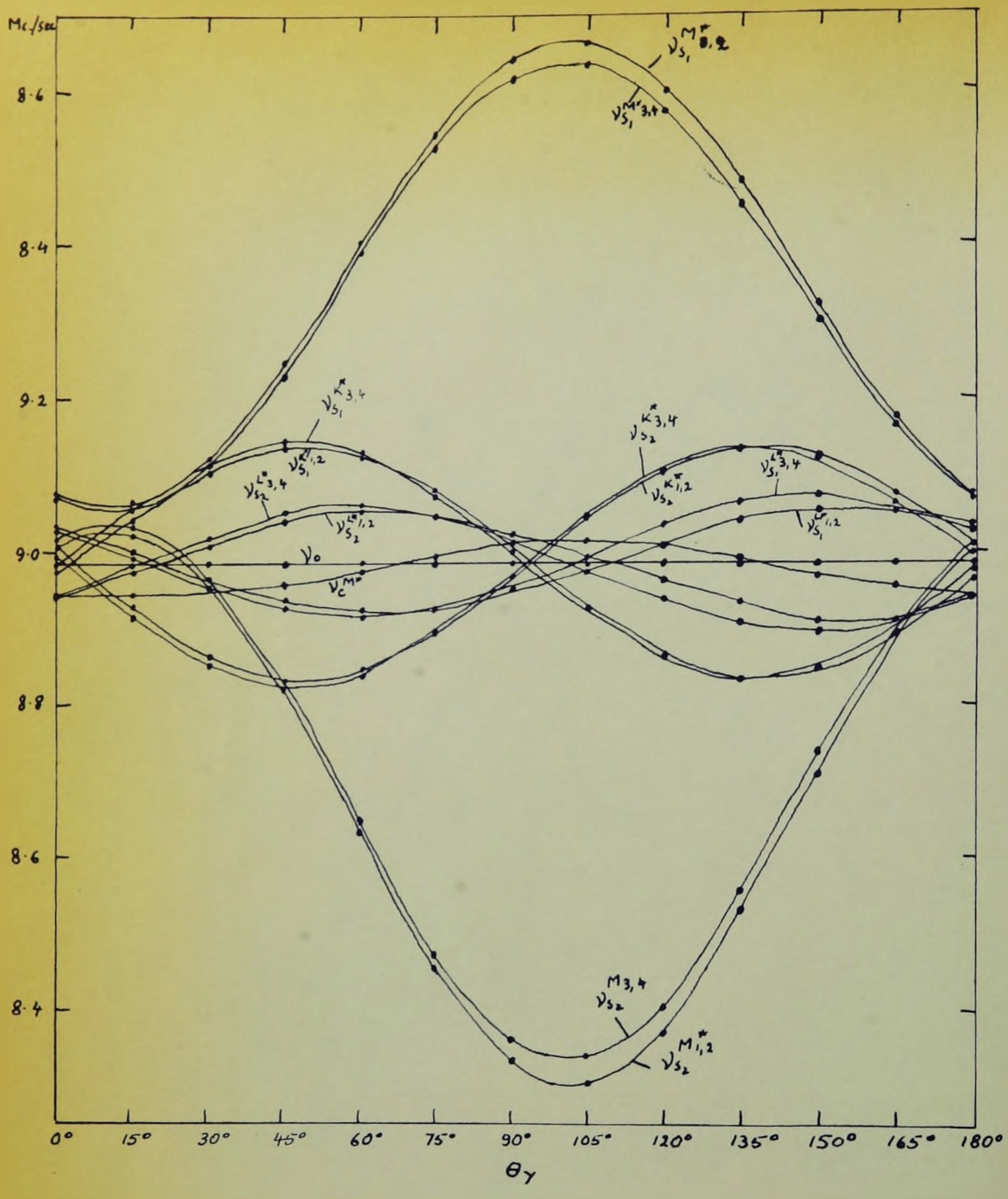

Fig. 13. The Rotation Pattern of all the B^{11} Lines in Colemanite at -40° C. for the Rotation about the Y-Axis.

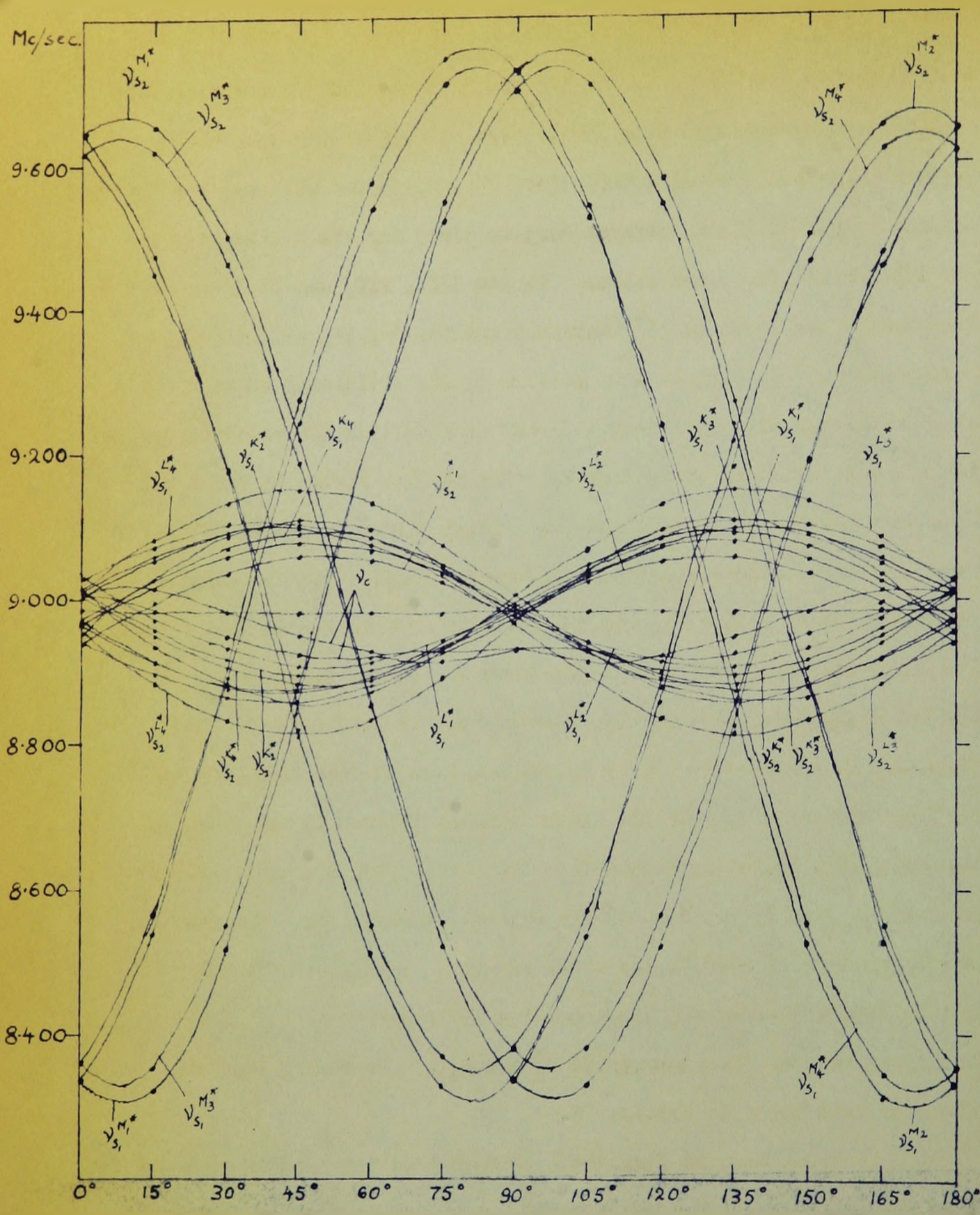

Fig. 14. The Rotation Pattern of all the B^{11} Lines in Colemanite at -40° C. for the Rotation about the Z-Axis.

to the crystal position which is defined in Table XX. The spectrum in Fig.10(b) corresponds to $\theta_y = 150^\circ$. Even though it was obtained with a perfectly general crystal orientation, Fig.10(a) does not show the observed maximum number of lines, because certain lines for the K sites overlap for this particular orientation. Tables XIII, XIV, and XV list the frequencies of the lines at 15° intervals for the X-, Y-, and Z-rotations, respectively. As explained in Section III.4, additional measurements at 5° intervals have been made in order to establish the rotation pattern but are not listed in these tables. The results listed in Table XIII have been plotted in Figs.11 and 12. Those listed in Tables XIV and XV have been plotted in Figs.13 and 14, respectively. The frequencies listed in Tables XIII - XV, and the scale of frequencies in Figs. 11-14, are different from their room temperature analogues, i.e,, Tables I - III and Figs. 6-9, respectively, because ν_o in this case was 8.985 mc./sec., as compared to $\nu_o = 11.981$ mc./sec. at room temperature. The line widths of most of the lines were, as at room temperature, of the order of 5 kc./sec., measured in the usual way, and their relative intensities were independent of the crystal orientation. One feature of the spectrum at -40° C. was found puzzling, namely, consistently smaller intensities of the lines bearing the superscript M_3^* and M_4^* than those bearing the superscript M_1^* and M_2^*. We shall, however, return to this topic in Section IV.

An inspection of Figs.11-14 reveals that the rotation pattern consists of 27 curves in the X- and Z-rotations and 14 in the Y-rotation. A comparison of Figs.11-14 with their room temperature analogues, Figs.6-9,

confirms the following:

(a) The curves denoted by superscripts M_1^*, M_2^*, M_3^*, and M_4^* have comparable amplitude with their room temperature analogues, i.e., the curves belonging to the sites $M_{1,3}$ and $M_{2,4}$. In the same way, the curves having the superscripts K_i^*, K_j^*, L_i^* and L_j^* are similar to the room temperature curves belonging to the sites $K_{i,j}$ and $L_{i,j}$, respectively.

(b) At -40° C., as at room temperature, ν_o stands out by its great intensity, as exemplified by Figs.10(a) and (b), and by its lack of angular dependence.

In consequence of this similarity the spectral lines can be grouped at -40° C. in exactly the same way as they were grouped at room temperature.

(i) The first group contains 8 satellite lines (4 pairs).

(ii) The second group contains 4 central lines which, however, were not resolved and appeared as 2 lines, except for a small splitting at certain crystal orientations.

(iii) The third group contains 16 satellite lines (8 pairs).

(iv) ν_o represents 8 separate, though unresolved, central lines.

We can conclude that the n.m.r. spectrum of B^{11} in colemanite at -40° C. contains 36 lines and therefore the unit cell of colemanite at -40° C. contains 12 boron sites at which ∇E differs in some respect.

We can establish the point group of colemanite at -40° C. as follows. The presence of the 12 boron sites per unit cell of colemanite at -40° C. at which $\tilde{\nabla E}$ differs in some respects proves that the crystal

has lost the centre of symmetry. Referring now to Figs.11, 12, and 14, it can be seen that the rotation pattern is symmetric with respect to $\theta = 0^{\circ}$ and 90°, and that the reduced spectrum occurs at these crystal orientations. Figs.10(b) and 13 show that the reduced spectrum also occurs throughout the entire Y-rotation. Hence, the Y-axis must be parallel either to a two-fold rotation axis or to the normal to a mirror plane, but it cannot be parallel to both of them simultaneously since the crystal structure is no longer centrosymmetric. The point group is therefore either 2 or m.* Incidentally, the fact that there are 12 boron sites detectable by the n.m.r. method at -40° C. establishes also the centrosymmetric structure of colemanite at room temperature.

The logic behind the system of classification of the lines will now become clear. In the foregoing pages we stressed the similarity between the room temperature and -40° C. spectra. This similarity will deepen even more on comparing the corresponding quadrupole coupling constants and the orientation of the principal axes of the tensor $\tilde{\nabla E}$ at the two temperatures. In view of this it should not be surprising that it has been possible to assign each line of the spectrum at -40° C. to its parent line at room temperature. The disappearance of the centre of symmetry has caused any two sites, formerly related by the centre, to become non-equivalent, i.e., the two identical $\tilde{\nabla E}$'s at room temperature have become non-equivalent at -40° C. In accordance with this, the room temperature sites are denoted by $P_{i,i+2}$; the two sites at -40° C. are denoted by P_i^* and P_{i+2}^* as follows:

---

*In the next chapter we shall establish that the point group of colemanite at -40° C. is 2.

TABLE XVI

The Separations, in Kc./Sec., of the B^{11} Satellite Lines for the K^* Sites in Colemanite at -40° C.

Rotation		0°	15°	30°	45°	60°	75°	90°	105°	120°	135°	150°	165°
X	K_1^*	5	-41	-85	-88	-61	-17	43	105	138	141	117	61
	K_2^*	5	67	116	142	135	108	43	-18	-67	-97	-87	-41
	K_3^*	19	-67	-116	-142	-120	-64	15	100	157	176	160	97
	K_4^*	20	100	155	182	100	108	16	-68	-126	-141	-117	-67
Y	$K_{1,2}^*$	43	-110	-240	-303	-283	-192	-48	112	235	295	285	186
	$K_{3,4}^*$	16	-137	-271	-315	-291	-182	-35	124	246	307	270	108
Z	K_1^*	-48	-136	-199	-219	-187	-99	5	103	170	185	152	68
	K_2^*	-48	64	149	186	176	99	5	-103	-180	-222	-205	-136
	K_3^*	-34	-136	-201	-219	-187	-99	19	127	203	211	177	68
	K_4^*	-36	64	176	205	203	128	20	-93	-180	-222	-205	-136

TABLE XVII

The Separations, in Kc./Sec., of the B^{11} Satellite Lines for the L^* Sites in Colemanite at -40° C.

Rotation		0°	15°	30°	45°	60°	75°	90°	105°	120°	135°	150°	165°
X	L_1^*	13	-21	-63	-99	-120	-119	-99	-68	-32	10	36	35
	L_2^*	12	31	32	11	-27	-64	-98	-115	-126	-97	-63	-22
	L_3^*	36	12	-22	-53	-84	-108	-90	-68	-32	4	36	43
	L_4^*	35	44	32	7	-27	-64	-90	-105	-91	-56	-26	10
Y	$L_{1,2}^*$	-99	-28	43	102	133	122	84	23	-47	-109	-148	-142
	$L_{3,4}^*$	-90	-9	73	121	133	122	55	-23	-102	-159	-180	-154
Z	L_1^*	84	-22	-102	-147	-144	-80	13	117	203	247	242	184
	L_2^*	84	180	238	248	203	117	12	-84	-144	-151	-104	-19
	L_3^*	54	-91	-210	-265	-223	-117	36	186	296	342	306	200
	L_4^*	55	199	305	342	299	186	35	-117	-222	-257	-211	-88

TABLE XVIII

The Separations, in Kc./Sec., of the Satellite Lines for the M^* Sites in Colemanite at -40° C.

Rotation		0°	15°	30°	45°	60°	75°	90°	105°	120°	135°	150°	165°
X	M_1^*	1387	2113	2455	2304	1709	844	-74	-795	-1147	-1001	-413	451
	M_2^*	1387	468	-402	-997	-1138	-807	-74	833	1708	2303	2458	2117
	M_3^*	1320	2099	2487	2367	1781	897	-69	-849	-1236	-1116	-536	355
	M_4^*	1320	367	-524	-1114	-1236	-858	-69	886	1779	2365	2492	2104
Y	$M_{1,2}^*$	-68	-39	-165	-429	-774	-1096	-1309	-1358	-1231	-961	-616	-299
	$M_{3,4}^*$	-61	-22	-152	-403	-760	-1063	-1259	-1293	-1165	-904	-572	-270
Z	M_1^*	-1318	-1339	-991	-367	360	992	1387	1411	1069	447	-285	-923
	M_2^*	-1318	-921	-299	455	1063	1409	1387	1003	369	-363	-992	-1335
	M_3^*	-1264	-1267	-923	-322	360	963	1323	1329	993	391	-306	-904
	M_4^*	-1264	-903	-299	397	394	1324	1323	975	369	-320	-923	-1267

TABLE XIX

Experimental Fourier Coefficients, in Kc./Sec., of the Separations of the B^{11} Satellite Lines for all Sites in Colemanite at -40° C.

Rotation	Site	a	b	c
X	K_1^*	26.50	-19.91	-114.72
	K_2^*	25.50	-18.82	117.78
	K_3^*	17.92	0.38	-160.15
	K_4^*	19.00	0.85	162.45
Y	$K_{1,2}^*$	-1.67	45.43	-300.20
	$K_{3,4}^*$	-8.33	25.02	-310.17
Z	K_1^*	-17.08	-21.73	-203.35
	K_2^*	-17.92	-22.98	203.98
	K_3^*	-5.92	-26.03	-218.35
	K_4^*	-6.33	-29.12	216.53
X	L_1^*	-43.92	58.10	-54.07
	L_2^*	-43.83	55.63	54.67
	L_3^*	-27.17	65.17	-31.30
	L_4^*	-27.58	63.35	34.37
Y	$L_{1,2}^*$	-5.56	-91.88	106.47
	$L_{3,4}^*$	-17.75	-73.48	141.27
Z	L_1^*	49.58	36.63	-198.98
	L_2^*	48.33	36.72	199.28
	L_3^*	42.83	10.68	-300.05
	L_4^*	43.83	10.82	298.67

TABLE XIX (Continued)

Rotation	Site	a	b	c
X	M_1^*	652.75	729.83	1652.08
	M_2^*	654.67	736.68	-1647.65
	M_3^*	625.00	695.93	1743.10
	M_4^*	626.00	702.85	-1740.38
Y	$M_{1,2}^*$	-695.42	614.25	263.22
	$M_{3,4}^*$	-660.33	597.65	242.42
Z	M_1^*	36.92	-1349.57	-409.48
	M_2^*	38.17	-1351.58	404.85
	M_3^*	31.00	-1290.58	-360.15
	M_4^*	33.83	-1291.62	359.18

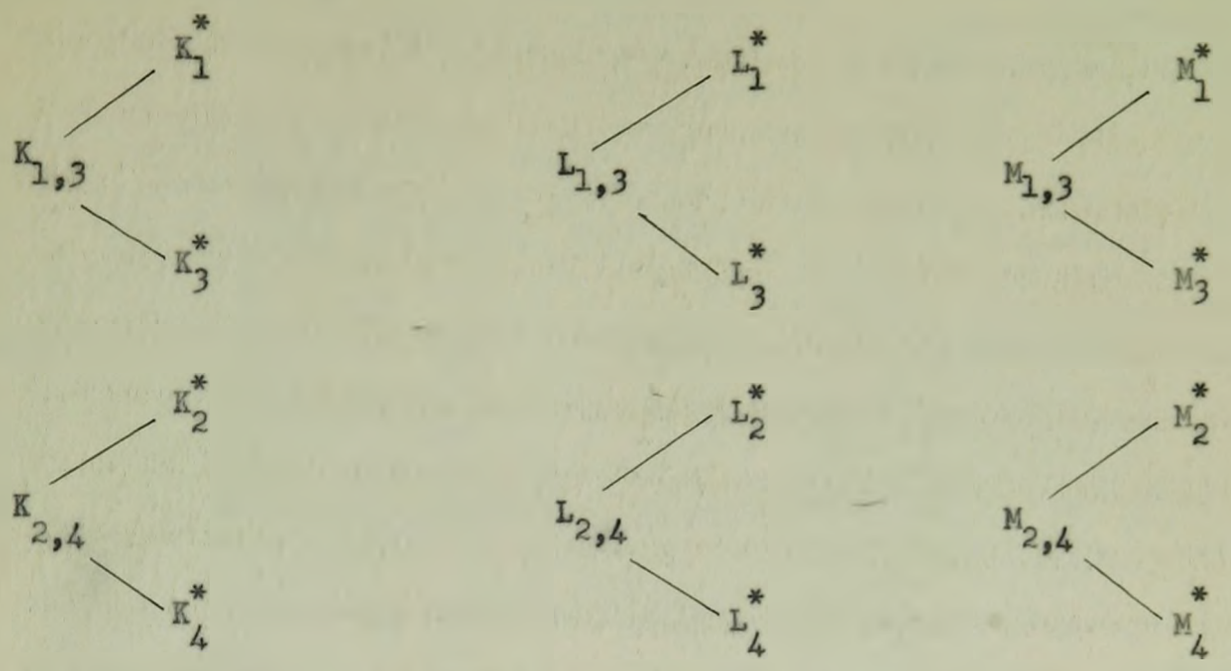

The symmetry-equivalent sites at -40° C. are P_1^* and P_2^*, or P_3^* and P_4^*. In all other respects the nomenclature has been preserved.

IV. 5. The quantitative analysis of the angular dependence of the n.m.r. lines has been performed in the same way as described in Section IV.3. The values of the separation between the satellite lines, $\Delta\nu$ have been deduced from Tables XIII - XV and are listed in Tables XVI, XVII and XVIII for each of the K^*, L^* and M^* sites, respectively. The values of $\bar{\nu}^{M_i^*} - \nu_o$ and of $\nu_c^{M_i^*} - \nu_o$ have not been listed since they are not essential in the analysis of the spectra at -40° C. (see, however, below). The Fourier analysis of the data in Tables XVI - XVIII has been carried out as described in Section IV. The resulting values of the coefficients a_i, b_i, c_i are listed in Table XIX for all the sites.

According to the evidence presented in the previous section, the sites P_1^* and P_2^*, or P_3^* and P_4^*, are related by a two-fold symmetry axis; therefore they possess numerically identical $\nabla\tilde{E}$'s which differ only

TABLE XX

A Comparison of the Values of $\Delta\nu$ Predicted for Specified Crystal Orientation. Assuming the Possible Sign Combinations of C_z and C_x, with the Experimental Values of $\Delta\nu$.

Site	Sign Combination	$\Delta\nu$ Kc./sec.	Sign Combination	$\Delta\nu$ Kc./sec	Experimental $\lvert\Delta\nu\rvert$ Kc./sec.
K_1^*	$=$	+ 322	$\pm$	+ 292	314
K_2^*	$\overset{+}{+}$	+ 270	$\overset{-}{+}$	+ 300	258
K_3^*	$=$	+ 322	$\pm$	+ 290	314
K_4^*	$\overset{+}{+}$	+ 260	$\overset{-}{+}$	+ 292	258
L_1^*	$=$	-123	$\pm$	-151	127
L_2^*	$\overset{+}{+}$	-162	$\overset{-}{+}$	-133	166
L_3^*	$=$	-152	$\pm$	-196	152
L_4^*	$\overset{+}{+}$	-202	$\overset{-}{+}$	-158	196

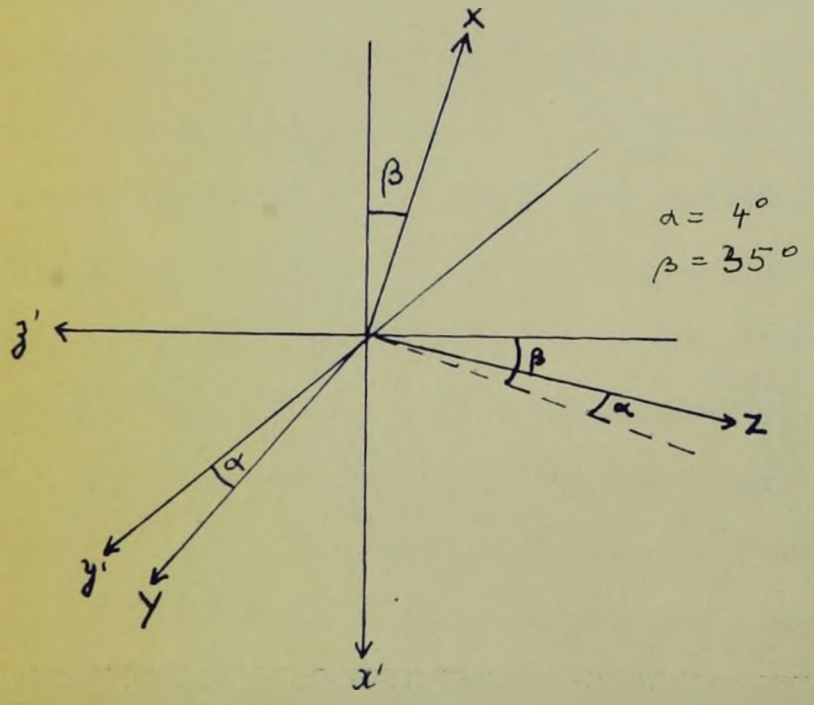

TABLE XXI

Components, in Kc./Sec., of the Tensor Ψ_{ii} for the B^{11} Sites K^* in Colemanite at -40° C.

Site	Rotation	Ψ_{XX}	Ψ_{YY}	Ψ_{ZZ}	Ψ_{XY}	Ψ_{YZ}	Ψ_{ZX}
	X	-53.00	6.58	46.42		114.72	
K_1^*	Y	-47.10	3.34	43.76			300.20
	Z	-38.81	4.65	34.16	203.35		
	X	-51.00	6.68	44.32		-117.78	
K_2^*	Y	-47.10	3.34	43.76			300.20
	Z	-40.90	5.06	35.84	-203.98		
	X	-35.84	18.30	17.54		160.15	
K_3^*	Y	-33.35	16.66	16.69			310.17
	Z	-31.95	20.11	11.84	218.35		
	X	-38.00	19.85	18.15		-162.45	
K_4^*	Y	-33.35	16.66	16.69			310.17
	Z	-35.45	22.79	12.66	-216.53		

TABLE XXII

Components, in Kc./Sec., of the Tensor Ψ_{ij} for the B^{11} Sites L^* in Colemanite at -40° C.

Site	Rotation	Ψ_{xx}	Ψ_{yy}	Ψ_{zz}	Ψ_{xy}	Ψ_{yz}	Ψ_{zx}
	X	87.84	14.18	-102.02		54.07	
L_1^*	Y	86.38	11.00	-97.38			-106.47
	Z	86.21	12.95	-99.16	198.98		
	X	87.66	11.80	-99.46		-54.67	
L_2^*	Y	86.38	11.00	-97.38			-106.47
	Z	85.05	11.61	-96.66	-199.28		
	X	54.34	38.00	-92.34		31.30	
L_3^*	Y	55.73	35.50	-91.23			-141.27
	Z	53.51	32.15	-85.66	300.05		
	X	55.16	35.71	-90.93		-34.37	
L_4^*	Y	55.73	35.50	-91.23			-141.27
	Z	54.65	33.01	-87.66	-298.67		

TABLE XXIII

Components, in Kc./Sec., of the Tensor Ψ_{ii} for the B^{11} Sites M^* in Colemanite at -40° C.

Site	Rotation	Ψ_{xx}	Ψ_{yy}	Ψ_{zz}	Ψ_{zy}	Ψ_{yz}	Ψ_{zx}
	X	-1305.50	1382.58	-77.08		-1652.08	
M_1^*	Y	-1309.67	1390.84	-81.17			-263.22
	Z	-1312.65	1386.49	-73.84	409.48		
	X	-1309.34	1391.35	-82.01		1647.65	
M_2^*	Y	-1309.67	1390.84	-81.17			-263.22
	Z	-1313.41	1389.75	-76.34	-404.85		
	X	-1250.00	1320.93	-70.93		-1743.10	
M_3^*	Y	-1257.98	1320.66	-62.68			-242.42
	Z	-1259.58	1321.58	-62.00	360.15		
	X	-1252.00	1328.85	-76.85		1740.38	
M_4^*	Y	-1257.98	1320.66	-62.68			-242.42
	Z	-1257.79	1325.45	-67.66	-359.18		

TABLE XXIV

Averages of the Components, in Kc./Sec., of the Tensor Ψ_{ij} for all B^{11} Sites in Colemanite at -40° C.

	Ψ_{xx}	Ψ_{yy}	Ψ_{zz}	Ψ_{xy}	Ψ_{yz}	Ψ_{zx}
$K^*_{1,2}$	-46.318	4.943	41.375	203.665	116.250	300.20
$K^*_{3,4}$	-34.657	19.062	15.595	217.440	161.300	310.170
$L^*_{1,2}$	86.587	12.090	-98.677	199.130	54.370	106.470
$L^*_{3,4}$	54.853	34.988	-89.841	299.360	32.835	-141.270
$M^*_{1,2}$	-1310.040	-1388.642	-78.602	407.165	1649.865	-263.220
$M^*_{3,4}$	-1255.888	1323.021	-67.133	359.665	1741.740	-242.420

in the orientation of their principal axes. We encounter, therefore, the same problem of assigning the appropriate signs to the off-diagonal components of $\tilde{\nabla}E$. However, in view of the similarity of the spectrum at -40° C. to that at room temperature, one expects that $\tilde{\nabla}E$'s at the sites $P_{i,i+2}$, P_i^* and P_{i+2}^* should be similar, i.e., their corresponding off-diagonal components should have the same signs. In the case of the M^* sites this can be easily established simply by inspecting the curves $\nu_c^{M_{i,i+2}^*}$ in Figs. 11-14 and noting that they have the same shape as their analogues at room temperature, i.e., they contain nearly the same coefficient r_i measured at the same Ho. In the case of the K^* and L^* sites, however, this cannot be so easily established and therefore an additional measurement was done in the manner indicated in Section II.5. The results of this measurement are presented in Table XX, where only the K^* and L^* sites are listed. As can be seen, the off-diagonal components of $\tilde{\nabla}E$'s at sites P_i^* and P_{i+2} must have the same signs as those at the sites $P_{i,i+2}$, since they predict the experimental results. Accompanying Table XX is the diagram indicating the crystal orientation at which the measurement was done. Incidentally, the spectrum of Fig.10(a) also corresponds to this crystal orientation.

The numerical values of a_i, b_i and c_i in Table XIX have been used to determine the tensor components, Ψij, for each of the sites. Tables XXI, XXII and XXIII list the results for K^*, L^* and M^* sites, respectively, and Table XXIV lists the averages for all the sites. The results in Table XXIV have been used in the diagonalisation process which was carried out in the usual way. The resulting values of the quadrupole

TABLE XXV

Quadrupole Coupling Constants and Asymmetry Parameters at Room Temperature and at -40° C. at the B^{11} Sites in Colemanite.

Boron Sites	Quadrupole Coupling Constant,		Asymmetry Parameter,	
	Room Temp.	-40° C.	Room Temp.	-40° C.
K_1, K_2	0.436 ± .002	0.421 ± .005	0.48 ± .01	0.57 ± .01
K_3, K_4		0.462 ± .005		0.43 ± .01
L_1, L_2	0.309 ± .002	0.259 ± .005	0.83 ± .01	0.86 ± .01
L_3, L_4		0.359 ± .005		0.79 ± .01
M_1, M_2	2.540 ± .003	2.521 ± .003	0.058±0.001	0.086 ± .001
M_3, M_4		2.552 ± .003		0.023 ± .001

TABLE XXVI

Direction Cosines of the Principal (x, y, z) Axes of $\tilde{\nabla E}$ with Respect to the (X, Y, Z) Axes at all B^{11} Sites in Colemanite at Room Temperature. The Two Sets of Signs Given for Each Set of Cosines Refer to the Two Sites Related by the Two-Fold Axis. The Signs Are Relative Only.

Boron Sites	Axis	Principal Axes x	y	z
	X	$\mp$ 0.138 $\pm$ 0.005	$\mp$0.781 $\pm$ 0.005	$\pm$0.609 $\pm$ 0.005
K	Y	+ 0.827 $\pm$ 0.005	+0.247 $\pm$ 0.005	+0.505 $\pm$0.005
	Z	$\mp$ 0.545 $\pm$ 0.005	$\pm$0.574 $\pm$ 0.005	$\pm$ 0.611 $\pm$ 0.005
	X	$\pm$ 0.258 $\pm$ 0.005	$\pm$0.603 $\pm$ 0.005	$\mp$ 0.754 $\pm$ 0.005
L	Y	- 0.527 $\pm$ 0.005	-0.567 $\pm$ 0.005	-0.633 $\pm$ 0.005
	Z	$\mp$ 0.810 $\pm$ 0.005	$\pm$0.561 $\pm$ 0.005	$\pm$ 0.172 $\pm$ 0.005
	X	$\mp$ 0.115 $\pm$ 0.002	$\mp$0.991 $\pm$ 0.002	$\mp$0.123 $\pm$ 0.002
M	Y	- 0.538 $\pm$ 0.002	+0.126 $\pm$ 0.002	- 0.826 $\pm$ 0.002
	Z	$\mp$ 0.835 $\pm$ 0.002	$\pm$0.036 $\pm$ 0.002	$\pm$0.549 $\pm$ 0.002

TABLE XXVII

Direction Cosines of the Principal (x,y,z) Axes of E with Respect to the (X,Y,Z) Axes at all B^{II} Sites in Colemanite at -40° C. The Two Sets of Signs Given for Each Set of Cosines Refer to the Two Sites Related by the Two-Fold Axis. The Signs Are Relative.

Boron Sites	Axis	Principal Axes x	y	z
	X	∓ 0.078 ±0.01	∓0.786 ±0.01	± 0.613 ± 0.01
$K^{*}_{1,2}$	Y	+ 0.830	+ 0.289	+0.476
	Z	∓ 0.552	± 0.546	± 0.631
	X	± 0.184 ±0.01	±0.775 ±0.01	∓0.604 ± 0.01
$K^{*}_{3,4}$	Y	-0.831	-0.206	-0.517
	Z	± 0.525	∓0.597	∓ 0.606
	X	∓ 0.295 ± 0.01	±0.544 ±0.01	∓0.785 ± 0.01
$L^{*}_{1,2}$	Y	-0.566	-0.562	-0.603
	Z	∓ 0.770	± 0.623	±0.142
	X	∓ 0.208 ± 0.01	∓ 0.649 ±0.01	±0.731 ± 0.01
$L^{*}_{3,4}$	Y	+ 0.409	+0.590	+ 0.657
	Z	± 0.858	∓ 0.480	∓ 0.182
	X	± 0.005 ± 0.002	∓ 0.992 ± 0.002	± 0.126 ±0.002
$M^{*}_{1,2}$	Y	-0.544	-0.108	-0.832
	Z	± 0.839	∓ 0.064	∓ 0.541
	X	∓ 0.018 ±0.002	±0.993 ± 0.002	∓ 0.113 ±0.002
$M^{*}_{3,4}$	Y	+ 0.559	+0.103	+0.823
	Z	∓ 0.829	±0.050	± 0.557

coupling constants and the asymmetry parameters, and their estimated experimental errors, are listed in the second and fourth columns of Table XXV. The resulting values of the direction cosines of the principal axes of $\hat{\nabla E}$ with respect to the (X, Y, Z) axes, and the estimated experimental error, are listed in Table XXVII. The results listed in Tables XXV - XXVII will be discussed in Chapter V of this thesis.

IV. 6. For the investigation of the temperature dependence of the resonance lines, the crystal was accurately aligned so that its Y-axis coincided with the rotation axis. This choice of orientation was made for the following reasons. Firstly, at room temperature the lines are more intense for this orientation. Secondly, for this crystal orientation any departure from the room temperature symmetry shows up in an obvious way. Thirdly, the alignment of the Y-axis parallel to the rotation axis could be made to better than 10 minutes. Each of the three sites, K, L and M, were examined; K sites were examined at $\theta_y = 35^\circ$ while L and M sites were examined at $\theta_y = 149^\circ$. The investigation of these sites consisted of recording the satellites at selected temperatures over the range $+52^\circ$ C. to -136° C.

We shall first describe the results obtained over the temperature range $+25^\circ$ C. to -16° C., which includes the Curie point. Table XXVIII lists the observed values of the separation of the satellite lines belonging to the K, L and M sites. Because the changes of the lines were quite small, separations rather than actual frequencies of the satellite lines have been used to eliminate the errors due to drift of the magnetic field. The values listed in Table XXVIII are plotted in

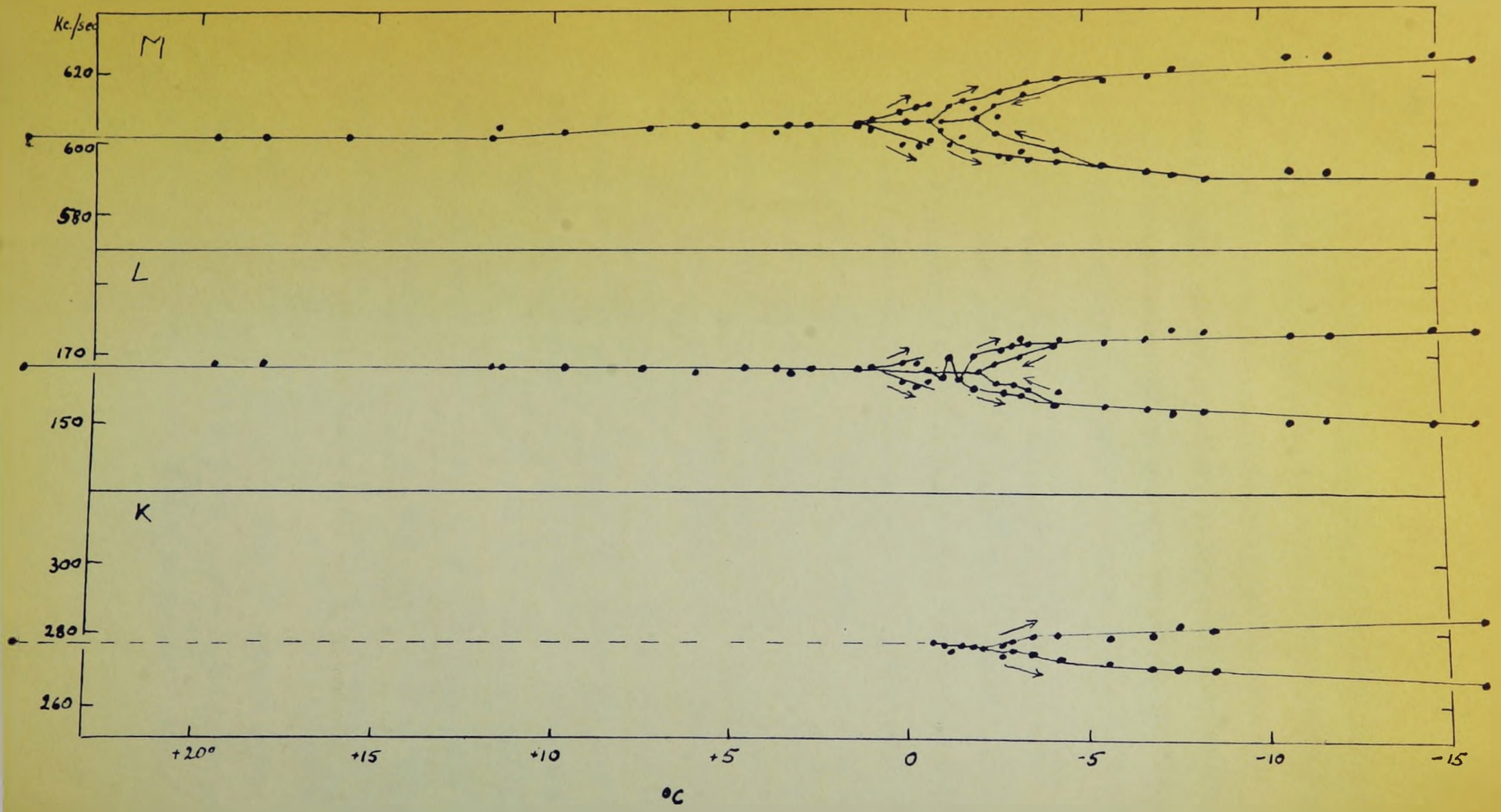

Fig. 15. Temperature Dependence of a Selected Set of Satellite Lines for all B^{11} Sites in Colemanite for $\theta y = 35^{o}$ (K Sites) and for $\theta y = 149^{o}$ (L and M Sites).

Fig.15 and the direction of temperature cycling is indicated.

An inspection of Fig.15 reveals that there is no clear-cut transition temperature which is assumed to coincide with the temperature at which the lines are first split. Following are the temperatures at which the splitting clearly occurred for various satellites:

M	L	K
-2.0° C. ↑	-2.0° C. ↑	-3.0° C. ↑
-1.0° C. ↓	-1.9° C. ↓	-2.7° C. ↓
-2.0° C. ↑	-2.5° C. ↑	
0.1° C. ↓	0.1° C. ↓	

The arrow pointing up indicates that the crystal temperature was being increased, while the arrow pointing down indicates that it was being decreased. The scatter of the temperatures at which the splitting was first observed is unlikely to be due to errors in the measurements of the crystal temperatures since great care was exercised to ensure that the temperatures, measured by the thermocouple, corresponded to that of the crystal. The variation in the splitting point is probably directly connected with the history of the crystal, i.e., with the rate at which it has been cooled or warmed up, with the amount of strain present in the crystal, etc. Further details of the results obtained are:

(a) Broadening of the lines belonging to the site M occurs at about $+1^{\circ}$ C. irrespective of the direction of temperature cycling.

(b) There is a consistent increase in the values of $\Delta\nu$ for site M which starts at about $+10^{\circ}$ C. and persists until the lines separate.

TABLE XXVIII

Separation, in Kc./Sec., of the B^{11} Satellite Lines in Colemanite at Various Temperatures. M and L Sites Were Measured at $\theta_y = 149^\circ$, K Sites at $\theta_v = 35^\circ$.

Decreasing Crystal Temperatures

Sites	°C. 25	18.2	15.9	11.7	9.7	7.3	6	4.6	3.4
M	602	602	602	602	604	605	606	607	606
L	166	169	167	167	165	165	167	167	165
K	278								

Sites	°C. 2.9	1.4	0	-0.7	-1	-1.2	-1.6	-1.9	-2.7
M	607	606	608	608	607	612	613	611	616
					605	600	603	598	597
L	166	166	166	166	164	170	163	170	171
								161	160
K				278	277	275	277	276	277
									274

Sites	°C. -2.9	-3.3	-3.4	-4.2	-5.6	-6.8	-7.5	-8.4	-16
M	616	615	618	619	619	620	622		625
	597	599	597	596	595	593	592	590	590
L	173	175	174	173	174	175	178	177	177
	162	159	160	156	156	155	153	154	151
K	278	278	280	280	279	280	283	281	284
	276	275	275	274	272	271	271	271	267

Increasing Crystal Temperatures

Sites	°C. -14.8	-11.9	-10.8	-4.3	-2.6	-2.5	-2	-1
M	626	626	626	618	609	612	609	608
	592	593	594	599	604	604	608	
L	178	176	176	174	167	168	166	166
	150	152	151	160	162	162		

Decreasing Crystal Temperatures

Sites	°C. 27	13.6	11.7	3.7	1	0.1	-0.3	-0.6
M	600	602	605	604	607	609	611	611
						600	600	603
L	167	167	166	167	167	168	167	166
						162	162	163

TABLE XXIX

Separations, in Kc./Sec., of the B^{11} Satellite Lines in Colemanite at Various Temperatures for $\theta_y = 149^\circ$.

Sites	°C.	52	47	43	40	37	33	32	29	25
M		598	597	598	598	598	599	600	600	60
L		170	170	170	168	170	169	168	168	167

Decreasing Crystal Temperatures

Sites	°C.	-46	-50	-60	-62	-75	-84	-126
M		633	633	636	637	640	640	Incomplete
		588	587	587	587	591	644 589	Incomplete
L		-	-	180	-			
		-	-	140	-			

Increasing Crystal Temperatures

Sites	°C.	-136	-99	-90	-87	-68	-60	-44	-38	-29	-22
M		Incomplete	645	647	643	643	642	639	637		
			630	629	634	635	631	634	632	630	628
			596	596	596	594	593	595	592	589	589
			578	577	583	584	582	586	583		
L			-	175	-	178	-	178	-	-	177
				137	138	141	-	140	-	-	147

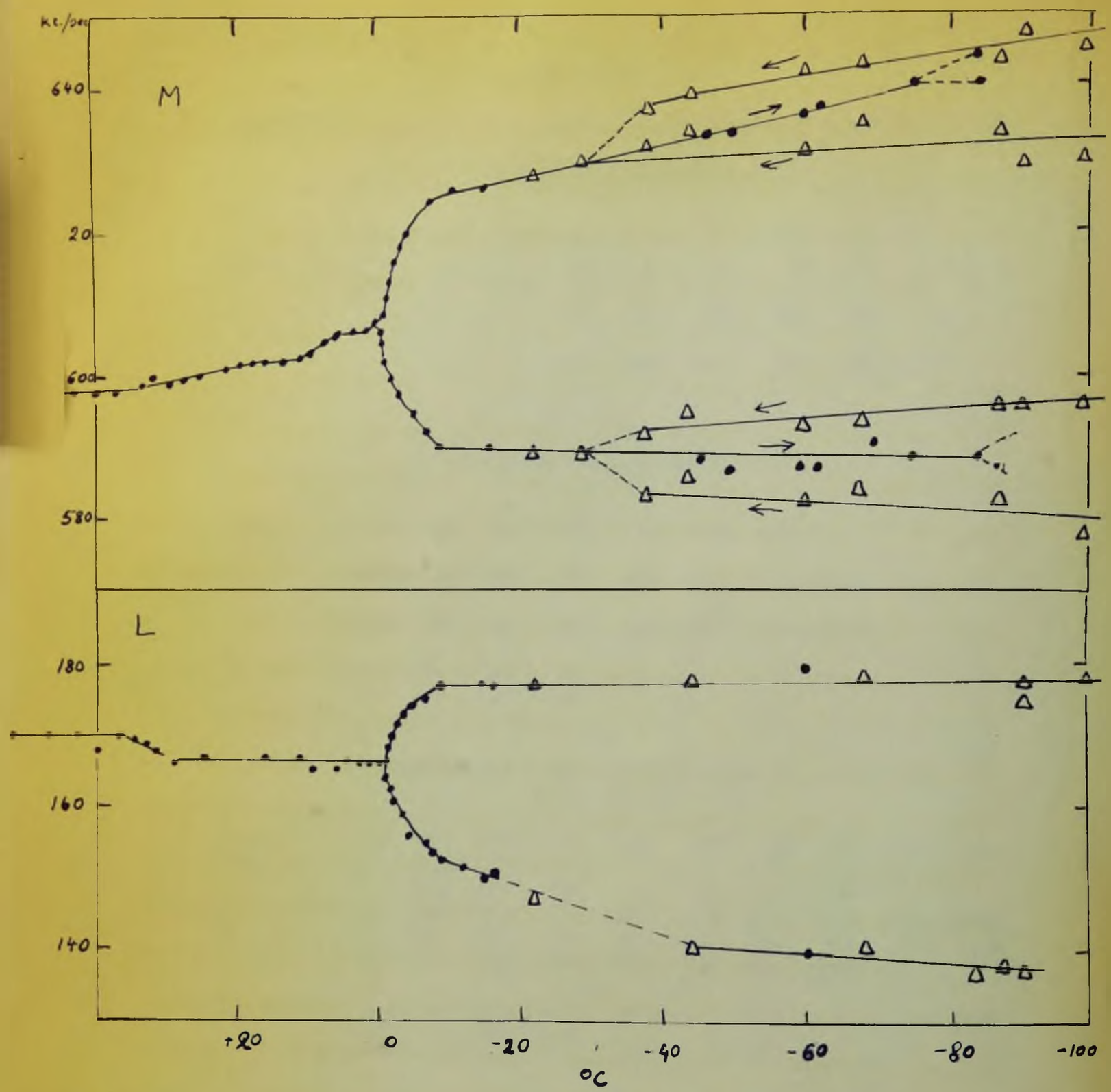

Fig. 16. Temperature Dependence of a Selected Set of Satellite Lines for L and M Sites in Colemanite for $\theta_y = 149^\circ$.

As a final step in this investigation, the spectrum of $\theta_y = 149^\circ$ was examined at crystal temperatures covering the ranges $+52^\circ$ C. to room temperature and -22° C. to -136° C. Table XXIX lists the separation between the satellite lines belonging to the sites L and M. The results listed in Table XXIX, and some results for sites L and M listed in Table XXVIII, are plotted in Fig.16. Referring to Fig.16, there occurs a slight increase in the values of $\Delta\nu$ for site M and a slight decrease in this value for site L as the temperature is lowered from $+52^\circ$ C. to room temperature. The results obtained in the temperature range -22° C. to -136° C. indicate that an additional splitting of the lines belonging to the site M occurs at about -80° C. with decreasing temperatures, and at about -35° C. with increasing temperatures. The satellite lines belonging to the L site were broadened under exactly the same circumstances. These broadenings (L site), and the additional splittings (M site), could arise from two sources. First, the crystal has been misaligned, or second, the crystal has undergone an additional transition. The first case cannot be true. The crystal orientation was repeatedly checked for misalignment before and after each set of measurements. In order to eliminate the possibility of misalignment due to anisotropic thermal contraction of the crystal platform, a perspex platform was used in addition to a lucite platform. These precautions did not influence the above results. The second case must therefore be true, i.e., colemanite undergoes an additional transition. Fig.16 shows that this newly discovered transition is characterised by a large thermal hysteresis loop extending from about -35° C. to about -80° C.

The fact that the lines belonging to the sites $M^*_{1,2}$ and $M^*_{3,4}$ are split, and those belonging to the sites $L^*_{1,2}$ and $L^*_{3,4}$ are broadened, indicates that the two-fold rotation axis has disappeared. In other words, the point group of colemanite in this phase is the triclinic point group 1.

CHAPTER V

DISCUSSION

V. 1. Let us first discuss the room temperature results. The symmetry properties of colemanite have been studied by other workers using three independent methods and following are the conclusions as to its symmetry at room temperature:

(a) X-ray analysis: centrosymmetric, point group 2/m (Christ et al.,'54).

(b) Dielectric breakdown studies: centrosymmetric (Davisson,'56).

(c) Pyroelectric and piezzoelectric studies: non-centrosymmetric (Davisson,'56).

It appears from the above that the evidence for the centrosymmetric structure is not conclusive. Davisson ('56) has proposed that the structure of colemanite remains essentially centrosymmetric at all temperatures, viz. including the room temperature, and that the asymmetry may be due to slight displacements of certain constituents, presumably the light atoms, from centrosymmetric positions.

As was stated in Chapter I, one of our objectives was to check the point group of colemanite at room temperature. As described in Chapter IV, the results supplied an unambiguous answer supporting the centrosymmetric point group 2/m.

At this point one should enquire into the origin of this controversy, viz. the evidence from the piezzoelectric and pyroelectric

studies. Normally, in cases such as this, one would be tempted to accept the results of the pyroelectric and piezzoelectric studies in preference to the X-ray and dielectric breakdown results since the slight displacements from centrosymmetric positions, if such exist, are likely to be associated with the light atoms which have relatively little influence on the X-ray and dielectric breakdown results. However, Chynoweth ('57) has suggested that an ideal crystal of colemanite would show no pyroelectric and piezzoelectric effect at room temperature. According to Chynoweth, the pyroelectric behaviour at room temperature can be explained by either a space-charge field inside the crystal resulting in an induced polarisation when the crystal is in the para-electric state or by a shift of the transition temperature in parts of the crystal as a result of strains. It is interesting to recall at this point that in our preliminary study we encountered many colemanite crystals exhibiting excessively broad lines, a fact which can be blamed on the existence of strains in a single crystal.

V. 2. It is interesting to speculate on a possible correlation between the electric field gradient tensors found in this work and the boron positions proposed by Christ et al. ('54). They propose that the three boron atoms in the asymmetric unit are located near the centres of two slightly distorted O_4 tetrahedra and a slightly distorted O_3 triangle.

In the discussion to follow it will be assumed that only the oxygen nearest-neighbours make significant contributions to $\tilde{\nabla E}$ at each of the boron sites. Let us first consider a BO_4 unit. At the centre of a perfect tetrahedron the symmetry is cubic so that $\tilde{\nabla E}$ must be

identically zero. In a slightly distorted tetrahedron, however, one would expect $\tilde{\nabla}E$ to be small at the centre, although it need no longer be zero, but there seems to be no reason to expect the asymmetry parameter to take any specific value within its range ($0 \leq \eta \leq 1$) or the principal axes to point in any specific direction. Considering now a BO_3 unit, the symmetry of $\tilde{\nabla}E$ at the centre of an equilateral triangle requires that η be zero and that the z-principal axis be along the normal to the plane of the triangle. Unless the O_3 triangle is greatly distorted, η should still be small at the boron site. Also, one might reasonably expect $\tilde{\nabla}E$ to be larger at the boron site near the centre of the slightly distorted equilateral triangle than at the boron sites at the centres of the slightly distorted tetrahedra because in the triangle the average B - O distance is shorter than in the tetrahedra (Christ et al., '54) and the symmetry is not as close to being cubic. As shown in Table XXV, we have indeed found that the quadrupole coupling constants at the B^{11} sites K and L are small and the values of η are not unusual whereas the quadrupole coupling constant is considerably larger and η is very small at the B^{11} sites M. Also, it follows from the atomic coordinates, made available to us through the courtesy of Dr. C. L. Christ of the U. S. Geological Survey, that the z-principal axis of $\tilde{\nabla}E$ at the sites M is nearly normal to the plane of the O_3 triangle. This is shown by the direction cosines with respect to the $\vec{b} \times \vec{c}$, $\vec{b}$, $\vec{c}$ directions, listed below:

axis	$\vec{b} \times \vec{c}$	$\vec{b}$	$\vec{c}$
Direction cosines of z-principal axis	0.123	-0.826	-0.549
Direction cosines of normal to plane	0.109	-0.843	-0.527

These arguments strongly suggest that the boron sites K and L are in the O_4 tetrahedra and the M sites are in the O_3 triangle.

Incidentally, it is of interest to note that the n.m.r. study of the B^{11} sites in kernite (Waterman and Volkoff,'55) revealed that the electric fields existing at boron sites C and D (using Waterman and Volkoff's nomenclature) are very similar to those at our sites K and L; while the electric fields existing at boron sites E and F are very similar to those at our sites M. We summarise our and Waterman and Volkoff's results below:

kernite	C	D	E	F
η	0.54	0.60	0.163	0.117
Q.c.c. (kc./sec.)	645	588	2563	2567
colemanite	K	L	M	
η	0.48	0.83	0.058	
Q.c.c. (kc./sec.)	436	309	2540	

In view of this similarity, we suggest that kernite contains two BO_4 tetrahedra and two BO_3 triangles in the asymmetric unit, contrary to the results of X-ray analysis by Portoles ('47, '48). This idea is supported by Dr. Christ (private communication) on the basis of Morimoto's ('56) X-ray analysis of borax. The structure of borax which, except for the water of hydration, has the same chemical formula as kernite, contains two BO_4 tetrahedra and two BO_3 triangles in its asymmetric unit. Also, Dr. Christ suggested that, since kernite is derived from borax, kernite must contain infinite chains whose unit is formed by two BO_4

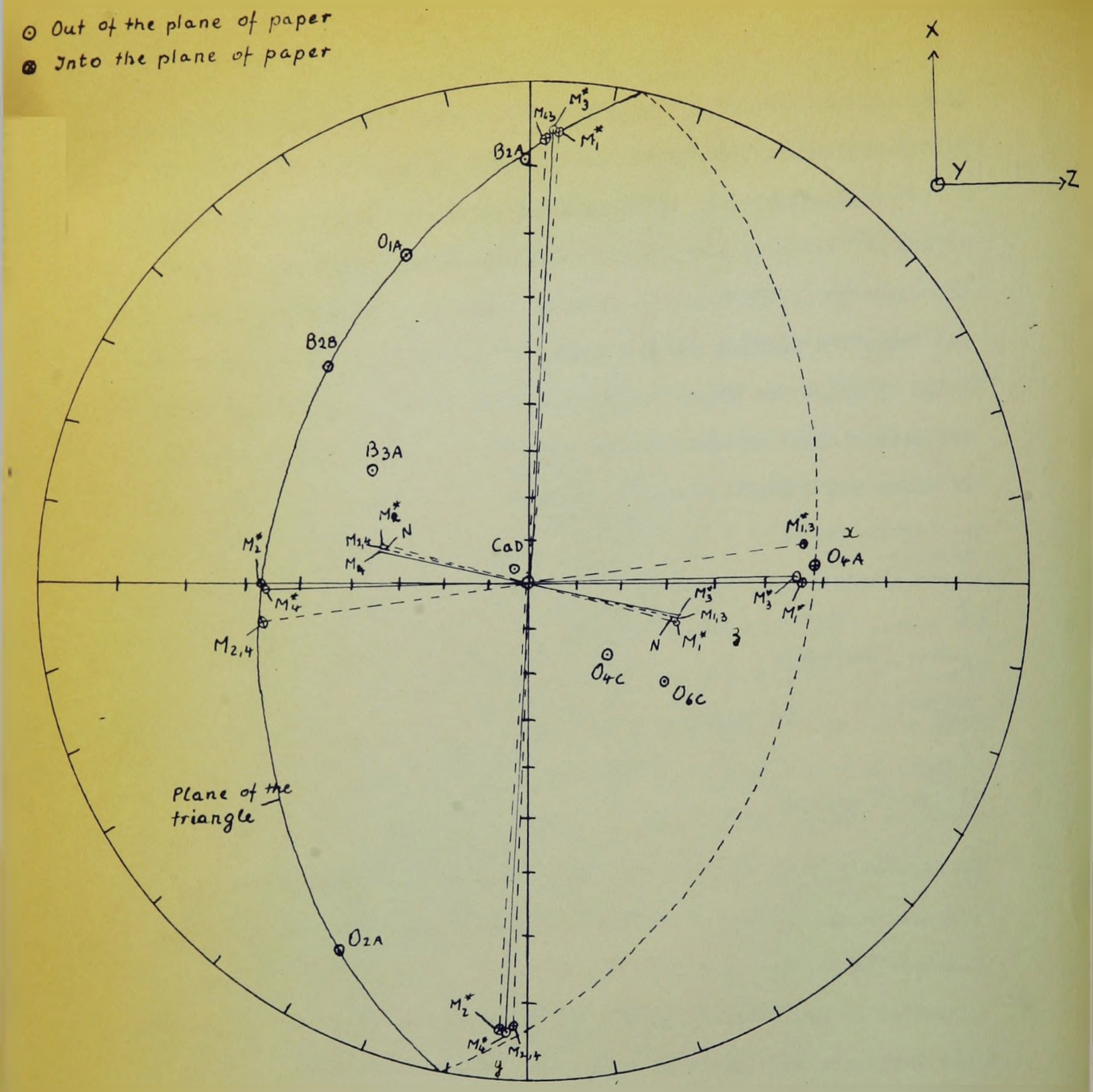

Fig. 17. Stereogram of the Principal Axes of $\nabla\tilde{E}$ at the B^{11} Sites M in Colemanite at Room Temperature and at -40° C., and of the Nearest- and the Next-Nearest-Neighbours as Seen by B_{1A} Boron Atom in Colemanite.

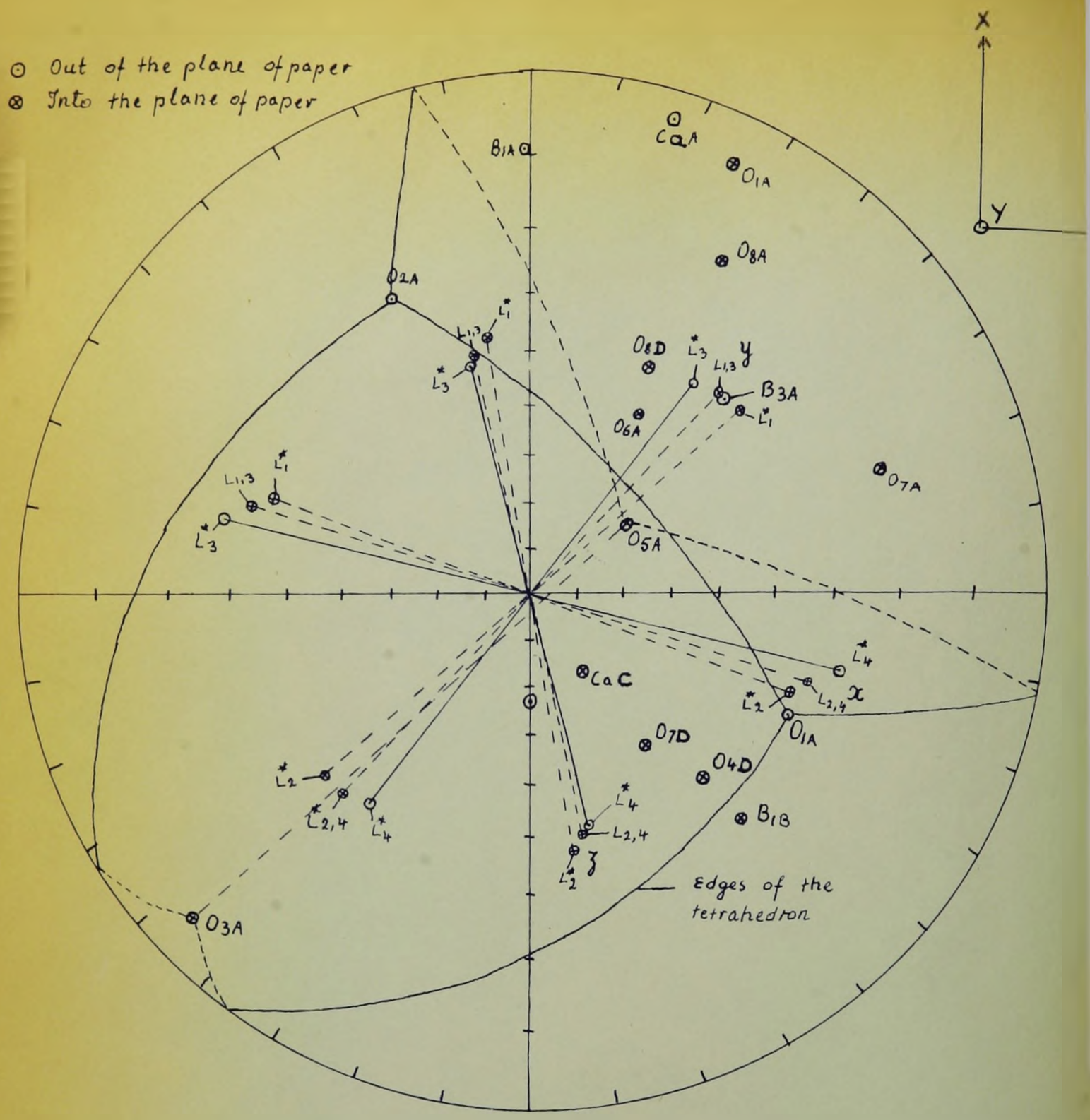

Fig. 18. Stereogram of the Principal Axes of $\bar{\nabla E}$ at the B^{11} Sites L in Colemanite at Room Temperature and at -40° C., and of the Nearest- and the Next-Nearest-Neighbours as Seen by B_{2A} Boron Atom in Colemanite.

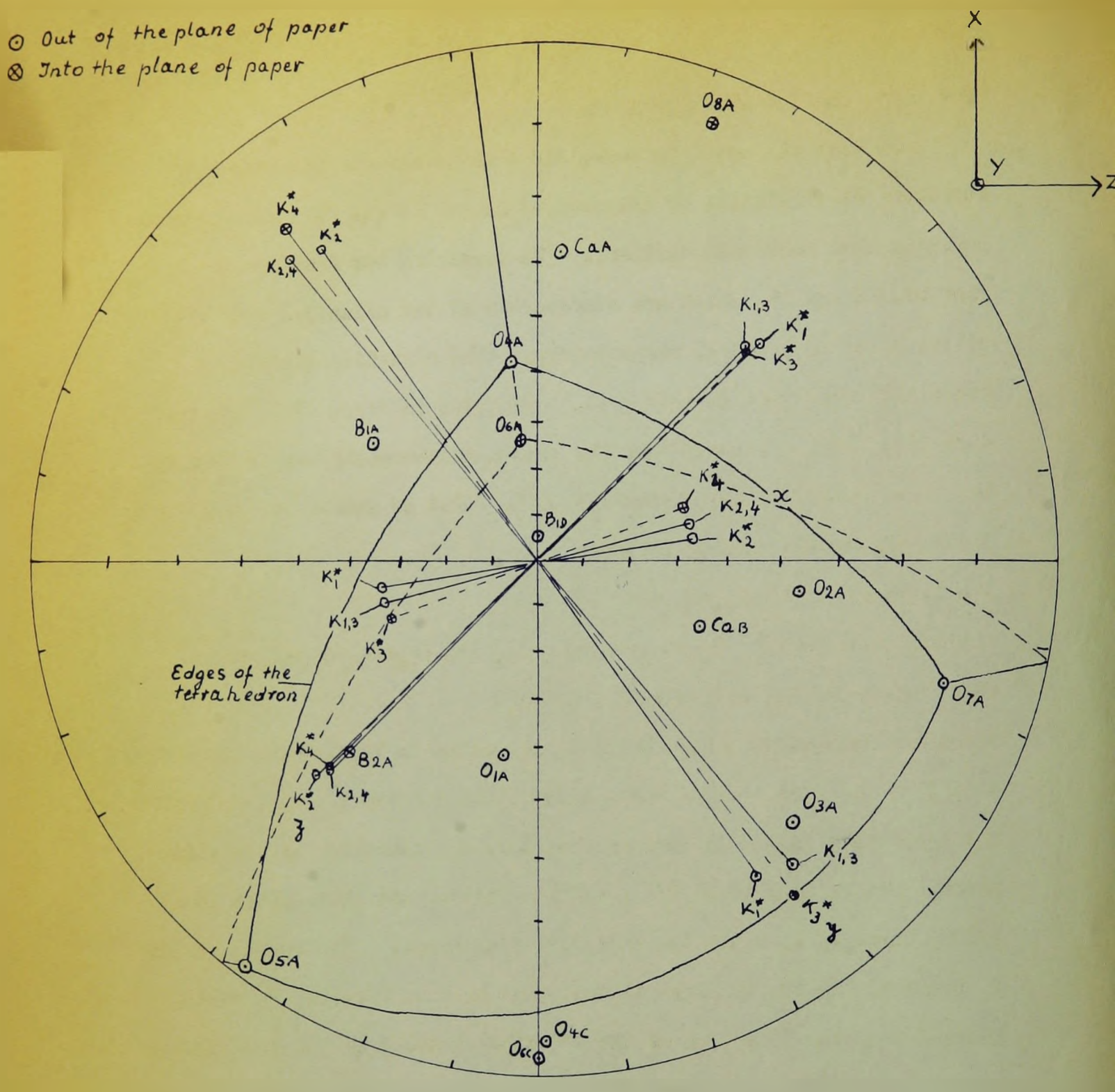

Fig. 19. Stereogram of the Principal Axes of $\overline{\nabla E}$ at the B^{11} Sites K in Colemanite at Room Temperature and at -40° C., and of the Nearest- and the Next-Nearest-Neighbours as Seen by B_{3A} Boron Atom in Colemanite.

tetrahedra and two BO_3 triangles.

We have attempted to correlate closely our results with the structure of colemanite as proposed by Christ et al. ('54, also private communication mentioned earlier). We summarise our findings in Figs.17, 18 and 19, which are stereograms of the principal axes of $\tilde{VE}$'s at the sites M, L and K, respectively. The direction cosines in Table XXVI were used in this plot. Included in Figs. 17-19 are the directions of the nearest- and the next-nearest-neighbours as seen by the three borons in the asymmetric unit. Let us denote one arbitrarily chosen asymmetric unit as follows:

BO_3 triangle: B_{1A}-O_{1A}-O_{2A}-O_{4A}

two BO_4 tetrahedra: B_{2A}-O_{1A}-O_{5A}-O_{2A}-O_{3A} and B_{3A}-O_{7A}-O_{5A}-O_{6A}-O_{4A}

water molecule: O_{8A} and calcium ion, Ca_A.

Two other asymmetric units, B and C, appearing in Figs.17-19, are derived from A by the operation of the a glide plane and the 2_1 axis, respectively. The asymmetric unit D is derived from C by the operation of the glide plane. The 2_1 axis is at 1/4 a and 0xc whereas the glide plane is at 1/4 b, where a, b, c are the unit cell dimensions. The normal to the O_3 plane of the BO_3 triangle is indicated by N in Fig.17. It should be noticed that the insertion of the B^{11} sites L and K in the same stereograms as B_{2A} and B_{3A}, respectively, does not imply that these sites are identical. As can be seen in Fig.17, N is parallel, to within 1^o, to the z-principal axis. The other two principal axes, x and y, are nearly parallel to the B_{1A}-O_{4A} and B_{1A}-B_{2A} lines, respectively. Regarding the K and L sites shown in Figs. 18 and 19, there seems to be no clear-cut

correspondence between their principal axes and the neighbouring atoms as seen by both borons, B_{2A} and B_{3A}, except that the z-axis of K is parallel, to within 7°, to the B_{2A} - B_{3A} direction and so is the y-axis of L, to within 1 1/2°. This fact appears to be significant in that one could picture the electron-cloud of the intervening oxygens, O_{3A}, O_{2A} and O_{1A} to be distorted by the borons, which fact in turn contributes significantly to the non-spherical symmetry of $\tilde{\nabla}$E's at the sites K and L. B_{2A} seems to stand out in another respect. Fig.17 shows that the y-axis of $\tilde{\nabla}$E at the sites M is nearly parallel to B_{1A}-B_{2A} and this fact may also be interpreted in terms of strong polarisation of the intervening oxygen, O_{2A}. Figs. 17-19 include also the orientations of the $\tilde{\nabla}$E's at the boron sites in colemanite at -40° C.

V. 3. Let us now discuss the results obtained at -40° C. Piezzo-electric, pyroelectric and ferroelectric studies of colemanite suggest that the crystal undergoes a transition at about -2° C. below which it is ferroelectric. An X-ray investigation of colemanite in the temperature range 155° C. to -195° C. by Christ ('53) revealed no evidence for such a transition.

We have studied colemanite at -40° C., the results of which study are described in Chapter IV. The doubling of the resonance lines in the spectrum at -40° C., as compared with the room temperature spectrum, has been interpreted as resulting from the lack of a centre of symmetry at -40° C. Thus, on the basis of our results alone we can say that colemanite at -40° C. possesses either the point group 2 or the point group m. Since colemanite at -40° C. is also ferroelectric with the

ferroelectric direction (i.e., the direction of spontaneous polarisation) coinciding with its crystallographic b-axis, the only acceptable point group is 2. Therefore, the alternative point group m has to be rejected.

The results obtained at -40° C. imply a redistribution of charges which is most certainly accompanied by displacements of the atoms from their centrosymmetric positions. At present, it is impossible to say conclusively which atoms have undergone displacements. The possibility of all atoms undergoing displacement in the ferroelectric phase cannot be completely ruled out but it is very unlikely that calcium and oxygens are displaced since displacement of these heavy atoms would be revealed by X-rays on account of their high X-ray scattering cross-section as compared with that of other constituents. It appears then, that hydrogen and boron atoms are the constituents most likely to have undergone displacement.

It is with this advance knowledge that results can be interpreted to a limited extent in terms of atomic movements. For the purpose of discussion, let us first consider the BO_3 triangle. Table XXV shows that the quadrupole coupling constant for the sites $M^*_{1,2}$ has a smaller value whereas that for the sites $M^*_{3,4}$ has a larger value than the quadrupole coupling constant for the sites M. This can be taken to imply that the boron nuclei at the sites $M^*_{1,2}$ have moved farther from and the boron nuclei at the sites $M^*_{3,4}$ have moved closer to the centre of the O_3 triangle, when compared to the boron sites

occupied at room temperature. The values of the asymmetry parameters for the M sites listed in Table XXV support these ideas. As far as the boron sites K and L are concerned, the quadrupole coupling constants at -40° C. split, relative to their room temperature values, into one having a larger value and the other having a smaller value. This fact can be interpreted similarly as in the case of M sites. On one hand the boron nucleus at the site possessing the larger quadrupole coupling constant has moved further away from the centre of the tetrahedron and on the other hand, the boron nucleus at the site possessing a smaller quadrupole coupling constant has moved closer to the centre of the tetrahedron than their corresponding sites at room temperature. If this hypothesis is true then it implies that the boron-oxygen units form electric dipoles in the phase with the point group 2, and that the resultant of these individual dipoles must be parallel to the monoclinic axis.

Although we feel that our results indicate that the boron atoms have undergone displacements with respect to the oxygen atoms, one cannot rule out the possibility that the effects at the boron sites are simply due to the new orientations of the hydrogen atoms. However, the contributions of H atoms to the $\tilde{\nabla}E$'s at boron sites are likely to be small because the oxygen nearest-neighbours provide a shield to the influence of the next-nearest-neighbours and because hydrogen atoms are both small and far removed from these sites. Although hydrogen atoms may not contribute appreciably to the resultant dipole moment per unit cell, they still may play a very important rôle in the ferroelectricity

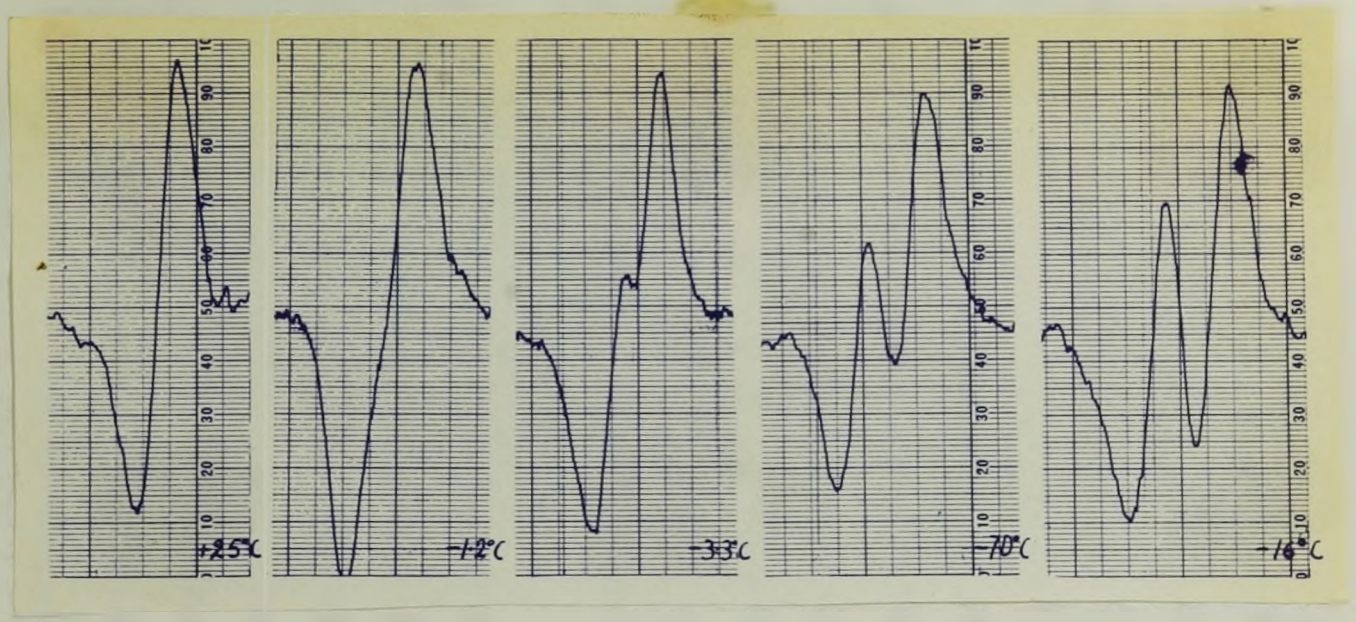

Fig. 20. The Temperature Effect upon the Satellite Lines Belonging to the B^{11} Sites K in Colemanite at Selected Temperatures (for $\theta_y = 35^{\circ}$).

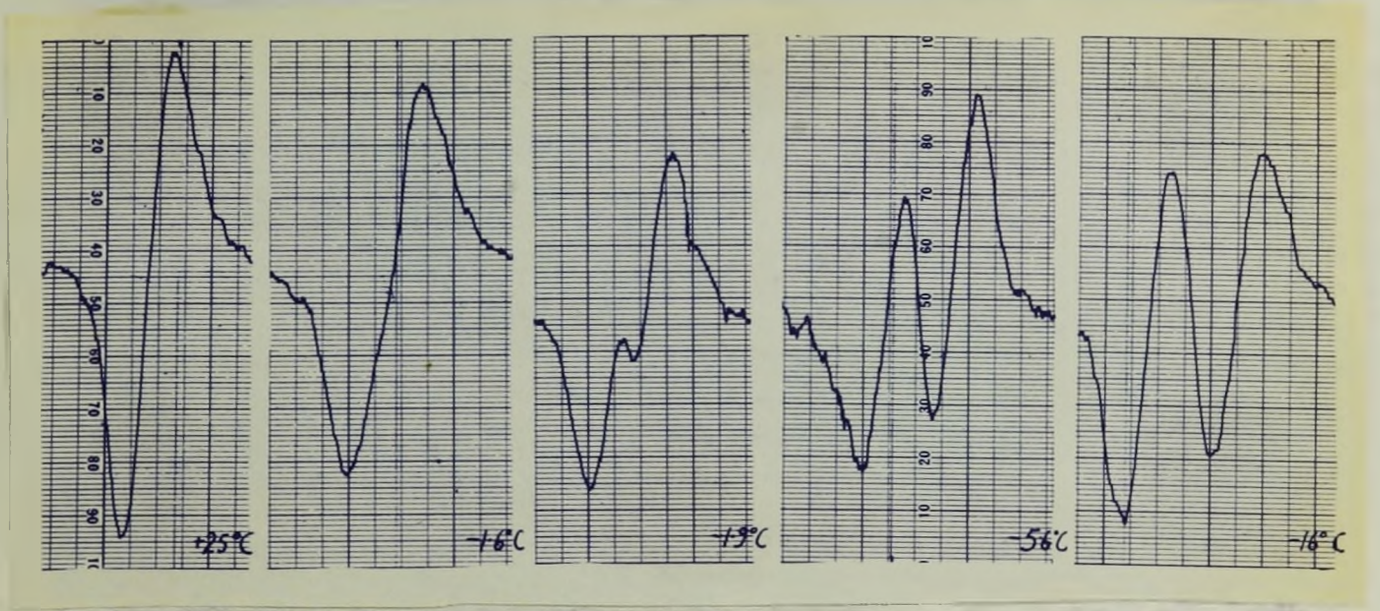

Fig. 21. The Temperature Effect upon the Satellite Lines Belonging to the B^{11} Sites L in Colemanite at Selected Temperatures (for $\Theta_y = 149^{\circ}$)

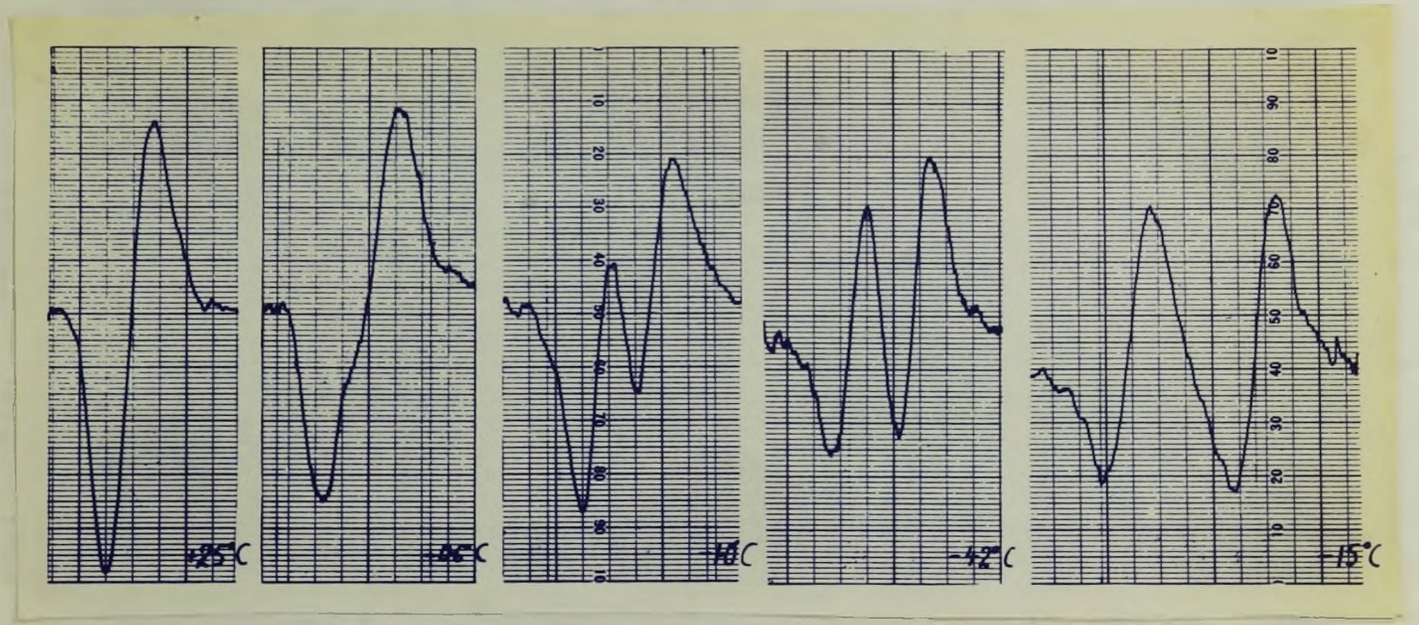

Fig. 22. The Temperature Effect upon the Satellite Lines Belonging to the B^{11} Sites M in Colemanite at Selected Temperatures (for $\theta_y = 149^o$).

in colemanite. They may trigger the ferroelectric transition in a way similar to their action in the KH_2PO_4 type of ferroelectrics.

V. 4. We shall now discuss the phase transitions in colemanite. The results of the investigation of the selected set of B^{11} n.m.r. lines over a temperature range were described in Chapter IV and summarised in Fig.15. The effects are illustrated in Figs. 20, 21 and 22, which show the changes which occurred in representative resonance lines belonging to the K, L and M sites, respectively, at selected temperatures over the range room temperature to -16° C. As the temperature is lowered, the narrow signals are first broadened which implies a very small splitting, then they are split by a measurable amount and, finally, they separate into two components. It should be noted in particular that the changes in the n.m.r. spectrum occurring at the transition are not due to a gradual growth of the signals belonging to the ferroelectric phase at the expense of the signal belonging to the centrosymmetric phase. This implies that, provided the temperature of the single crystal is uniform, the two phases, the ferroelectric and the centrosymmetric, never coexist together. In other words, the transition cannot be of the order-disorder or martensitic type. The fact that the separation of the signals is at first infinitesimal indicates that, as far as the positions of the atoms are concerned, the two phases differ only by infinitesimal amount when they are at exactly the transition temperature. Also, the fact that the separation of the signals is not rapid but is brought about gradually over a finite temperature range

indicates that the transition is of the thermodynamic second-order type.

Incidentally, it was mentioned in Section IV.4 that the intensities of the lines belonging to sites M_3^* and M_4^* were consistently smaller and broader than those belonging to the sites M_1^* and M_2^*. Since this effect was observed only at temperatures lower than -20° C., its possible explanation may involve the second transition which was discussed in this work, but it is not certain in what way.

The point group of colemanite in the newly discovered phase cannot be other than the triclinic point group 1. Now, while this point group admits ferroelectricity, no known crystal possessing this point group has ever been observed to be ferroelectric. Taking into consideration the fact that colemanite has been observed to be ferroelectric right down to -195° C. by both Chynoweth ('57) and Goldsmith ('56), hence it must be ferroelectric in this newly discovered phase since the transition temperature occurs between -38° C. and -80° C. Thus, it appears that colemanite is the only known example of a ferroelectric crystal with point group 1. This phase is also interesting because the ferroelectric axis is not confined by symmetry to any particular crystal direction.

Since it does not seem to have been pointed out in the literature, it may be worth mentioning that colemanite is likely to be anti-ferroelectric at room temperature. Glide planes and two-fold screw axes, the symmetry elements of colemanite at room temperature, permit the existence of individual dipole moments within the unit cell although, of course, their resultant per unit cell must vanish for the point group

2/m. Also, calculations based on the atomic coordinates show that all the borons are off-centre in their respective O_3 triangles and O_4 tetrahedra but the displacements involved are so small that they may not be significant. In addition, the variations of the $\Delta\nu$ values plotted in Fig.16 for the temperature range 52° C. to Curie point and the room temperature results support this idea that the boron atoms are displaced from the centre of gravity of their oxygen nearest-neighbours.

An enumeration of the results described in this thesis may now be appropriate:

1) The point group of colemanite at room temperature has been found to be 2/m.

2) The point group of colemanite at -40° C. has been found to be 2.

3) The electric field gradient tensors at all B^{11} sites in colemanite at room temperature and at -40° C. have been completely determined.

4) The results have been partially interpreted in terms of the crystal structure.

5) The ferroelectric transition has been studied thoroughly with the following results:

(i) The Curie point depends upon the history of the crystal. It probably lies close to 0° C. in a colemanite crystal free of strains.

(ii) The transition is not of the order-disorder, or martensitic, type.

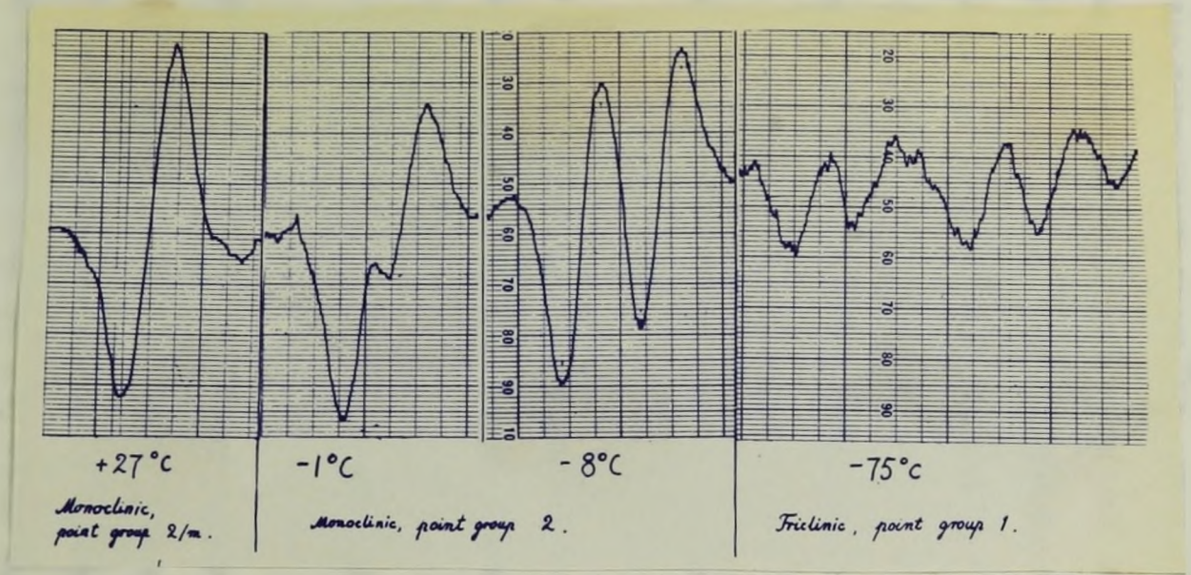

Fig. 23. Typical Satellite Lines Belonging to the B^{11} Sites M in Colemanite in the Three Phases (for $\theta_y = 149^o$).

(iii) The transition is second-order.

6) A new phase in colemanite has been discovered. The transition into this phase is characterised by a large thermal hysteresis loop extending between the temperatures of about -35° C. to about -80° C.

Thus, following are the known phases in colemanite stable in the decreasing temperature scale:

monoclinic	monoclinic	triclinic
point group 2/m	point group 2	point group 1

Fig.23 portrays typical satellite signals belonging to B^{11} M sites at $\theta_y = 149^\circ$ in these three phases.

REFERENCES

Bersohn, R. J. Chem. Phys. 20: 1505, 1952.

Bloch, F., Hansen, W. N. and Packard, M. Phys. Rev. 69: 37, 1946.

Christ, C. L. Am. Min. 30: 411, 1953.

Christ, C. L., Clark, J. R. and Evans, H. T. Acta Cryst. 1: 453, 1954.

Chynoweth, A. G. Acta Cryst. 10: 511, 1957.

Cotts, R. M. and Knight, W. D. Phys. Rev. 96: 1285, 1954.

Das, T. P. and Bersohn, R. Phys. Rev. 102: 733, 1956.

Datars, R. D. M. Sc. Thesis, McMaster University, Hamilton, Ont., 1956.

Davisson, J. W. Acta Cryst. 9: 9, 1956.

Goldsmith, G. J. Bull. Am. Phys. Soc., Ser. II 1: 322, 1956.

Megaw, H. D. Ferroelectricity in Crystals, Methuen & Co., London. 1957.

Morimoto, N. Min. (Japan) 2: 1, 1956.

Petch, H. E., Cranna, N. G. and Volkoff, G. M. Can J. Phys. 31: 837, 1953.

Petch, H. E. and Holuj, F. Abstracts of the Communications at the Fourth Annual Congress of International Union of Crystallographers, 51. 13, 1957.

Portoles, L. Estud. Geol. Inst. Malada 5: 3, 1947; 7: 21, 1948.

Pound, R. V. Phys. Rev. 79: 685, 1950.

Purcell, E. M., Torrey, H. C. and Pound, R. V. Phys. Rev. 70: 474, 1946.

Sternheimer, R. M. and Foley, H. M. Phys. Rev. 102: 731, 1956.

Volkoff, G. M., Petch, H. E. and Smellie, D. W. L. Phys. Rev. 84: 602, 1951.

Can. J. Phys. 30: 270, 1952.

Volkoff, G. M. Can. J. Phys. 31: 820, 1953.

Waterman, H. H. and Volkoff, G. M. Can. J. Phys. 33: 156, 1955.

Waterman, H. H. Ph. D. Thesis, University of British Columbia, Vancouver, B. C., 1954.

Whittaker, E. and Robinson, G. The Calculus of Observations, Blakie & Son Ltd., London. 1948.